UNIVERSITY OF CALIFORNIA, SAN DIEGO

# Coordination of Axonal Transport Revealed by Particle Tracking and Quantitative Immunofluorescence

A dissertation submitted in partial satisfaction

of the requirements for the degree

Doctor of Philosophy

in

Bioinformatics and Systems Biology

by

Lukasz J Szpankowski

Committee in charge:

Professor Lawrence Goldstein, Chair
Professor Shankar Subramaniam, Co-Chair
Professor Philip E. Bourne
Professor Arshad B. Desai
Professor Terence T. Hwa

2011

The Dissertation of Lukasz J Szpankowski is approved, and it is acceptable in quality and form for publication on microfilm and electronically:

---

---

---

---

Co-Chair

---

Chair

University of California, San Diego

2011

## DEDICATION

*Mojemu Ojcu, który nigdy nie zniżył swojego*

*lotu i oczekuje tego samego ode mnie…*

## EPIGRAPH

*"One can prefer to be an optimist or a pessimist,*

*but the best approach is to be an empiricist"*

- Eric S. Lander

**TABLE OF CONTENTS**

## LIST OF ABBREVIATIONS

**APP** – amyloid precursor protein

**APPYFP** – amyloid precursor protein fused to yellow fluorescent protein

**KLC** – kinesin light chain

**KHC** – kinesin heavy chain

**DHC** – dynein heavy chain

**DIC** – dynein intermediate chain

**IF** – immunofluorescence

**PSF** – point spread function

**SNR** – signal to noise ratio

**$PrP^C$** – cellular mammalian prion protein

**MT -** microtubule

**RL** – run length

**SV** – segmental velocity

**PF**– pause frequency

**PD** – pause duration

## LIST OF FIGURES

## LIST OF TABLES

## ACKNOWLEDGMENTS

First and foremost, I would like to thank my advisor, Dr. Larry Goldstein, for the exemplary support and encouragement throughout my graduate studies. From our very first meeting, he has treated me as an equal and always valued my opinion. Not only is Larry a tremendous scientific mind, but he is one of the most fair and honest individuals I have ever met. He has drastically influenced the way I think, solve problems, and present solutions; characteristics for which I am forever grateful. In similar fashion, I would like to thank my co-advisor, Dr. Shankar Subramaniam, a brilliant man whose influence has greatly impacted my life. The guidance of my other committee members, Drs. Terry Hwa, Philip Bourne, and Arshad Desai, has been invaluable. I am indebted to my committee for all of their expertise, advice, and encouragement at many points along the way.

I am extremely grateful for the help of my friends and colleagues in the Goldstein Lab, all of which had a significant influence on my research and time in graduate school. In particular, I would like to acknowledge Drs. Gerald Reis and Sandra Encalada, for all the conversations, support, mentoring, and collaboration over the years. You both have had a great impact on my life as a scientist. To the other graduate students in the lab, Mason Israel – my bay mate and friend, Emily Davis – GO BLUE, Jessica Rusert, Liz Rodriguez and Rhiannon Killian, I wish you all the best. Sol and Grace, you two are about to take over. None of my work would have been possible without the amazing group of brilliant post-docs, project scientists, lab techs, and administrators I have had the honor to work with in the lab.

Many individuals have had a direct influence on making my project possible. Drs. Ge Yang, Khuloud Jaqaman, and Gaudenz Danuser have been absolutely critical in helping me develop the computational aspect of my work. Jennifer Meerloo and the Neuroscience Microscopy Core for state-of-the-art microscopy and imaging tools, from which I was able to form the basis of my work. I would also like to thank the entire Interdisciplinary Bioinformatics and Systems Biology Program and especially Laura Gracia, our wonderful graduate coordinator.

Most importantly, I would like to thank my family, for all the love and support over the years. Clearly, none of this would have been possible without you all. To my amazing grandfather, who did not live to see this document, you will always be a part of me and what I achieve. To my grandmother, for her supporting presence and unfading interest in all aspects of my life. My mother, for helping me see things in perspective and stay true to myself. To my father, the brilliant professor and '$6^{th}$ member' of my committee, who this dissertation is dedicated to, has taught me to always aim high, stay confident, and challenge myself. You always think 5 steps ahead, and I hope to apply the knowledge I have gained from you to all my future pursuits. My sister Paulina, one of the kindest people I know, who has been there for me through thick and thin, you have such a bright future ahead.

Lastly, I would like to thank my wonderful friends, old and new. In particular, my roommate Jim Marshel, for all our conversations, optimizations, and general debates about everything science as well as everything not. Scott Wilke, Katie Travis, we started this whole process over five years ago and made it through together. I owe you all a great deal for the support. To my dear high school and college friends, you know who you are,

thank you for the wonderful times and in advance for all the future adventures. You have truly helped keep my head in reality. And as my final note, I would like to acknowledge my friends at the ARCS San Diego Chapter, for financial support, encouragement, and networking opportunities.

Chapter 2, in part, is a reprint of the following manuscript currently in review. Reis, G.F.,* G. Yang*, L. Szpankowski, C. Weaver, S.B. Shah, J.T. Robinson, T.S. Hays, G. Danuser, L.S.B. Goldstein. "Kinesin-1 Driven Axonal Transport of APP Vesicles in Vivo is Weakly Processive and Promoted by Interactions with the Intermediate Chain of Cytoplasmic Dynein." The dissertation author was the secondary investigator and author of this paper.

Chapter 3, in part, is currently being prepared for submission. Szpankowski, L., S.E. Encalada, L.S.B. Goldstein. "Elucidating the Relative Motor Subunit Composition of APP Vesicles." The dissertation author was the primary investigator and author of this paper.

Chapter 4, in part, is a reprint of the following published manuscript. Encalada, S.E., L. Szpankowski, C. Xia, L.S.B. Goldstein. (2011). "Stable Kinesin and Dynein Assemblies Drive the Axonal Transport of Mammalian Prion Protein Vesicles." *Cell* 144(4): 551-565. The dissertation author was the secondary investigator and author of this paper and co-led the development, implementation, and analysis of the quantitative immunofluorescence method.

## VITA AND PUBLICATIONS

| | |
|---|---|
| 2005 | Bachelor of Science in Cell and Molecular Biology, University of Michigan, Ann Arbor |
| 2011 | Doctor of Philosophy in Bioinformatics and Systems Biology, University of California, San Diego |

Szpankowski, L., S.E. Encalada, L.S.B. Goldstein. "Elucidating the Relative Motor Subunit Composition of APP Vesicles." (*in preparation*)

C. Weaver, L. Szpankowski, C. Leidel, G. Shubeita, L.S.B. Goldstein. "Endogneous GSK-3/Shaggy Regulates Bidirectional Transport of the Amyloid Precursor Protein." (*in revision*)

Reis, G.F.,* G. Yang*, L. Szpankowski, C. Weaver, S.B. Shah, J.T. Robinson, T.S. Hays, G. Danuser, L.S.B. Goldstein. "Kinesin-1 Driven Axonal Transport of APP Vesicles in Vivo is Weakly Processive and Promoted by Interactions with the Intermediate Chain of Cytoplasmic Dynein." (*in revision*)

Encalada, S.E., L. Szpankowski, C. Xia, L.S.B. Goldstein. (2011). "Stable Kinesin and Dynein Assemblies Drive the Axonal Transport of Mammalian Prion Protein Vesicles." *Cell* 144(4): 551-565.

Aktulga, H.M., I. Kontoyiannis, L. Lyznik, L. Szpankowski, A. Grama, W. Szpankowski. (2007). " Identifying Statistical Dependence in Genomic Sequences via Mutual Estimates." *EURASIP Journal on Bioinformatics & Systems Biology*: 14741.

Szpankowski, W., W. Ren, L. Szpankowski. (2005). "An Optimal DNA Segmentation Based on the MDL Principle." *Int. J. Bioinformatics Research and Applications* 1(1): 3-17.

## ABSTRACT OF THE DISSERTATION

Coordination of Axonal Transport Revealed by Particle Tracking and Quantitative Immunofluorescence

by

Lukasz J Szpankowski

Doctor of Philosophy in Bioinformatics and Systems Biology

University of California, San Diego, 2011

Professor Lawrence Goldstein, Chair

Professor Shankar Subramaniam, Co-Chair

Movement is intrinsic to life. Most forms of directed nanoscopic, microscopic and ultimately, macroscopic movement in cells is powered by tiny protein machines known as molecular motors. Microtubule-based motor proteins from the kinesin and dynein superfamilies are essential for many of these transport processes and coordinate to

distribute various cellular cargos, including vesicles, organelles, protein complexes, and mRNAs to appropriate destinations within the cell. Due to the extreme compartmentalization of neurons, long range transport is particularly critical and recent advances suggests that these transport systems may fail early in the pathogenesis of a number of neurodegenerative diseases. Although substantial progress has been made to understand the underlying fundamentals, how these two opposite polarity motor protein families cooperate to generate coordinated bidirectional movement is poorly understood. This work reveals a number of novel features of coordinated axonal transport through robust particle tracking and quantitative immunofluorescence for two medically relevant classes of cargos; amyloid precursor protein (APP) and cellular prion protein ($PrP^C$) vesicles.

We developed a quantitative approach to analyze the axonal transport of YFP-tagged APP vesicles in *Drosophila* segmental nerves using heterozygous animals. This allowed us to assess the contribution of individual motor subunits and accessory proteins to coordinated axonal transport. Our approach yielded a novel model for how motor proteins work together to achieve bi-directional transport. We subsequently propose a robust image analysis method to assess relative motor subunit composition of individual endogenous APP vesicles in mouse hippocampal culture. Our data provides new insight on how select motor subunit and cargo attachment protein levels contribute to the overall architecture of these vesicles. Finally, we characterize the intracellular transport and steady-state motor subunit composition of mammalian $PrP^C$ vesicles. We suggest a coordination model wherein $PrP^C$ vesicles maintain a stable population of associated

motors whose activity is modulated by regulatory factors instead of by structural changes to motor-cargo associations.

Since disruption of this transport machinery has been implicated in numerous neurodegenerative diseases, such as Alzheimer's, Parkinson's, and ALS, elucidating the underlying fundamentals of this highly coordinated system is an essential part of understanding what happens during the progression of these devastating illnesses.

# 1 INTRODUCTION

We are interested in how the cellular machinery works to coordinate movement of materials inside of nerve cells. Similar to how trucks deliver goods using a network of highways, cells use molecular motors to coordinate bidirectional transport of essential cargo using molecular tracks. Proper functioning of intracellular transport is crucial for many aspects of cell sustainability and overall organism health. Eukaryotic cells require long distance transport on microtubule tracks, along which superfamilies of kinesins and dyneins generate ATP-dependent movements. This is especially the case for neurons, where in large mammals, such as humans, nerve cells can stretch over one meter in length. A hallmark of the polarized structure of a nerve cell is its long thin axon, a cytoplasmic process than can extend over a meter in length from the neuronal cell body before ending at a synapse. Proteins and other vital molecular signals are synthesized in the cell body and need to be actively distributed to locations throughout the axonal process. It would take approximately 150 years for a 3-nm-radius protein (~100 kDa) to diffuse 1 meter in water (Howard 2001) or over 2000 years in cytoplasm; hence, diffusion is inadequate for long distance movement. Clearly, active transport is an essential process, even for small metabolites and proteins.

In general, microtubule-based bidirectional transport is coordinated in the cell by families of kinesin (anterograde) and dynein (retrograde) motor complexes which are essential for neuronal function and survival as well as the overall transport of vesicles and organelles to appropriate destinations. In addition, recent work has demonstrated that kinesin and dynein motor proteins play critical roles in long-distance signaling events in neurons, neuronal regeneration, and in the development of neurodegenerative disease (Goldstein 2003). Mutations in genes that code for various subunits of the molecular machinery have been strongly implicated in several human neurodegenerative diseases including Alzheimer's, Parkinson's, and amyotrophic lateral sclerosis (ALS) (De Vos, Grierson et al. 2008). Elucidating the underlying fundamentals of this highly coordinated system is an essential part of understanding what happens during the progression of these devastating illnesses.

Microtubules are dynamic polymers composed of α- and β-tubulin dimers and serve as one of the fundamental components of the cytoskeleton. They have a diameter of roughly 25nm and serve not only as structural components within cells but are also directly involved in many vital cellular processes including mitosis, cytokinesis, and vesicular transport (Baas 1999). In addition, they exhibit an intrinsic polarity. In the case of axons, microtubules are organized with their (+)-ends towards the synapse and their (-)-ends pointing towards the neuronal cell body. Intracellular trafficking towards the synapse, anterograde transport, is driven by microtubule plus-end kinesins, while minus-end directed dyneins are responsible for the corresponding retrograde movements (Goldstein and Yang 2000).

Kinesin-1 is composed of heavy chain (KHC or KIF5) and light chain (KLC) subunits. The kinesin-1 motor activity is located in the KHC subunit (Goldstein and Philp 1999) while cargo binding and regulatory activities are located in both KHC and KLC. The N-terminus of KLC interacts with KHC while the TPR repeat regions of KLC play a role in cargo attachment (Kamal, Stokin et al. 2000). Many studies suggest roles for kinesin-1 in cellular movements including lysosome distribution, mitochondrial movement, intermediate filament organization, transport to the apical and basolateral surfaces in polarized cells, and axonal transport of numerous types of vesicles as well as neurofilaments and tubulin (Gindhart, Desai et al. 1998).

The minus-end directed retrograde motor dynein is a large protein complex with six subunits: a large dynein heavy chain (DHC), an intermediate and light-intermediate chain (DIC and DLIC), and 3 dynein light chains (DLC). Dynein has many cellular functions including axonal transport, Golgi organization, mitochondrial movement, and others. Each dynein subunit may be capable of multiple protein-protein interactions that mediate regulation and binding to cellular cargos (Pfister, Shah et al. 2006). Dynein functions also require a protein complex called dynactin, which is composed of 11 subunits. Two key dynactin subunits are arp1, which forms the filamentous base of the dynactin complex, and p150Glued, which forms a long arm extending from the filamentous base of the dynactin complex (Schroer 2004). The p150Glued protein has been shown to bind to many other proteins including DIC and microtubules. Fig 1-1 shows a to-scale portrayal of motor subunit architecture on a vesicle of average size.

One of the most intriguing problems in the field of axonal transport is how these opposite polarity motors regulate their activity to achieve bi-directional movement of

vesicles and organelles within axons. Until recently, our understanding of how kinesin, dynein, and dynactin are organized on the surface of vesicles and function together to yield bi-directional transport was limited to the following. For anterograde movement, kinesin has been thought to be the sole mediator of anterograde movement within axons (Goldstein and Philp 1999) and behave as a highly processive motor whose function does not require a co-factor (Block 1995). Furthermore, cytoplasmic dynein is considered the sole motor responsible for retrograde axonal transport (King and Schroer 2000) and behave in a poorly processive fashion requiring dynactin to function optimally (Levy and Holzbaur 2006). The dynactin protein complex is thought to function as the primary enhancer for dynein's processivity as well as a vesicular attachment factor for cytoplasmic dynein via interactions between arp 1 (the filamentous base of dynactin) and the spectrin cytoskeleton (Schroer 2004). Together, these reports have led to the "standard model" for axonal transport found in current textbooks and encyclopedias. This model however, has several shortcomings, which were revealed by recent studies. Namely, it does not explain switching between opposite motor activities, a behavior of which has been observed for many vesicles. Furthermore, it does not take into account recently reported biochemical interactions between DIC and KLC (Ligon, Tokito et al. 2004). And thirdly, it does not explain why dynactin mutations seem to affect both kinesin-1 and dynein function (Gross, Welte et al. 2002).

The first step in the process of teasing out the transport mechanisms at play was to choose a specific class of axonally transported vesicles to investigate. Bidirectional transport of different types of cargos may be controlled by distinct types of motor coordination. We directed our focus on the transport of APP vesicles in axons, primarily

because these vesicles are of major scientific and medical interest. Medically, these vesicles and their behavior, as well as the transport and proteolytic processing of the APP protein appear to be key players in the development of Alzheimer's disease (Stokin and Goldstein 2006). Scientifically, APP vesicles undergo long distance kinesin-1 dependent anterograde transport in axons, the APP protein is readily tagged and visualized, transport exhibits both anterograde and retrograde components (Gunawardena, Her et al. 2003), and coordination of kinesin-1 and dynein, perhaps via dynactin, is apparent. Furthermore, axons are a system with significant technical advantages because of the extreme spatial separation of a cellular compartment enriched in active transport. As a model system, APP vesicles have some additionally important advantages including a large body of information about biochemical behavior, purification methods, and phenotypes in different contexts (Stokin and Goldstein 2006). Recent work has uncovered that APP forms a complex with the TPR domain of KLC through coimmuno-precipitation, sucrose gradient, and direct in vitro binding assays (Kamal, Stokin et al. 2000). In this view, one of the normal functions of APP may be as a membrane cargo receptor for kinesin-1.

Previous work led to formulation of three general models to account for coordination of bidirectional vesicle movement (Gross 2004). These models were developed and evaluated primarily on the basis of observations of short-range movements of lipid droplets, melanosomes, and other non-neuronal or non-natural cargo movement paradigms such as movement in S2 cell filopodia. In generating predictions from these models for APP axonal vesicle movement, all of these models rely upon previous evidence that kinesin-1 generates anterograde axonal APP vesicle movements, dynein

generates retrograde APP movements, and dynactin is required for dynein attachment to vesicles and/or the enhancement of dynein processivity. With these initial assumptions, each of these models makes distinct predictions about the expected pattern of behavior when kinesin-1, dynein, or dynactin are reduced in amount or eliminated. For example, in the *tug-of-war* model, simultaneous attachment and activity of opposing motor activities is proposed to generate net movement in one direction or another depending upon the relative number of each type of motor attached to a vesicle at a given time. This simple model predicts that reduction of kinesin-1 should increase retrograde transport while reduction of dynein should enhance anterograde transport. Similarly, increased kinesin-1 is predicted either to have no effect or to stimulate anterograde activity and reduce retrograde activity. In the *exclusionary-presence* model, vesicles can bind to kinesin or dynein, but not to both simultaneously. This model has similar predictions to the tug-of-war model. Finally, in the *coordination* model (Kural, Kim et al. 2005), vesicles bind to both kinesin and dynein simultaneously, but an unknown coordination process on the vesicle surface ensures that both types of motor are not active at the same time. The predictions of this model are less obvious given the lack of a defined proposed coordination mechanism, but at minimum if dynein and kinesin-1 themselves are part of the coordination mechanism then reductions of dynein or kinesin-1 might impair movements in the opposite direction. All models predict that shifts in the amount of either one of the motors would cause a reduction of reversal frequency and/or a decrease in the pause duration and in the number of the stationary vesicles. For vesicle transport in non-neuronal cases, it was argued that a coordination model of some sort best accounts for the experimental observations (Gross 2004).

To probe these issues, we developed a semi-automated vesicle tracking and analysis software package. This approach enabled detailed high-resolution computational analysis of a large number of bi-directionally moving, fluorescent amyloid precursor protein (APP-YFP) vesicles in living *Drosophila* segmental nerve axons and is outlined in Chapter 2. Imaging in wild type and mutant backgrounds expressing a 50% genetic reduction in components of kinesin and dynein motor complexes, provided a comparative analysis of numerous transport parameters across 16 selected motor-subunit-deficient genotypes resulting in over 40,000 tracked particles. This vast dataset reveals a number of previously unknown features of axonal vesicle movement and strongly questions most current conventional models of motor coordination and attachment on axonal vesicles. These findings have led us to propose a new model for how bidirectionally coordinated vesicle movement in axons is generated by antagonistic motor proteins in which competition of dynactin and kinesin for binding to DIC controls the direction of movement.

Although this is certainly substantial progress, several key pieces of information required to further tease apart the mechanism at play are missing. We have obtained an immense amount of information on the overall axonal transport of APP vesicles, but what happens on *individual* vesicles remains largely a mystery. Taking a look at motor subunit architecture on individual APP vesicles in control and motor mutant genotypes will surely shed light on these fundamental intracellular processes. Chapter 3 outlines an investigation of relative motor protein concentrations on individual APP vesicles using an optical approach followed by extraction of key information using custom image analysis software. This novel quantitative immunofluorescence approach can be applied to the

study of a variety of colocalization events in many systems. A novel and puzzling result from the *Drosophila* analysis indicates that retrograde transport is impaired when the anterograde kinesin motor subunits are genetically reduced. Current hypotheses posit that since kinesin is known to be an activator of dynein, reductions in kinesin impair retrograde transport by decreasing activation of dynein subunits on individual APP vesicles. We report that this does not seem to be the case, and reduction of kinesin light chain-1 on the vesicle in fact leads to reduced dynein heavy chain association. Additionally, we observe an increase of both kinesin and dynein subunit association as a function of the amount of APP carried in a particular vesicle.

Notably, how the motor protein cocktail changes on vesicles of known transport class (anterograde, retrograde, stationary, and reversing) has yet to be determined. There have been efforts to answer these questions, and the motivation for elucidating these mechanisms has certainly been prominent in the field, but no system to date has had the potential to really unfold these mysteries. Chapter 4 presents a method to directly investigate these questions using a technique we developed which exploits innovative microfluidic chambers, a combination of imaging methods, and custom image analysis software to uncover motor subunit architectures on vesicles of known transport class. This final chapter focuses on another type of medically relevant axonally transported cargo, the prion protein ($PrP^C$) vesicle. We present a comprehensive analysis, where the intracellular transport and steady-state motor subunit composition of $PrP^C$ is characterized leading to a proposed coordination model where $PrP^C$ vesicles maintain a stable population of associated motors whose activity is modulated by regulatory factors instead of by structural changes to motor-cargo associations.

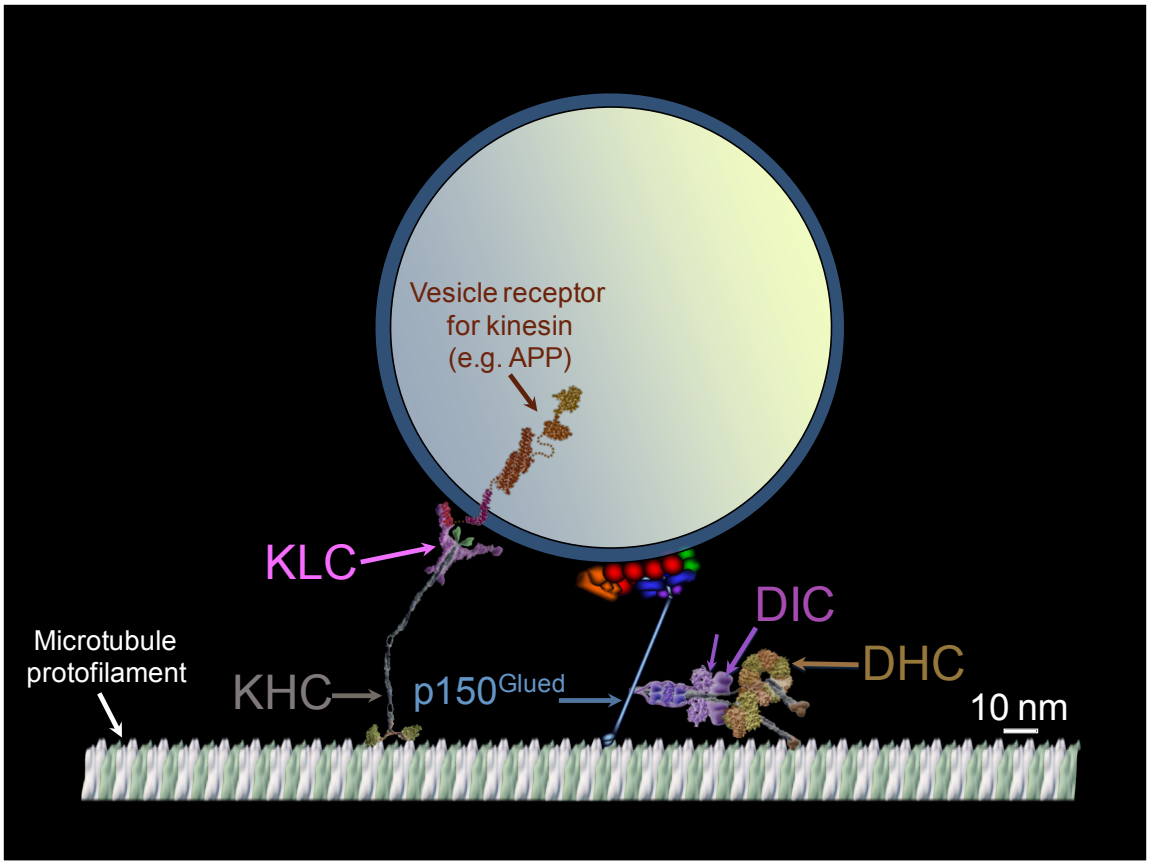


**Figure 1-1** Schematic diagram of motor-cargo association. This to-scale depiction shows both kinesin and dynein attached to a vesicle of average size and the microtubule protofilament.

# 2 KINESIN-1 DRIVEN AXONAL TRANSPORT OF APP VESICLES IN VIVO IS WEAKLY PROCESSIVE AND PROMOTED BY INTERACTIONS WITH THE INTERMEDIATE CHAIN OF CYTOPLASIMIC DYNEIN

**Abstract**

Bidirectional axonal transport driven by kinesin and dynein along microtubules is critical to neuronal viability and function. To evaluate axonal transport mechanisms, we developed a high-resolution imaging system to track the movement of amyloid precursor protein (APP) vesicles in *Drosophila* nerve axons. Computational analyses of a large number of moving vesicles in defined genetic backgrounds enabled us to test with precision existing and new models of motor activity and coordination in vivo. We discovered several previously unknown features of vesicle movement, including the finding that anterograde APP movement powered by kinesin-1 in vivo displays the characteristics of non-processive motors. This finding is largely incompatible with the properties of kinesin-1 derived from in vitro biophysical analyses. Our data also suggest that kinesin-1 and cytoplasmic dynein motors assemble in stable mixtures on APP vesicles and that their direction and velocity are controlled at least in part by dynein intermediate chain.

## 2.1 Introduction

A hallmark of the polarized structure of a neuron is its long thin axon, a cytoplasmic process that can extend for more than one meter in humans. Within the axon, a wide variety of cargos essential for the viability and function of the neuron must be transported along microtubules between the neuronal cell body and synapses (Grafstein and Forman 1980). Understanding how molecular motor proteins drive this axonal transport is essential to understanding a wide range of neurological diseases associated with transport defects (Chevalier-Larsen and Holzbaur 2006; Duncan and Goldstein 2006; Stokin and Goldstein 2006; De Vos, Grierson et al. 2008).

Axonal transport is driven by motor proteins that can move along polarized microtubules in different directions (Goldstein and Yang 2000; Hirokawa and Takemura 2005). Transport toward synapses (anterograde transport) is driven by microtubule plus-end directed kinesins, especially those from the kinesin 1-4 and 13 families (Goldstein and Yang 2000; Lawrence, Dawe et al. 2004; Hirokawa and Takemura 2005). Kinesin-1 of higher eukaryotes consists of two types of subunits: kinesin heavy chain (KHC) and kinesin light chain (KLC). Transport toward the neuronal cell body (retrograde transport) is driven by microtubule minus-end directed cytoplasmic dynein (King 2000; Vallee, Williams et al. 2004) whose in vivo functions require dynactin (Schroer 2004). Cytoplasmic dynein consists of four subunits: dynein heavy chain (DHC), dynein intermediate chain (DIC), dynein light intermediate chain (DLIC), and dynein light chain (DLC), whereas the dynein cofactor dynactin consists of ten different subunits (Schroer 2004).

A substantial amount of information about the biophysics, biochemical

mechanisms of movement, and mechanics of kinesin-1 and cytoplasmic dynein motors has emerged from extensive in vitro studies. For example, single kinesin-1 motors can walk processively towards microtubule plus ends for hundreds of steps, resulting in typical in vitro run-lengths of approximately one micrometer (Howard, Hudspeth et al. 1989; Block, Goldstein et al. 1990; Svoboda, Schmidt et al. 1993). In keeping with the high degree of processivity, the velocity of microtubule or bead movement driven by kinesin-1 in vitro does not vary with the number of available motors (Howard, Hudspeth et al. 1989; Block, Goldstein et al. 1990; Svoboda, Schmidt et al. 1993). Similarly, in vitro bead movement generated by cytoplasmic dynein is also processive (Wang, Khan et al. 1995; Reck-Peterson, Yildiz et al. 2006; Gennerich, Carter et al. 2007) though to a lesser extent than kinesin-1. Additionally, cytoplasmic dynein uses dynactin to enhance processivity (Schroer 2004).

It remains largely unknown how the in vitro behavior of kinesin-1 and cytoplasmic dynein motors relates to long-range axonal transport of vesicles and organelles in vivo. Similarly, it is uncertain to what extent in vitro motor behavior predicts that of in vivo. Indeed, the reported characteristics of movement driven by kinesin-1 and cytoplasmic dynein in vitro are at odds with a number of in vivo observations of vesicle and organelle motion in axons. First, single cargos often move substantially faster in vivo than can be generated by single or multiple kinesin-1 and cytoplasmic dynein motors in vitro (e.g., (Kural, Kim et al. 2005). Second, distances traveled by axonal vesicles in vivo can be two to three orders of magnitude longer than the average run-lengths generated by kinesin-1 and cytoplasmic dynein motors in vitro (Grafstein and Forman 1980). In addition, some axonal cargos switch frequently between

anterograde and retrograde movement (Gross 2004). Thus, comprehensive in vivo quantitative analysis of cargo motion driven by kinesin-1 and cytoplasmic dynein is essential to understand the mechanisms of motor function in axonal transport. Furthermore, in vivo studies are crucial for determining how in vitro properties are harnessed to generate in vivo behavior. Such analyses, however, have been lacking because of the challenges in precisely manipulating motor function and accurately measuring consequent changes in cargo motion in vivo.

Genetic analysis in cells and organisms provides a unique and powerful tool to probe the function of motor proteins and regulators in vesicle and organelle transport in vivo. Previous studies generally used models lacking most to all motor function or relied on high-level overexpression of kinesin-1, cytoplasmic dynein, or dynactin subunits (Martin, Iyadurai et al. 1999; Chevalier-Larsen and Holzbaur 2006). These manipulations often caused pleiotropic phenotypes, which provided limited information as to how the kinetics of vesicle or organelle movements in vivo depend on specific motor properties. Hence, development and testing of molecularly explicit models of vesicle movement have been difficult. To circumvent these problems, we used modest reduction or overexpression of functional kinesin-1, cytoplasmic dynein, or dynactin subunits. To achieve sufficient sensitivity for robust interpretation of the associated weak phenotypes in the absence of organismal inviability, we developed computer-assisted quantification of the precise behavior of large numbers of amyloid precursor protein (APP) axonal vesicles. Based on statistical analyses of the distribution of motion parameters, we could test different models of mechanical and regulated motor interaction on vesicles in vivo. Most surprisingly, our data provides strong evidence that kinesin-1

behaves as a poorly processive motor in vivo. Our data also support a new model for in vivo motor coordination and reveal that stable motor loading is a feature of APP vesicle transport.

## 2.2 Results

### 2.2.1 Establishing the properties of axonal APP vesicle movement in vivo

To probe the trafficking behavior of individual APP vesicles in *Drosophila* larval segmental nerves in vivo, we used SG26.1 Gal4 to drive the expression of UAS-APPYFP. Because the expression of SG26.1 Gal4 is confined to a subset of ventral ganglion neurons, APPYFP fluorescent vesicles are generally found and visualized in only a single axon within a segmental nerve. To confirm that microtubules in these axons are oriented with their plus ends directed away from cell bodies, we expressed the plus-end binding protein, EB1-GFP, using the same driver. Of 165 EB1-GFP particles tracked, 160 (97%) moved away from the cell body, consistent with a previous report (Stone, Roegiers et al. 2008). No changes in directionality were observed. Thus, movement away from cell bodies in these axons can be classified as plus-end directed and anterograde.

To evaluate the behavior of APP vesicles in a control background, we used single particle tracking to acquire a dataset of high spatial (0.126 micron) and temporal (10Hz) resolution trajectories of APPYFP movement (Fig. 2-1A-B; also see Methods). Because our method allows tracking of vesicle movement in single axons, the resulting exceptional clarity enabled quantitative evaluation of the behavior of many moving vesicles. A standard dataset consisted of 10 individual animals of a given genotype imaged in a defined region approximately 900 μm from the neuronal cell bodies in the ventral ganglion. The field size imaged was 88 μm in length, and 4 video segments were recorded from each animal with each video segment being 15 seconds (sec) long (Fig. 2-1A-B).

In APPYFP control animals, 32.3% (s.e.m. = 2.3%; n=10 animals; total number

of analyzed vesicle trajectories = 1890) of measured vesicles moved anterogradely (i.e. towards synapses), 18.2% (s.e.m. = 2.1%) moved retrogradely (i.e. towards neuronal cell bodies), and a surprisingly high percentage (~40.4%; s.e.m. = 4.0%) of vesicles remained stationary (Fig. 2-1C; see Appendix for all terms and cargo motion descriptors used). In addition, 9.1% (s.e.m. = 1.2%) of vesicles reversed direction (Fig. 2-1C). The average frequency of directional switches was 6.09 switches/minute (s.e.m. = 0.25 switches/minute; n = 174 trajectories) with some vesicles reaching frequencies as high as 20 switches/minute. Strikingly, switches generally did not involve pausing: among the 232 reversals detected, only 8.6% coincided with pauses, consistent with a previous report of lipid droplet transport in *Drosophila* embryos (Welte et al., 1998). Thus, directional switches are mediated by an apparently instantaneous change in the balance of active motors.

### 2.2.2 Anterograde kinesin-1 driven APP movement exhibits characteristics of non-processive motors

Considerable evidence demonstrates that APP movement is driven by kinesin-1 (Koo, Sisodia et al. 1990; Ferreira, Niclas et al. 1992; Amaratunga, Morin et al. 1993; Simons, Ikonen et al. 1995; Tienari, De Strooper et al. 1996; Kamal, Stokin et al. 2000; Szodorai, Kuan et al. 2009). Strikingly, we observed that a substantial fraction of APPYFP vesicles traveled at velocities faster than those observed for kinesin-1 motors in vitro, consistent with previous reports (Kaether, Skehel et al. 2000; Stamer, Vogel et al. 2002; Goldsbury, Mocanu et al. 2006). This feature was revealed by analysis of segmental velocities, defined as velocities within a moving vesicle trajectory segment unbroken by a pause (see Appendix). The mean anterograde segmental velocity was 0.86

μm/sec (s.d. = 0.55 μm/sec; n = 1430 segments) (Fig. 2-1D), similar to the highest mean velocity of 0.8 μm/sec reported for single or multiple kinesin-1 motors in vitro (Howard, 2001). However, the distribution of anterograde segmental velocities had a long tail towards higher values, with 41% of vesicles moving faster than 0.8 μm/sec and 13% of vesicles moving faster than 1.6 μm/sec (Fig. 2-1D). The maximal anterograde segmental velocity was 2.85 μm/sec.

The observation that in vivo APP transport can be substantially faster than kinesin-1-driven movements in vitro is in apparent conflict with the well established and generally accepted high processivity of kinesin-1-driven movement in vitro (Howard, Hudspeth et al. 1989; Block, Goldstein et al. 1990; Spudich 1990). The substantial in vitro processivity of kinesin-1 is revealed by the absence of any correlation between motor number and velocity generated although run-length and motor number is highly correlated. It was argued (Spudich 1990) that kinesin-1 processivity in vitro originates from a mechanochemical cycle during which the kinesin-1 motor is strongly bound to the microtubule for almost 100% of the time (Howard 2001). Thus, under these in vitro conditions, multiple kinesin-1 motors generate longer runs but no velocities faster than that of a single motor. Consistent with this view, ATPase measurements in vitro reveal that the most active kinesin-1 ATPase rates are sufficient, but do not exceed, the rate needed to sustain the typical in vitro velocity of 0.8 μm/sec if hydrolysis of 1 ATP generates an 8 nanometer step (Schnitzer and Block 1997; Howard 2001). Although it has been suggested (Kural, Kim et al. 2005) that velocities as high as we and others observe are generated by multiple kinesin-1 molecules working together in vivo, this proposal has not been tested directly. In fact, this is not only inconsistent with in vitro biophysical and

biochemical analyses but also with recent in vivo observations of lipid droplet movement in the *Drosophila* embryo, suggesting that neither velocity nor run-length vary when kinesin-1 amounts on lipid vesicles are varied (Shubeita, Tran et al. 2008).

To test whether kinesin-1 movement in vivo might be less processive and therefore more amenable to cooperation than kinesin-1 in vitro, we used genetic, biochemical, and statistical analyses of APP vesicles to test several key predictions of the hypothesis that high velocity movements are generated by increasing the number of active kinesin-1 molecules on vesicles and that the processivity behavior of kinesin-1 in vivo is substantially different from that observed in vitro.

A first prediction of the hypothesis that the number of active kinesin-1 motors on APP vesicles determines velocity is that the distribution of velocities should be non-normal with multiple modal peaks reflecting differential motor occupancy of vesicles. To evaluate this possibility, we conducted statistical mode analysis (Fraley and Raftery, 2002) on the segmental velocity distributions of anterograde APPYFP vesicle populations (see Appendix). We found that the anterograde velocity distribution was best fit by three modes (Fig. 2-1E) with the first mode at ~0.4 μm/sec and apparent multiples at ~0.8 μm/sec (2X) and 1.6 μm/sec (4X). Thus, the lowest velocity mode in the anterograde direction was slower than the maximal mean velocities of individual kinesin-1 motors measured in vitro, the second largely equivalent to maximal mean velocities in vitro, and the third significantly faster. Nonetheless, this first prediction is fulfilled.

A second prediction of the hypothesis that kinesin-1 motor number determines vesicle behavior in vivo is that faster velocities would require more non-processive behavior. An important characteristic of non-processive motor behavior is the direct

coupling between the velocity and run-length (or pause frequency) of cargos (Spudich 1990). For a system of highly processive motors, these two variables would be independent such that run-length (or pause frequency) would depend upon motor number but velocity should be effectively constant or have no obvious correlation with run-length or pause frequency. Alternatively, non-processive motors are predicted and observed to show strong dependence of both run-length and velocity on motor number with a unique prediction that run-length or pause frequency should show a strong dependence on velocity (Spudich 1990). Because of our relatively short observation window of 15 sec, the run-lengths of many vesicles are truncated. Therefore, we evaluated for non-processive behavior by testing for a correlation of segmental velocity with pause frequency. For control, the correlation coefficient was - 0.45 for the anterograde direction, with the negative sign indicating that the faster the cargo the lower the average probability of a pause (Fig 2-2I). This is consistent with the prediction of kinesin-1 behaving as a non-processive motor in vivo. The observed level of correlation is significantly higher than the correlation of random pairings drawn from the same distributions of velocities and pause frequencies whose mean is effectively zero (magnitude < 0.0001) and standard deviation is ~0.04 (see Appendix). Thus, the second prediction is also fulfilled.

A third prediction of the hypothesis that kinesin-1 can exhibit non-processive or coordinated behavior in vivo is that reducing the amount of kinesin-1 on vesicles should shift the distribution of velocities to lower modes with preferential loss of higher modes and with no generation of new modal velocities. We tested this possibility by performing experiments where kinesin-1 gene dosage was only partially reduced rather than

completely removed. This approach circumvents the issues of organismal lethality and other cellular defects reported in previous in vivo analyses of vesicle or organelle movement where key motor protein subunits were completely removed (Boylan and Hays, 2002; Gindhart et al., 1998; Hurd and Saxton, 1996). Thus, we analyzed APP transport in animals heterozygous for null mutations, i.e., two KHC reduction genotypes, $khc^{8}$/+ and $khc^{20}$/+, and one KLC reduction genotype, $klc^{8ex94}$/+. We expected that this approach would lead to approximately 50% reduction in kinesin-1 abundance. Indeed, Western blot analysis confirmed this expectation and demonstrated that the removal of one functional khc or klc gene caused approximately a 50% reduction in KHC or KLC protein, respectively (Fig. 2-2A-C). Interestingly, reduction of one functional khc gene also resulted in KLC protein reduction whereas removal of one functional klc gene did not affect KHC protein levels. Thus, KLC protein levels appear to depend on KHC but not vice-versa, which agrees with previous work in *Drosophila* S2 cells (Ligon et al., 2004).

To test whether reduction in kinesin-1 gene expression translates to less kinesin-1 motor protein assembly on vesicles, we used bottom loaded sucrose flotation step gradients. In our experimental design, a fraction at the interface of the 8% and 35% sucrose step consists of floated membranes and vesicles. We found that 50% khc gene reduction leads to approximately 50% reduction in both KHC and KLC proteins (Fig. 2-2D-E). Thus, reduction in khc expression translates into total reduction in kinesin-1 levels as well as in kinesin-1 associated with vesicles.

To test whether this reduction of kinesin-1 motor protein on vesicles shifts the distribution of velocities in a manner predicted for a non-processive motor, we evaluated

both duration-weighted and unweighted segmental velocities. Duration-weighted segmental velocities allow us to evaluate the average velocity behavior that vesicles exhibit per time spent moving while unweighted segmental velocities report the average of the velocity distribution (i.e., the average velocity value occupied without considering the duration of different trajectory segments). Analysis of kinesin-1 reduction genotypes reveals strong and generally inhibitory effects on APP movement. We observed substantial decreases in APPYFP average duration-weighted segmental velocity (Fig. 2-2F), average unweighted segmental velocities, and run-length as well as substantial increases in pause frequency and pause duration. Reduction of either KHC or KLC proteins also leads to large increases in the fraction of vesicles that are stationary while decreasing the fraction of vesicles that are moving in either direction or switching movement direction. Thus, the behavior of APP is very sensitive to the level of kinesin-1 present on vesicles, which differs fundamentally from a previous report of lipid droplet transport in *Drosophila* embryos (Shubeita, Tran et al. 2008).

To further evaluate this finding, we extended the statistical mode analysis (Fraley and Raftery, 2002) to the vesicle velocity distributions of anterograde populations in kinesin-1 reduction genotypes (see Appendix). Like controls, the anterograde velocity distribution of kinesin-1 reductions was best fit by three modes (Fig. 2-2G). Importantly, as predicted above for the scenario of non-processive motors, the mode velocities for kinesin-1 reductions remained unchanged compared to control. However, there were significant shifts in the relative population of each mode in kinesin-1 heterozygotes (Fig. 2-2H, Table 2-1). For example, the decrease in anterograde velocity observed in $khc^{8}/+$ was accompanied by an increase in the population of cargos belonging to the slowest

mode 1 (from ~26% in control up to 54% in $khc^{8}/+$) mostly at the expense of vesicles in the fastest mode 3 (from 34% in control down to 13% in $khc^{8}/+$) (see Table 2-1 and Fig. 2-1E, 2-2G). Other kinesin-1 reduction genotypes showed similar behavior. These biochemical and genetic findings are consistent with the notion that the number of functional kinesin-1 motors assembled per cargo is reduced in the kinesin-1 reduction genotypes, causing a decrease in the anterograde velocity and a shift in the occupancy of modal velocities. Thus, not only is the third prediction fulfilled, but these experiments also suggest that APP behavior is very sensitive to the level of kinesin-1 on vesicles unlike lipid droplet transport in *Drosophila* embryos (Shubeita, Tran et al. 2008).

A fourth prediction of the hypothesis that kinesin-1 can be non-processive in vivo is that the correlation of velocities and pause frequency should be preserved when kinesin-1 dosage is reduced. For all kinesin-1 reduction genotypes, the magnitude of these correlation coefficients was in the range of -0.45 to -0.55 for anterograde movement (Fig. 2-2I); the correlation coefficient under random pairing is effectively zero (all magnitudes < 0.0001) whereas the maximum $3\sigma$ is ~0.15 (Fig. 2-2I red line). Thus, these coefficients are highly significant. As for the control data, the negative correlation coefficients indicate that the faster the cargo the lower the average chance for a pause, fulfilling the fourth prediction for non-processive motor behavior.

A potentially important concern about our analyses is whether kinesin-1 reduction causes non-specific global toxicity to axonal transport, which might affect the movement of APP vesicles. There are several observations that suggest this problem is not a major feature in our data. First, many studies have reported that kinesin-1 reduction leads to axonal swellings and vesicle accumulations (Gunawardena and Goldstein, 2001; Hurd

and Saxton, 1996; Martin et al., 1999). While axonal swellings were observed in our kinesin-1 reduction genotypes, they were generally found in distal axonal regions as opposed to the more proximal region that we analyzed. Second, non-selective poisoning would likely shift modal velocity values as opposed to the shifts in mode distributions that we observed. Third, if global toxicity were a cause of velocity changes, both kinesin-1-dependent and independent transport would be impaired. To test this idea, we analyzed the movement of synaptotagmin (SYT), a kinesin-3 cargo (Pack-Chung et al., 2007; Yonekawa et al., 1998), in $khc^{8}$/+ and $klc^{8ex94}$/+ animals. Despite minor differences, including modest stimulation of movement, no substantial or consistent changes in SYT-GFP movement were observed (data not shown). Thus, non-specific global toxicity seems an unlikely mechanism underlying the effects of kinesin-1 reduction on APP movement.

### 2.2.3 Kinesin-1-driven anterograde velocity modes are relatively stable

Current proposed models of vesicle movement make somewhat different predictions about the stability of vesicle movement behavior during axonal transport. For example, models in which motor proteins actively associate and dissociate with vesicles to determine direction of movement or pausing predict that movement parameters would vary over time (e.g., before and after pauses). Alternatively, models that invoke stable loading of vesicles in neuronal cell bodies predict substantial stability of movement before and after pauses and during runs. In fact, a prediction of the hypothesis that varying kinesin-1 motor amounts on APP vesicles controls their behavior is that while the distribution of velocities is broad, the velocity of any given vesicle should remain relatively stable if motor number does not change over time. To probe these issues, we

focused on analyzing movement behaviors relative to pauses, which punctuate runs and define run-lengths. We established two different measures for pause frequency (see Experimental Procedures). First, we calculated for each pause event the inverse of the duration of the preceding segment. The mean value of this measure defines how often a motion segment is interrupted by a pause. Hence, this parameter is referred to as the segmental pause frequency. Of note, only the pause events whose preceding motion segment is not truncated at the beginning of the 15-sec observation window contribute to this measurement. Accordingly, this value tends to overestimate the frequency of pausing. Thus, we also calculated the total pause frequency (i.e. the number of pause events divided by the total time in motion), which includes all 15 sec vesicle tracks in the dataset. Anterograde APPYFP vesicles in control animals had a segmental pause frequency of 1.45 pauses/sec (s.e.m = 0.09 pauses/sec; n = 767 pauses), a total pause frequency of 0.11 pauses/sec (s.e.m. = 0.01 pauses/second; n = 695 tracks), and a mean pause duration of 1.55 sec (s.e.m = 0.05 sec; n = 767 pauses). Consistent with the infrequent pauses, APP vesicles in vivo exhibited substantially longer run-lengths compared to kinesin-1-driven movements in vitro. The observed average run-length of anterograde APPYFP cargos is 7.63 μm (s.e.m. = 0.26 μm; n = 1430 segments), which is substantially higher than the typical 1-2 μm reported for kinesin-1 in vitro (Howard, Hudspeth et al. 1989; Block, Goldstein et al. 1990). Since our cargo trajectories are truncated spatially and temporally, we also estimated true run-lengths by dividing the mean segmental velocity by the total pause frequency (see Appendix). The estimated bulk run-length for anterograde vesicle movement is 11.7 μm, which is also substantially longer than the run-lengths reported in most other in vivo systems (e.g., (Gross et al.,

2002)). These findings may reflect mechanistic differences in fulfillment of fundamentally different biological requirements between short-distance cellular transport and long-distance axonal transport in polarized neurons. Of note, we confirmed the existence of these predicted longer run-lengths by recording longer-duration movies (2 minutes of continuous imaging). The anterograde run-length was 21.85 μm (s.e.m. = 2.3 μm; n = 47 segments).

We further probed the stability of APP movement by asking how often vesicles change their velocity modes within a run and whether their velocity modes are changed by pauses. Accordingly, we calculated the probability that an APPYFP vesicle changes 0, 1, or 2 velocity modes between the start and end of a segment (i.e., between the time points before and after a pause) (see Appendix). The probability that a vesicle did not switch velocity modes within an anterograde run was 0.49. The probability for a one-mode-switch was 0.41, and the probability for a two-mode switch was 0.10. The probabilities for mode switch after a pause were 0.59 for no-mode, 0.38 for one-mode, and 0.03 for two-mode. These values have to be compared to the probabilities for mode switches by chance, which are derived from the different population sizes associated with each mode: 0.34 for no switch, 0.48 for a one-mode switch, and 0.18 for a two-mode switch. Thus, velocity modes are relatively stable during runs and after pausing.

**2.2.4 Kinesin-1 effects on retrograde transport**

Kinesin-1 inhibition or reduction was previously reported to impair retrograde transport (Brady et al., 1990; Colin et al., 2008; Kim et al., 2007; Martin et al., 1999; Pilling et al., 2006). To test for such effects, we first established baseline behavior of retrograde APP transport under control conditions. We found that the distribution of

APPYFP retrograde segmental velocities (mean ± s.d.: 0.87 ± 0.45 μm/sec; n = 907 segments) has a substantially higher mean and standard deviation compared to cytoplasmic dynein velocities in vitro (King, 2000; Reck-Peterson et al., 2006) (Fig. 2-3A). The maximal retrograde velocity observed in control animals was 3.14 μm/sec. We also found that the retrograde distribution in controls showed two strong modes and a third weaker mode (Fig. 2-3B; Table 2-1). In addition, as with anterograde movements, retrograde movements exhibited generally stable behavior. The probability for no-mode switch within a retrograde run was 0.58, for a one-mode switch 0.39, and for a two-mode switch 0.03. Again, the values for no-mode switch or one-mode switch substantially exceed the probabilities for switches by chance (0.47 for no-mode switch, 0.48 for a one-mode switch, and 0.05 for a two-mode switch). The probability for no-mode switch after a pause was 0.72, for a one-mode switch 0.28, and for a two-mode switch 0.003. We also observed longer retrograde run-lengths in vivo than reported in vitro. The observed mean retrograde run length was 7.08 μm (s.e.m= 0.26 μm, n= 907 segments), which leads to an estimated bulk run-length of 13.2 μm. The estimated retrograde bulk run-length, confirmed by longer-duration recording as for anterograde, was 14.18 μm (s.e.m. = 2.7 μm; n = 26 segments).

Our analysis of khc and klc gene dosage reduction revealed substantially impaired retrograde transport. As observed for anterograde movement, we found significant decreases in APPYFP duration-weighted retrograde segmental velocities (Fig. 2-3C), unweighted segmental velocities, and a major shift in occupancy, but not value, of velocity modes (Fig 2-3D-E). In addition, we observed a significant decrease in retrograde run-lengths as well as significant increases in retrograde pause frequencies and

durations. Retrograde vesicles had a segmental pause frequency of 1.48 pauses/sec (s.e.m. = 0.12 pauses/sec; n = 434 pauses), a total pause frequency of 0.09 pauses/sec (s.e.m. = 0.01 pauses/sec; n = 439 tracks), and mean pause duration of 1.46 seconds (s.e.m. = 0.06 sec; n = 434 pauses). Consistent with the observation that heterozygosity for khc gene reduces both KHC and KLC protein levels, $khc^{8}$/+ and $khc^{20}$/+ generated more pronounced effects on retrograde transport as compared to $klc^{8ex94}$/+. Thus, kinesin-1 plays an important role in bidirectional transport as proposed previously (Kim et al., 2007; Martin et al., 1999; Pilling et al., 2006). In addition, we observed that both KLC and KHC subunits play a similar role, which differs from previous studies where only KHC was reported to make a significant contribution (Ling et al., 2004).

There are two obvious possibilities for why retrograde transport of APP is diminished in kinesin-1 reductions: 1) Loss of kinesin-1 leads to reduced cytoplasmic dynein loading; and/or, 2) Loss of kinesin-1 leads to reduced activation of cytoplasmic dynein on vesicles (Ally, Larson et al. 2009). In our flotation experiments, we noted that DHC protein levels in $khc^{8}$/+ remained unchanged in the PNS and exhibited only a minor (15%) decrease in the 8/35 fraction (Fig 2-2D-E). Thus, loss of kinesin-1 appears to not lower significantly the amounts of cytoplasmic dynein on floated vesicles.

The possibility that loss of kinesin-1 leads to reduced cytoplasmic dynein activation on APP vesicles cannot be tested directly in our system with methods currently available. However, a prediction of this hypothesis is that overexpression of kinesin-1 or its subunits would lead to increased cytoplasmic dynein activation. Thus, we overexpressed khc, klc, or both together by generating animals carrying khc and klc genomic transgenes either singly or together (GEN-KHC and GEN-KLC). Western blot

analysis of GEN-KHC showed increase in both KHC and KLC proteins by ~50-100% whereas only KLC protein was increased by 50-100% in GEN-KLC (Fig. 2-4A-C). Furthermore, simultaneous overexpression of khc and klc led to nearly 100% increase in KHC protein but a much higher (~300%) increase in KLC protein (Fig. 2-4A-C). Thus, consistent with the reduction experiments, KLC protein levels appear to depend on KHC but not vice-versa.

Examination of APPYFP movement revealed that kinesin-1 overexpression impaired both anterograde and retrograde transport. Significant decreases in duration-weighted segmental velocities (Fig. 2-4D-E), unweighted segmental velocities and run-lengths, as well as significant increases in vesicle pause frequencies and durations were observed. Qualitatively, these changes were similar to kinesin-1 reduction although transport impairment by overexpression was generally milder. However, kinesin-1 reduction and overexpression differed dramatically in how they changed the cargo population distribution. While reduction caused significant increases in the fraction of stationary vesicles and significant decreases in moving vesicles, overexpression did not change the percentage of stationary vesicles but rather led to a slight increase in anterograde and decrease in reversing populations. This observation indicates that increased kinesin-1 levels may give mild, although barely significant, activation of anterograde movement but does not support the hypothesis that kinesin-1 activates cytoplasmic dynein.

Closer examination of our data suggested a third possibility to account for the effects of kinesin-1 reduction and overexpression on retrograde transport. Specifically, we observed a significant decrease in the total number of APPYFP vesicles in kinesin-1

reductions as compared to overexpression. This observation raises the possibility that kinesin-1 reduction and overexpression may impair APP movement by two different mechanisms. For overexpression, excess kinesin-1 protein may interfere with bidirectional movement by either sequestering essential soluble factors or directly inhibiting cytoplasmic dynein activity (see below). In the case of kinesin-1 reduction, however, the decrease in anterograde movement may indirectly affect retrograde movement by generating a sampling bias. Specifically, our data reveal that the number of moving vesicles dropped from ~30 to ~10 in all three kinesin-1 reduction genotypes (Fig. 2-2-2-4F), and this was accompanied by a highly significant increase in the fraction of stationary cargos. No other genotype exhibited a similarly significant reduction in total number of cargos. This proposed sampling phenomenon can lead to an apparent impairment of retrograde transport related to the limited combinations of kinesin-1 and cytoplasmic dynein associated with vesicles within the axonal shaft (see Fig. 2-4G-H).

**2.2.5 Reduction of dynein and dynactin subunits confirms that non-processivity and modal stability are generic features of kinesin-1 driven APP transport**

We evaluated cytoplasmic dynein and dynactin reduction genotypes to further probe motor protein coordination and attachment to APP vesicles. Evaluation of these genotypes also allowed us to test whether the apparent non-processivity and stability of movement behavior are general features across a range of genetic conditions. Thus, we analyzed vesicle movement in two dynein heavy chain (DHC) reduction genotypes, $dhc64c^{4\text{-}19}/+$ and $dhc64c^{p4163}/+$ (both null or near-null alleles); one dynein light chain (DLC) reduction genotype, $robl^{k}/+$, and two dynein intermediate chain (DIC) reduction genotypes, $dic^{1}/+$ and $dic^{3}/+$. The $dhc64c^{p4163}$ allele has an internal 122 basepair deletion

of nucleotides 5750-5871 (with respect to the Dhc64C cDNA), which is predicted to remove P-loop1 and lead to premature termination of translation upstream of P-loops 2-4. Western blot analysis of these mutations confirmed that dhc64c$^{4-19}$ and dhc64c$^{p4163}$ are null or near-null (Fig. 2-5A).

To test whether removal of one functional dhc gene leads to reduction in DHC protein, we performed quantitative Western blot analysis on dhc64c$^{4-19}$/+ and dhc64c$^{p4163}$/+ animals. As expected, we observed approximately a 50% and 60% reduction in protein levels for dhc64c$^{4-19}$/+ and dhc64c$^{p4163}$/+ respectively (Fig. 2-5B). Because DIC levels have been reported to change with dhc reduction (Caviston et al., 2007; Colin et al., 2008), we also probed dhc64c$^{4-19}$/+ and dhc64c$^{p4163}$/+ for DIC. Indeed, we observed that DIC levels are reduced by approximately 50% in dhc64c$^{4-19}$/+ and dhc64c$^{p4163}$/+. Similarly, ROBL levels are reduced in these genotypes.

In dhc64c$^{4-19}$/+ and dhc64c$^{p4163}$/+ no significant changes in anterograde duration-weighted segmental velocities were observed (Fig. 2-5C) whereas retrograde segmental velocities were significantly reduced as expected (Fig. 2-5D). Since duration-weighted segmental velocities emphasize velocities with long durations, we also examined the distribution of unweighted segmental velocities. We found significant increases in the mean values of anterograde segmental velocities of both dhc64c$^{4-19}$/+ and dhc64c$^{p4163}$/+ accompanied by the expected decrease in retrograde segmental velocities. Anterograde run-lengths in dhc64c$^{4-19}$/+ and dhc64c$^{p4163}$/+ also exhibited significant increases while retrograde run-lengths were decreased. Analysis of velocity modes revealed that in controls, the retrograde distribution showed two strong modes and a third weaker mode (Fig. 2-5E). In both dhc64c/+ allelic reductions, we observed shifts to slower modes as

compared to control (Table 2-1). In addition, DHC reduction caused significant increases in anterograde and retrograde pause frequencies and durations (Table 2-1) and a small increase in the fraction of anterograde vesicles at the expense of reversing and stationary vesicles. In summary, DHC reduction impairs retrograde transport but enhances a number of features of anterograde transport. Hence, DHC acts generally as an inhibitor of anterograde transport and is required, as expected, for retrograde transport. In addition, this apparent inhibition of kinesin-1 mediated transport by DHC does not readily fit the proposed tug-of-war mechanism for bi-directional transport proposed by Ally and colleagues (Ally, Larson et al. 2009) (also see Discussion).

To assay the effect of dlc reduction on vesicle movement, we used a deletion allele of the robl gene (Bowman et al., 1999). Western blot analysis indicated that the removal of one functional robl gene caused approximately a 20% reduction in DLC. Probing for DHC and DIC, we observe a 70% and 30% reduction respectively. Thus, there is a significant reduction of DHC in $robl^{k}$/, but DIC and DLC levels are only mildly decreased. Changes to anterograde and retrograde transport in $robl^{k}$/+ show similar trends as for dhc/+. We observed impairment of retrograde transport (Fig. 2-5D) and improvement in anterograde transport in terms of increased run-length and a higher percentage of anterograde cargos. However, other changes to anterograde and retrograde transport were not significant.

To assess the effect of dic reduction on vesicle movement, we used two loss-of-function alleles (Boylan and Hays, 2002). Western blot analysis in $dic^{1}$/+ and $dic^{3}$/+ showed 70% and 40% reduction in DIC protein respectively. These changes are consistent with the idea of $dic^{1}$ being a stronger reduction allele than $dic^{3}$ (Boylan and

Hays, 2002). Interestingly, DHC and ROBL protein levels are also significantly decreased in $dic^{1}$/+ and $dic^{3}$/+, with DHC being reduced by 75% and 45% and ROBL approximately 50% and 40% respectively. In contrast to DHC and DLC reduction, DIC reduction resulted in impairment of all anterograde and retrograde APPYFP transport parameters in $dic^{1}$/+ and $dic^{3}$/+. Significant reductions were observed in anterograde and retrograde duration-weighted segmental velocities (Fig. 2-5C-D), unweighted segmental velocities, and run-lengths. In addition, we observed significant increases in pause frequencies and durations (Table 2-1). Furthermore, DIC reduction caused a significant increase in the fraction of stationary vesicles and a significant decrease in the fraction of reversing vesicles. However, $dic^{1}$/+ and $dic^{3}$/+ showed some minor variability in how the fractions of anterograde and retrograde vesicles were changed.

Dynactin has been proposed to have a number of functions in vesicle transport (Schroer, 2004). These include promotion of dynein processivity via binding to microtubules (King and Schroer, 2000) and/or attachment of dynein to vesicles (Karki and Holzbaur, 1995, 1999). However, recent work (Haghnia et al., 2007; Kardon et al., 2009(Kim, Ling et al. 2007) does not support these proposals. Dynactin has also been proposed to coordinate kinesin and dynein activities (Gross et al., 2002). Disruption of the dynactin complex via arp1 deletion or p50 overexpression leads to bidirectional impairment in axonal transport (Haghnia et al., 2007; Kwinter et al., 2009). To probe the role of dynactin in APP movement, we used three reduction genotypes of distinct subunits: $dmn^{5499}$/+, a p50/dynamitin loss-of-function allele; $Gl^{1}$/+, a $p150^{Glued}$ dominant negative allele; and grid/+, an Arp1 loss-of-function allele. Protein reduction in these backgrounds was assessed via Western blot. In grid/+, we observe a 40% reduction in

ARP1 protein and approximately 50% reduction in p50. The levels of p150 could not be evaluated due to lack of an effective antibody (see Methods). As for $dmn^{5499}/+$, we observe a 50% reduction in both p50 and GRID proteins.

Reduction of p50/dynamitin caused mild decreases in the means of APPYFP retrograde duration-weighted and unweighted segmental velocities but did not significantly change anterograde velocities (Fig. 2-5G). However, it impaired transport in both directions by increasing pause frequencies and durations (Table 2-1). In addition, the fractions of vesicles shifted towards more anterograde at the expense of lower contributions from the other three classes. Perturbation of $p150^{Glued}$ and Arp1 caused stronger transport impairment in terms of reduced duration-weighted segmental velocities, segmental velocities, and run-lengths (Fig. 2-5G-H). However, the impairment was less pronounced in terms of increased means of pause frequencies and durations (Table 2-1). Changes to cargo populations in $Gl^{1}/+$ and grid/+ were mild but also indicated transport impairment. Overall, these data confirm that dynactin is required to promote anterograde and retrograde transport although the transport impairment associated with perturbation of any of its three subunits is milder than those associated with perturbation to kinesin-1 and cytoplasmic dynein.

Taken together, the effects of cytoplasmic dynein and dynactin reduction on parameters of mode stability and processivity revealed that the behavior of these parameters mirrored the findings in control and kinesin-1 dosage reduction genotypes. Specifically, correlations of velocity and pause frequency were maintained, supporting the hypothesis of non-processivity of kinesin-1- driven APP movement in vivo. Similarly, stability of modes was comparable.

### 2.2.6 Stimulation of anterograde transport by overexpression of DIC

Cytoplasmic dynein has been previously proposed to serve as an activator of kinesin-1 (Kim et al., 2007; Ling et al., 2004; Martin et al., 1999; Pilling et al., 2006). Previous biochemical data established that the only detectable interactions between kinesin-1, cytoplasmic dynein, and dynactin protein complexes are mediated by DIC. Interactions were reported between DIC and $p150^{Glued}$ (Vaughan and Vallee, 1995) and DIC and KLC (Ligon et al., 2004). Both binding interactions involve similar regions of DIC (Vaughan and Vallee 1995; Ligon, Tokito et al. 2004; Schroer 2004). Hence, it might be possible that motor protein activity on APP vesicles is controlled by a competition between $p150^{Glued}$ and KLC for binding to DIC. Consistent with this idea, we noted that compared to DHC and DLC reduction, DIC reduction by far caused the strongest and most consistent impairment of cargo transport in both directions.

If DIC controls the balance between anterograde and retrograde transport, a key prediction is that overexpression of DIC would stimulate anterograde transport by binding to KLC and activating kinesin-1. To test this idea, we increased DIC protein levels by overexpressing a genomic transgene, GEN-DIC (Boylan and Hays 2002). The overexpression of dic in this background is confirmed by Western blot analysis showing 100% increase in DIC protein. Indeed, we observed a slight increase in unweighted anterograde segmental velocity in GEN-DIC. Most strikingly, the GEN-DIC genotype was associated with significant increases in both anterograde run-length and fraction of anterograde APPYFP vesicles. This increase in anterograde vesicle fraction was accompanied by a significant decrease in the fraction of stationary and reversing vesicles.

We also noted that GEN-DIC has an increased population of cargos with

velocities in mode 1 (slowest velocity mode; Fig. 2-6C-D). If the modes relate to numbers of functional motors assembled on the vesicles, this result would indicate that higher DIC concentrations compete with the proper assembly of kinesin-1. On the other hand, GEN-DIC markedly raised the anterograde modal velocities of vesicles in mode 3 (Table 2-1 and Fig. 2-6C), supporting the notion that DIC acts as a promoter of kinesin-1 activity. Of note, the differential effects of DIC on mode decomposition (i.e. increase of the population of mode 1 and increase of the mean velocity of mode 3) cancel each other in the distributions of anterograde segmental velocities (Fig. 2-6C). This seemingly contradictory finding explains why the average anterograde velocities remained relatively unchanged compared to control even though the increased anterograde population and extended run-lengths supported DIC's enhancement of kinesin-1-driven cargo transport. Thus, these data support the idea that DIC acts as a promoter of anterograde transport. Of note, we also observed that overexpression DIC increased bidirectional pause frequency and duration (Table 2-1). Because this occurred in both anterograde and retrograde directions and without reduction in duration-weighted segmental velocities (Fig. 2-6A-B), it is possible that increased density of non-APP vesicles (obstacles) along the axon indirectly interferes and/or temporarily stalls vesicle movement in this genotype.

## 2.3 Discussion

In this study, we used modest genetic alterations in kinesin-1, cytoplasmic dynein, or dynactin subunits to probe specific mechanisms of axonal transport in vivo. Computer-assisted quantification of the precise behavior of large numbers of APPYFP axonal vesicles allowed us to achieve sufficient sensitivity for robust interpretation of weak phenotypes in the absence of organismal inviability. We discovered several novel features of the effects of reduced or increased amounts of cytoplasmic dynein, kinesin-1, and dynactin on parameters of APP axonal transport in vivo. First, vesicle movement driven by kinesin-1 in vivo has crucial differences from that of in vitro. Specifically, while kinesin-1-driven movement in vitro is highly processive, in vivo movement exhibits strikingly non-processive behavior. This can be demonstrated by a number of criteria and points to fundamental alterations in motor properties in vivo relative to in vitro. Second, APPYFP vesicles moving in axons exhibit relatively consistent modal velocities, suggesting the presence of stable motor assemblages on vesicles. In fact, our genetic, motility, and biochemical evidence strongly suggests that the number of kinesin-1 motor proteins associated with APP vesicles dictate their properties, which is fundamentally different from what has been previously reported for lipid droplet movement (Shubeita, Tran et al. 2008). Third, as discussed below, our data agree with other reports that do not support simple tug-of-war and exclusionary presence models (Gross, 2004). Instead, our data suggest a new and testable motor competition-coordination model of axonal transport.

### 2.3.1 Does the amount of kinesin-1 on APP vesicles control movement parameters?

Considerable in vitro biochemical and biophysical evidence has led to the prevailing view that kinesin-1 is highly processive. This high degree of processivity has the important consequence that the velocity of cargos driven by multiple kinesin-1 motors cannot exceed the velocity of cargos driven by a single motor. It has been suggested that this highly processive behavior is generated because the strongly bound state time of the kinesin-1 motor domain is a large fraction of the total mechanochemical cycle time and because binding and release of the two heads of the kinesin-1 dimer are tightly coordinated (Spudich 1990; Howard 2001; Gennerich and Vale 2009). By reducing the probability that a cargo dissociates from a microtubule during its journey to a distant destination (e.g., cell body to synapse), such behavior has been postulated to be important for generating long-distance vesicle movement in vivo by single or small numbers of kinesin-1 motors. Structural studies suggest that axonal vesicles in vivo associate with multiple motors (Hirokawa 1982). However, numerous in vivo studies have reported kinesin-1 velocities that are too fast to easily reconcile with in vitro findings. Our study establishes that, at least for APP vesicles, kinesin-1-driven movements in vivo are not highly processive. Specifically, we found that a 50% reduction of kinesin-1 gene dosage results in fewer motors on floated vesicles. Such reductions generate shorter run-lengths and reduced velocities resulting from decreased occupancy of higher order velocity modes as compared to control. Finally, the coupling of run-length and velocity, a hallmark of low processivity motor behavior, was confirmed by the significant negative correlation between anterograde pause frequency and velocity.

Although a molecular explanation for this non-processive movement of kinesin-1 is lacking, recent work suggests that regions adjacent to the motor domain may control motor coordination (Crevenna, Madathil et al. 2008). Notably, previous work on the biophysical behavior of the coil 1 domain of KHC suggests that this structured alpha-helical coiled-coil has the unusual ability to melt at physiological temperature (de Cuevas, Tao et al. 1992). This instability could provide a mechanism for reducing coordination within the kinesin-1 dimer, diminishing processivity, and increasing velocity generated by multiple kinesin-1 motors.

Our results also suggest that the assemblage of motors and their activation states on APP vesicles stay relatively constant for the majority of vesicles. Even over the duration of a pause there appears to be a "memory" in the activation state, suggesting that the molecular properties regulating vesicle movement (e.g., the number of active motors) do not vary substantially over the time scale of seconds. These findings also suggest that pause events in vivo are primarily induced by temporary "congestion" of the axonal tracks as opposed to motor dissociation. Taken together, our data suggest that once movement is initiated, cargos under control conditions maintain the same level of motor activation for many seconds. This type of behavior was also noted for lipid droplets (Welte et al., 1998). Within a set motor assemblage, the walking efficiency may vary slightly depending on the local resistance a cargo experiences. Occasionally, the resistance is sufficient to stall or even reverse vesicle motion. However, the same motor configuration is active in a majority of cases when motion resumes. An issue in need of future resolution is whether pause events with velocity mode switches are caused by a

fundamental reconfiguration of active motors or by motor activity changes secondary to axonal "congestion."

We note that our data are largely inconsistent with conclusions from recent work in the lipid droplet system (Shubeita, Tran et al. 2008), which suggest that varying the number of active kinesin-1 or cytoplasmic dynein motors on lipid droplets does not appreciably alter their velocity or processivity. While this finding may be true for the short-range developmentally specific behavior of lipid droplets in the embryo, it clearly cannot account for the APPYFP movement behavior we observed.

### 2.3.2 In vivo behavior of APP axonal vesicles is inconsistent with most current models for control of vesicle movement

In agreement with previous work on lipid droplets, melanosomes, and other non-neuronal cargos, our data do not support simple tug-of-war or exclusionary presence models and are most consistent with coordination models (Gross, 2004; Kural et al., 2005). For example an exclusionary presence model for APP axonal vesicles predicts that reduction of kinesin-1 motors should have either no effect or increased retrograde transport while reduction of dynein motors should have no effect or increased anterograde transport. Similarly, increased kinesin-1 is predicted to have either no effect or increased anterograde activity but reduced retrograde. Our findings are inconsistent with these predictions. As for simple tug-of-war models, the prediction is that simultaneous attachment and activity of opposing motor activities would generate net APP movement in one direction or another depending upon the relative number of each type of motor attached to a vesicle (Muller et al., 2008; Soppina et al., 2009). Thus, reduction of either kinesin-1 or cytoplasmic dynein would be predicted to uniformly

stimulate movement in the opposite direction, which is inconsistent with many of our observations. A more sophisticated tug-of-war model (Ally, Larson et al. 2009) proposes that dynein activity is needed to activate kinesin-1 and vice- versa. Though supported by some of our data, this model is not consistent with all of the observations we have made. For example, kinesin-1 reduction is reported previously as well as here to inhibit dynein-driven movements (Brady et al., 1990; Colin et al., 2008; Kim et al., 2007; Martin et al., 1999; Pilling et al., 2006), which seems consistent with this modified tug-of-war model. However, although in this study we cannot completely exclude direct effects of kinesin-1 reduction on cytoplasmic dynein activity, we propose that the effects of kinesin-1 reduction on dynein-driven retrograde transport represent a sampling bias (i.e., intrinsic to measurements of vesicle transport in regions of the axon distant from cell bodies; see Fig. 2-4F-H). More importantly, our finding that reductions in DHC enhance anterograde movement is inconsistent with the model proposed by Ally and colleagues.

A computational model of motor-driven transport was recently proposed (Muller, Klumpp et al. 2008) in which multiple kinesin and dynein motors interact indirectly via their nonlinear, force-dependent unbinding rates. This yields a non-intuitive coordination mechanism where vesicle movement in a specific direction is driven predominantly by one type of motor. This model makes several specific predictions of transport behavior, which we tested using our vesicle motion data. First, when the plus-end and minus-end directed motors are asymmetric, the model predicts that anterograde and retrograde vesicle movement each follow a single peak velocity distribution. However, our APPYFP motion data reveal that distributions of both anterograde and retrograde velocities are much wider and exhibit multiple modes. Second, the model proposes that stationary

cargos, classified under the category of "no motion," are driven by weak motors with a small ratio of stall to detachment forces. Consequently, the model predicts that a significant increase in the fraction of stationary cargos results from significant increases in both weak plus-end- and minus-end-directed motors. In fact, significant increases in the fraction of stationary cargos are observed in many of our reduction genotypes. For example, KHC reductions ($khc^{8}$/+ and $khc^{20}$/+) are accompanied by a twofold increase in the fraction of stationary cargos, which in this model would require a concurrent increase in the fraction of "weak" dynein motors. We note that this prediction also contradicts the basic assumption of the model that kinesin mutations do not alter the fundamental properties of dynein motors and vice-versa. Finally, changing the parameters of the motors in this model can account for changes to stall force, run length, pause time, and velocity caused by different dynein mutations in the lipid droplet transport system. However, this model cannot account for the changes we observe for APP vesicles in the population distribution of different types of cargos (anterograde, retrograde, stationary, and reversing). For example, this model cannot explain why there is a substantial fraction of stationary APPYFP cargos (~40% in control) and why there are different fractions of anterograde (~32% in control) and retrograde (18% in control) cargos. These arguments suggest that mechanical coordination alone is insufficient to describe the behavior of APP axonal vesicles.

### 2.3.3 A competition-coordination mechanism regulates axonal transport of APP vesicles

In a typical coordination model, vesicles bind to both kinesin-1 and cytoplasmic dynein simultaneously, and a coordination process on the vesicle surface ensures that

both types of motors are not active at the same time (Gross 2004). The predictions of this model are ambiguous given the lack of a defined coordination mechanism. However, if kinesin and dynein themselves are part of the coordination mechanism, this model would predict that reductions of either kinesin-1 or cytoplasmic dynein might impair movements in both directions. For vesicle transport in the lipid droplet system, it was argued that a coordination model of some sort best accounts for the experimental observations (Gross, 2004).

Four observations that we report here for the APP vesicle constrain the type of coordination model that can be proposed. We find that: 1) Reducing kinesin-1 does not reduce cytoplasmic dynein levels on floated vesicles, hence kinesin-1 is not required for cytoplasmic dynein association with vesicles; 2) Overexpression of kinesin-1 does not stimulate dynein-driven retrograde transport, suggesting that kinesin-1 binding to DIC does not stimulate dynein activity; 3) Sampling effects in kinesin-1 reduction may account for reductions in retrograde movement; and 4) Modest overexpression of DIC stimulates a number of features of anterograde movement including the distribution and occupancy of velocity modes and a large increase in the ratio of anterograde to retrograde movement (a shift from 1.8:1 to 2.3:1). Thus, a formal genetic interpretation of our results implicates DIC as an activator of kinesin-1-mediated anterograde transport. Combining these genetic findings with biochemical evidence (Ligon, Tokito et al. 2004) for the ability of DIC to bind $p150^{Glued}$ and KLC in similar regions leads to a simple model in which the activity of kinesin-1 and cytoplasmic dynein is coordinated by competition of dynactin and kinesin-1 for binding to DIC, thereby controlling the direction of movement (Fig. 2-6E). Specifically, this model proposes that the binding of

dynactin to DIC promotes retrograde transport and, in competition with this interaction, binding of DIC and KLC promotes anterograde transport. In addition, excess soluble kinesin-1 generated by modest overexpression of khc, klc, or both is predicted to compete with vesicle-bound dynactin for DIC binding, resulting in impaired activation of cytoplasmic dynein. Similarly, excess kinesin-1 is predicted to compete with vesicle-bound KLC for DIC binding, causing impaired kinesin-1 movement. Indeed, our data exhibit reduced retrograde and anterograde transport with the overexpression genotype GEN-KHC; GEN-KLC (Fig. 2-2D-E). On the other hand, the model predicts that excess soluble DIC binds preferentially to KLC on the APP vesicle resulting in an enhanced bias in anterograde transport. For vesicles in the GEN-DIC genotype, we found a marked increase in the anterograde population, faster average segmental velocities (Table 2-1), faster velocities in the highest velocity mode (mode 3), and extended run-lengths in the anterograde direction. The precise mechanism for the KLC bias in GEN-DIC is an interesting question warranting further investigation.

Taken together, our data provide strong quantitative support for the proposed competition-coordination mechanism. Of note, previous overexpression studies in non-neuronal cells were interpreted to mean that excess DIC poisons retrograde transport (King, Brown et al. 2003). However, unlike our live cell measurements, the fixed cell analyses in previous work could not distinguish inhibition of retrograde transport from stimulation of anterograde transport or a combination of the two. Still, we cannot completely exclude that some aspects of our data might represent indirect effects of protein overexpression on transport (i.e., due to aberrant transport/sequestration of known or unknown regulators of motor proteins). For example, kinesin-1 overexpression did not

yield faster anterograde velocities, indicating that additional regulatory factors are required (Gindhart, Chen et al. 2003; Blasius, Cai et al. 2007). Further investigations will be needed to test the many detailed predictions of our model. In addition, a search for various proteins interacting with $p150^{Glued}$, DIC, and KLC may augment our understanding of how the interactions between DIC, dynactin, and/or KLC may be modulated.

## 2.4 Methods

### Genetics

*Drosophila* stocks were maintained at room temperature or at 25°C except when crosses were set up for imaging. L3 larvae obtained for imaging and movement analysis were taken from crosses incubated at 29°C. The control group used in this study was UAS-APPYFP (X), which has an APPYFP transgene inserted in the X chromosome. Only female L3 larvae were used for imaging of this as well as all other genotypes. In brief, L3 larvae expressing UAS-APPYFP arose from crosses between male UAS-APPYFP flies and SG26.1Gal4 virgin females. Male animals provided an internal control for the cross since they did not express UAS-APPYFP. To examine the effect of motor gene reductions on vesicle movement, we first generatedF an UAS-APPYFP; $pin^{88K}$/T(2:3) CyO TM6B stable stock. The chromosome carrying T(2:3)CyO, TM6B is referred to as B3 and carries the dominant markers Hu, Tb, and Cyo.

For kinesin-1 reduction studies, three alleles were used: $khc^{8}$/CyO, $khc^{20}$/CyO, and $klc^{8ex94}$/TM6B. The *khc* alleles are null point mutants whose translated fragments are thought to be degraded due to instability (Saxton, Hicks et al. 1991; Hurd and Saxton 1996; Hurd, Stern et al. 1996; Brendza, Sheehan et al. 2000). The *klc* allele is a deletion allele spanning the entire *klc* gene in chromosome 3 (Gindhart, Desai et al. 1998). For each of these alleles, virgin UAS-APPYFP; $pin^{88K}$/B3 flies were crossed to $khc^{8}$/CyO, $khc^{20}$/CyO, or $klc^{8ex94}$/TM6B males. Selected male UAS-APPYFP/Y; *kinesin*/B3 were then crossed to virgin SG26.1Gal4 animals, and female non-tubby L3 larvae were selected for imaging.

For cytoplasmic dynein reduction studies, five alleles were used: *dhc64c*$^{p4163}$/TM6B, *dhc64c*$^{4-19}$/TM6B, *dic*$^{1}$/FM7GFP, *dic*$^{3}$/FM7GFP, and *robl*$^{k}$/CyO. The *dhc64c* $^{p4163}$ allele has an internal 122 basepair deletion of nucleotides 5750-5871 (with respect to the Dhc64C cDNA), which is predicted to remove P-loop 1 and lead to premature termination of translation upstream of P-loops 2-4. Western blot analysis of these mutations confirms that *dhc64c*$^{4-19}$ and *dhc64c*$^{p4163}$ are null or near-null alleles (see Western blot analysis in Figure 2-5A). The *dic* alleles have been characterized as loss of function, with *dic*$^{1}$ being functionally stronger than *dic*$^{3}$ (Boylan and Hays 2002). The *dlc* allele *robl*$^{k}$ is a deletion allele spanning the entire *robl* gene (Bowman, Patel-King et al. 1999). For crosses involving *dhc* or *dlc*, we proceeded as with kinesin-1. For *dic* crosses, UAS-APPYFP/Y; SG26.1Gal4/B3 animals were crossed to *dic*$^{1}$/FM7GFP or *dic*$^{3}$/FM7GFP and a GFP microscope was used to select female L3 larvae negative for GFP—these female animals are UAS-APPYFP/*dic*; SG26.1Gal4/+.

For dynactin reduction studies, three alleles were used: *grid*/TM6B, *dmn*$^{5499}$/CyO, and *Gl*$^{1}$/In(3L)D, *d*$^{1}$ (BL-2394). The *grid* allele has been characterized as a loss of function point mutant (Haghnia, Cavalli et al. 2007). The *dmn*$^{5499}$ allele, kindly provided by Dr. Jason Duncan, is also thought to be a loss of function point mutant (unpublished observations). The *Gl*$^{1}$ allele is thought to be dominant negative. As with kinesin-1, UAS-APPYFP; *pin*$^{88K}$/B3 virgins were crossed to *grid*/TM6B, *dmn*$^{5499}$/CyO, or *Gl*$^{1}$/In(3L)D, *d*$^{1}$ (BL-2394). Selected males UAS-APPYFP/Y; *dynactin*/B3 were then crossed to virgin SG26.1Gal4 animals, and female non-tubby L3 larvae were selected for imaging.

For kinesin-1 overexpression experiments, we used GEN-KLC/CyO; TM3/TM6B and *sp*/CyO; GEN-KHC stocks (Saxton, Hicks et al. 1991; Gindhart, Desai

et al. 1998). To achieve overexpression of both kinesin-1 subunits, we crossed GEN-KLC; GEN-KHC virgins to UAS-APPYFP/Y; SG26.1Gal4/B3 animals and imaged UAS-APPYFP/X; GEN-KLC/+; GEN-KHC/SG26.1 animals. For cytoplasmic dynein overexpression experiments, we used a GEN-DIC stock (Boylan and Hays 2002). In brief, UAS-APPYFP/Y; GEN-DIC/B3 males were generated and crossed to SG26.1 virgins. UAS-APPYFP/X; GEN-DIC/+; SG26.1/+ L3 larvae were then selected for imaging.

**Microscopy**

L3 larvae were dissected and imaged on a 3 $cm^2$ sylgard platform using $Ca^{2+}$-free medium consisting of NaCl (128 mM), EGTA (1 mM), MgCl2 (4 mM), KCl (2 mM), HEPES (5 mM), and sucrose (36 mM). Dissected animals were inverted onto a cover slip and imaged using a Nikon Eclipse TE2000-U inverted microscope with a CoolSNAP HQ camera (Roper Scientific) and a 100×/1.40 NA oil objective. Images were collected at 10 frames per second with 100 ms exposure for 15 seconds under the control of Metamorph software (MDS Analytical Technologies). For each genotype, four time-lapse movies were collected for each animal; ten animals were imaged for analysis.

**Western blot analysis**

To characterize *Dhc64C* gene mutations, balanced females carrying the *□4163a* or *4-19* mutations were crossed to males expressing the DHC-3HA transgene and a deficiency that removes the *Dhc64C* gene. Progeny of genotype *Df/γ* or *Df/4-19* survive only in the presence of the transgene. Protein extracts from all the female progeny classes were either treated with UV-vanadate (+) or left untreated (-) and then assayed by Western blot. The blot was probed with an anti-DHC antibody that recognizes

endogenous DHC, the DHC-3HA transgene product, and the LUV fragments resulting from UV cleavage of the endogenous and transgenic DHC. Tagged and un-tagged LUV fragments are resolved as a doublet. Only a single LUV band is recognized in rescued *Df/γ* or *Df/4-19* flies, corresponding to the higher molecular weight tagged fragment. This is consistent with the absence of endogenous DHC protein expression.

Protein analysis of kinesin-1, cytoplasmic dynein, and dynactin genetic reduction and overexpression backgrounds was done using Western blot and quantification with an Odyssey system (Li-COR Biosciences). In brief, ten animals were homogenized in 100 mL 2X LDS sample buffer (Invitrogen) with 2% BME. Samples were heated for 10 minutes at 98°C and centrifuged for 5 minutes at 14,000 rpm. The supernatant was then removed, and protein concentration was measured using the Bio-Rad DC protein assay. Samples were loaded on pre-cast 4-12% Bis-Tris gels (Invitrogen), and See-Plus 2 (Invitrogen) was used as the molecular weight marker. Transfer to nitrocellulose membranes was done at 4°C using a wet system and buffer consisting of 25 mM Tris-base, 190 mM Glycine, and 20% methanol. Membranes were incubated in primary antibody overnight at 4°C. Incubation in secondary antibody (Odyssey; 1:5,000) was 2 hours at room temperature. Quantification was done using Odyssey software.

**Antibodies**

Anti-KHC (Cytoskeleton, Denver, CO), anti-KLC (Goldstein lab), anti-DHC (P1H4) (McGrail and Hays 1997), anti-DIC (Chemicon International, Temecula, CA), anti-ROBL (Bowman, Patel-King et al. 1999), anti-Arp1 (Haghnia, Cavalli et al. 2007), anti-p50 (Duncan and Warrior 2002), anti-syntaxin (8C3) (Developmental Studies Hybridoma Bank, University of Iowa, Iowa City, IA) were used as described. Many

commercially available anti-p150 antibodies were tested, but none recognized *Drosophila* p150.

**Membrane flotation assay**

After raising yw and $khc^{8}$/+ animals at 25°C, we collected approximately 7.5 mL of adult flies in a 50 mL conical tube and snap-froze immediately in liquid nitrogen. Tubes were shaken to separate heads from bodies, and fly heads were collected using a sieving system (Slemmon, Salvaterra et al. 1982). Heads were then homogenized in 0.75 mL homogenization buffer comprised of 8% sucrose + 1 mM imidazole. Debris was removed by centrifugation at 1,500 x g for 10 minutes at 4°C, and the postnuclear supernatant (PNS) was collected. The pellet was then resuspended in 0.75 mL homogenization buffer and centrifuged for 5 minutes at 1500 x g. The supernatant was collected and combined with the PNS, which was centrifuged at 10,000 x g for 5 minutes to remove mitochondria. The resulting supernatant was carefully removed so as not to disturb the pellet and mixed with 62% sucrose to a final concentration of 40% sucrose ("input"). The input was bottom loaded in an 11x34mm Beckman polycarbonate tube and overlaid with two 0.7 mL cushions of 35% and 8% sucrose. Tubes were spun at 200,000 x g for 2 hours at 4□C. The 8/35% interface, which contains light membrane-bound organelles and associated proteins (Haghnia, Cavalli et al. 2007) was collected and assayed by SDS-PAGE and Western blotting.

**Single particle tracking and computational analysis of APPYFP vesicle movement**

APPYFP vesicles in time-lapse movies were detected as particles (Ponti, Vallotton et al. 2003). Their full trajectories were recovered using customized software based on a modification of the single particle tracking technique described in (Yang,

Matov et al. 2005). Specifically, because individual APPYFP vesicles frequently cross one another during bidirectional transport, their trajectories were first resolved using a global bipartite linear assignment algorithm (Yang, Matov et al. 2005) that minimizes total variations of intensity, velocity, and direction of movement for each vesicle. However, because the output of this step still contains mostly trajectory segments, a further process was performed to link these segments into full trajectories using a multiple hypothesis testing algorithm (Blackman 1999) that grows individual trajectory segments into full trajectories. Then, a manual process was used to recover trajectories that the software was unable to recover. Finally, for quality control, all recovered trajectories were individually inspected so that errors are either corrected or removed. This process is able to recover more than 95% of all vesicle trajectories that fully reside in the microscope field-of-view.

For each genotype, individual cargos are automatically classified as being stationary, anterograde, retrograde, or reversing. Cargo trajectories of each genotype are then analyzed by calculating five different groups of descriptors that characterize the overall distribution of cargo population and individual cargo behavior in terms of velocity, run-length, pause, and reversal. See Appendix for detailed definitions and explanations of these descriptors. Data analysis was conducted using customized software written in MATLAB (Mathworks) and C++.

**Statistics**

Data are first checked for normality using three different tests implemented in the *nortest* package of *R*: the Lilliefors test, the Anderson-Darling test, and the Shapiro-Francis test. For those that follow normal distributions, their means and distributions are

compared using pairwise two-sample two-sided student's t-tests and Kolmogorov-Smirnov tests, respectively. For those that do not follow normal distributions, nonparametric tests including permutation tests (Moore and McCabe 2005) and Wilcoxon tests are used. For example, distributions of segmental velocities follow a mixture of multiple normal distribution modes rather than a single normal distribution. We used permutation tests to assess differences between means. When differences between means of segmental velocities of different genotypes were not statistically significant, we further assessed their differences by comparing their distributions in terms of their medians using Wilcoxon rank-sum tests. See Appendix for further details regarding the statistical tests comparing other non-normally distributed data such as pause frequency, pause duration, and run length.

For each genotype, different modes in cargo velocities were identified by model-based clustering of the collection of all cargo segmental velocities using the mClust package of *R* (Fraley and Raftery 2002). Then, for each individual cargo, the mode of its segmental velocities can be determined using standard pattern classification techniques (Theodoridis, and Koutroumbas, 2008). Specifically, we compared the segmental velocity modes of each individual cargo in three cases: 1) before and after a pause; 2) before and after a reversal; and 3) on initiation and termination of a track segment. By repeating this analysis for all individual cargos, we calculated the ensemble probabilities of transition between modes. That is, for each genotype under the three cases, we calculated ensemble probabilities of cargos remaining in the same segmental velocity mode and switching between different modes. See Appendix for further details.

To examine whether individual cargos stably maintain their velocity modes, we first calculated the theoretical mode transition probabilities if cargos were to randomly adopt different velocity modes relative to previous velocity modes as described above. Using the analysis of control anterograde velocities before and after a pause as an example, clustering analysis reveals that the anterograde segmental velocities have three modes at 0.37μm/sec, 0.66μm/sec, and 1.46μm/sec with corresponding probabilities of a vesicle occupying each mode of 0.2615, 0.3940, and 0.3445, respectively. Thus, the probability for a cargo to stay in the same mode before and after a pause if modes are selected randomly after a pause is (0.2615*0.2615) + (0.3940*0.3940) + (0.3445*0.3445), which equals approximately 0.34. Similarly, the probability of a cargo randomly undergoing a single mode switch, either between mode 1 to 2 or between mode 2 to 3, is (0.2615*0.3940) + (0.3940*0.2615) + (0.3940*0.3445) + (0.3445*0.3940), which equals approximately 0.48. Finally, the probability of a cargo randomly undergoing a two mode switch between mode 1 and 3 is (0.2615*0.3445) + (0.3445*0.2615), which equals approximately 0.18. In comparison, the actual measured probability of a cargo to maintain its mode before and after a pause is 0.59, substantially higher than 0.34, suggesting that cargos stably maintain velocity modes before and after pauses.

Consistent with this observation, the actual probability of a single mode switch and a double mode switch are 0.38 and 0.03, respectively, lower than the theoretically predicted probability of 0.48 and 0.18. To check whether these differences are statistically significant, we determined the standard deviation of the estimated actual probabilities using bootstrapping. Using re-sampling with replacement, we randomly

selected a subset of tracks from the total collection of tracks and calculated the probabilities of mode changes. By repeating this process 2000 times, we calculated the standard deviation of the estimated actual probabilities. We found that for all estimated probabilities for both anterograde and retrograde movement, the standard deviations do not exceed 0.02. Using the $3\sigma$ rule, we conclude that the differences between the actual estimated probabilities versus the theoretical probabilities are statistically significant. In conclusion, the actual probability of a cargo to maintain its velocity mode is significantly higher than what a random mode change can account for, indicating that cargos maintain their velocity modes with relative stability.

Chapter 2, in part, is a reprint of the following manuscript currently in review. Reis, G.F.,* G. Yang*, L. Szpankowski, C. Weaver, S.B. Shah, J.T. Robinson, T.S. Hays, G. Danuser, L.S.B. Goldstein. "Kinesin-1 Driven Axonal Transport of APP Vesicles in Vivo is Weakly Processive and Promoted by Interactions with the Intermediate Chain of Cytoplasmic Dynein." The dissertation author was the secondary investigator and author of this paper.

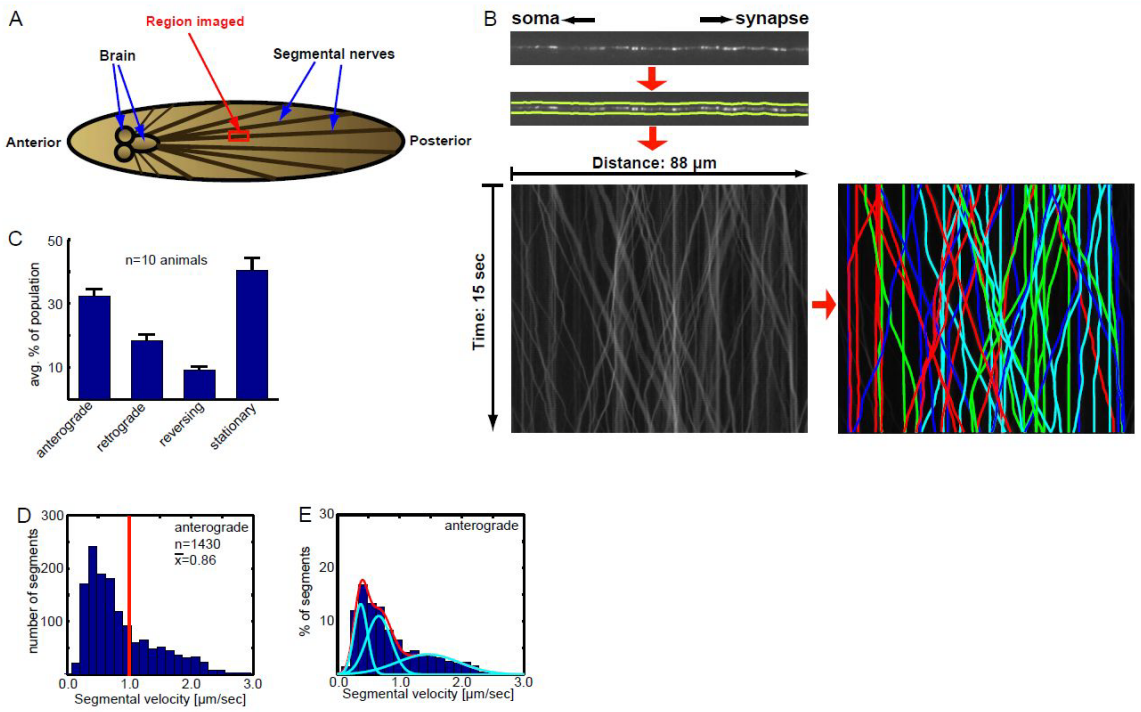


**Figure 2-1** Anterograde transport of APPYFP vesicles in *Drosophila* segmental nerve axons. (A) Live cell image data was collected from an axonal region (~90 micrometers in length) located ~900 micrometers from the cell body. (B) Upper panel: first frame of a time-lapse sequence showing APPYFP vesicle transport. Middle panel: a band (5 pixels in thickness) following the axon is extracted from each frame. Lower left panel: bands from all frames are pasted top-to-bottom to form a kymograph. Lower right panel: computationally recovered vesicle trajectories color-coded and overlaid on the kymograph. Colors were selected randomly to differentiate crossing trajectories. Trajectories lasting shorter than the full movie duration (15 seconds) were excluded. (C) Classification of vesicles as anterograde, retrograde, or reversing when moving or as stationary (n=10 animals; total number of trajectories=1890; all error bars show s.e.m.). (D) Distribution of anterograde segmental velocities. Red line marks 1 µm/sec. (E) The distribution of anterograde segmental velocities has three different modes (cyan) (based on clustering of n = 1430 segmental velocities). Superposition of three modes is shown in red.

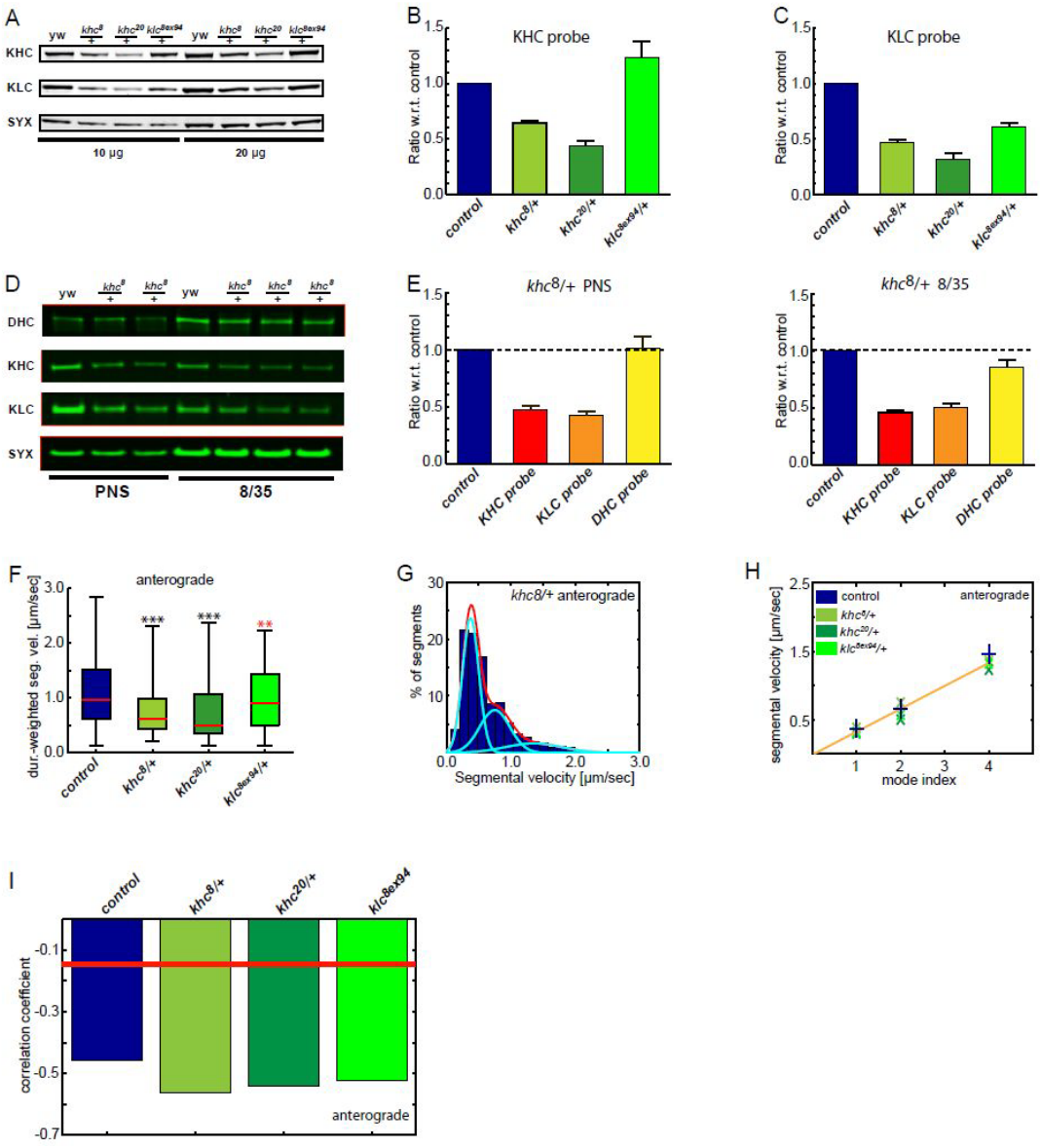


**Figure 2-2** Anterograde transport of APPYFP vesicles in kinesin-1 reduction. (A) Western blot analysis of kinesin-1 in *khc* and *klc* reduction genotypes. Loading control: syntaxin. (B, C) *khc* gene reduction decreases both KHC and KLC protein levels, but *klc* gene reduction only reduces KLC protein level (n=4 per condition). (D) Western blot analysis of membrane-bound KHC, KLC, and DHC proteins in $khc^{8}$/+. (E) Reduction in *khc* leads to decrease in membrane-bound KHC and KLC protein levels without affecting membrane-bound DHC levels. PNS fraction: post-nuclear supernatant; 8/35 fraction: vesicular. (F) Anterograde duration-weighted segmental velocities (control n=780 tracks; $khc^{8}$/+ n=213; $khc^{20}$/+ n=169; $klc^{8ex94}$/+ n=276). (G) Anterograde segmental velocity distribution of $khc^{8}$/+ has three modes (cyan). Red: superposition of modes (based on clustering of n = 449 segmental velocities). (H) Linear regression of anterograde mode centers assembled for different kinesin-1 reduction genotypes. The centers follow approximately a 1:2:4 ratio. (I) Coefficients of correlation between velocity and pause frequency in kinesin-1 reduction genotypes. Low correlation values suggest highly processive behavior; high negative correlation values, as is the case for these data, indicate weakly processive behavior. The red horizontal bar indicates the maximal (3σ) range of correlation coefficients under random pairings of velocity and pause frequency. * $p<0.05$ ** $p<0.01$ *** $p<0.001$

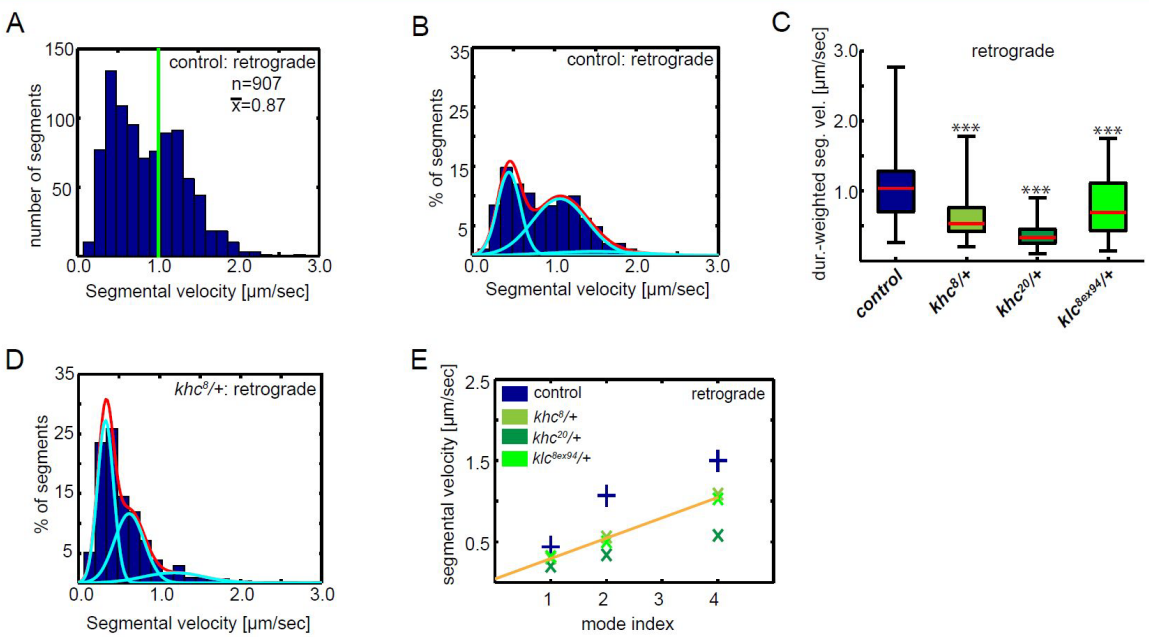


**Figure 2-3** Retrograde transport of APPYFP vesicles in kinesin-1 reduction. (A) Distributions of retrograde segmental velocities. Green line marks 1 µm/sec. (B) Retrograde segmental velocity distribution of control has three modes (cyan). Red: superposition of modes (n = 907 segmental velocities). (C) Retrograde duration-weighted segmental velocities (control n=515 tracks; $khc^{8}$/+ n=122; $khc^{20}$/+ n=143; $klc^{8ex94}$/+ n=134) (D) Retrograde segmental velocity distribution of $khc^{8}$/+ has three modes (cyan). Red: superposition of modes (n= 310 segmental velocities). (E) Linear regression of retrograde mode centers assembled from different kinesin-1 reduction genotypes. The centers follow approximately a ratio of 1:2:4. * p<0.05 ** p<0.01 *** p<0.001

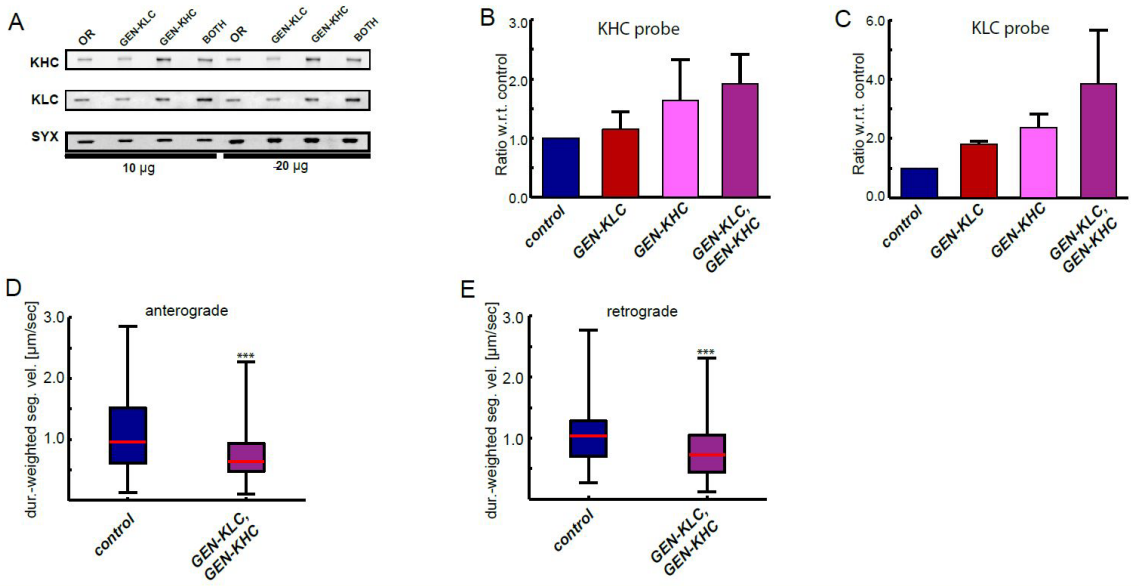


**Figure 2-4** (A-E). APPYFP vesicle transport in kinesin-1 overexpression. (A-C) Western blot analysis of kinesin-1 proteins in *khc* and *klc* overexpression genotypes (GEN-KHC and GEN-KLC). The overexpression of *khc* increases both KHC and KLC protein levels, but *klc* overexpression only increases KLC protein level (n=4 for each condition). (D-E) Effects of kinesin-1 overexpression on anterograde and retrograde duration-weighted segmental velocities (anterograde: control n=780 tracks; GEN-KLC; GEN-KHC n=875; retrograde: control n=515 tracks; GENKLC; GEN-KHC n=411). * $p<0.05$ ** $p<0.01$ *** $p<0.001$

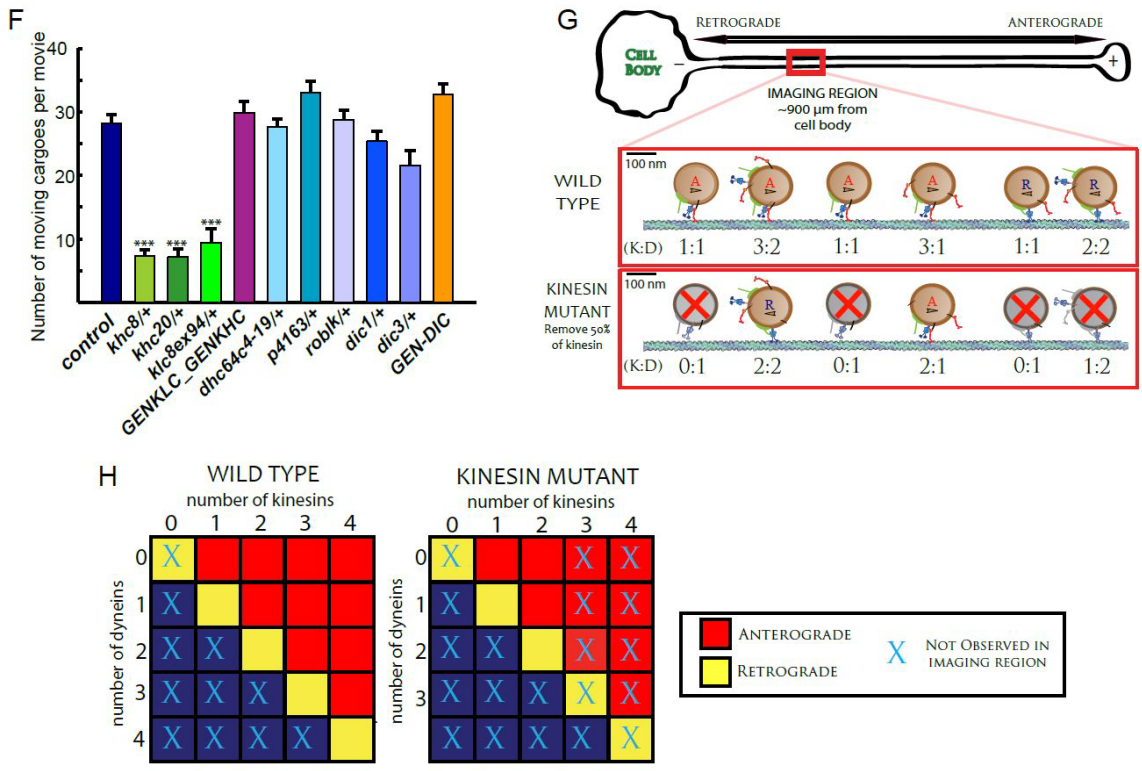


**Figure 2-4** (F-H). (F) Total number of moving cargos per movie for each genotype. A marked decrease in moving cargos is observed for kinesin-1 reductions. All error bars show s.e.m. (G) Kinesin-1 reductions lead to impairment of both anterograde and retrograde transport (imaged region highlighted in red). A hypothetical distribution of moving vesicles is displayed for control. Vesicles on which the number of active kinesin-1 and dynein motors are equal, or on which kinesin-1 motors outnumber dynein motors, are far more likely to enter the axon from the cell body and to reach the imaged region than vesicles with a surplus of dynein motors (K:D – ratio of kinesin and dynein motors). With kinesin reduction, vesicles on which dynein motors outnumber kinesin will leave the imaged region (crossed-out in the schematic below). Hence, vesicles reaching the imaged region will have fewer dynein motors compared to control, resulting in an apparent defect in retrograde traffic. (H) Matrix representation emphasizing bidirectional impairment of APP transport with kinesin reduction. The model described in (G) predicts that a majority of vesicles found in a given region distal from the cell body would have a ratio of kinesin:dynein (K:D) > 1. These vesicles would move preferentially anterogradely and thus would pass through the imaged region. Depending on the details of the coordination of the two antagonistic motors, vesicles with a K:D ratio of ~1 may eventually also reach the imaged region. However, vesicles with a K:D ratio <1 would be less likely to be seen in the imaged region. In support of this assumption, we found 40% stationary, 32% anterograde, 18% retrograde, and 9% reversing vesicles of the total vesicle population observed in APPYFP control. Under this view, a reduction in kinesin-1 lowers the overall number of vesicles reaching the imaged region. In addition, those vesicles that reach the imaged region will tend to have fewer dynein motors bound, which yields a lower efficiency of retrograde transport. This proposed sampling phenomenon can be formalized by a matrix of motor combinations per vesicle. Only combinations in the upper triangle (K:D > 1) and on the diagonal (K:D ~ 1) would be captured by our imaging approach whereas the lower triangle (K:D < 1) would escape observation. In the kinesin-1 reduction genotypes, cytoplasmic dynein levels are implicitly reduced in the imaged region. In all cases, an X designates vesicles that are not observed in the imaged region. * $p<0.05$ ** $p<0.01$ *** $p<0.001$

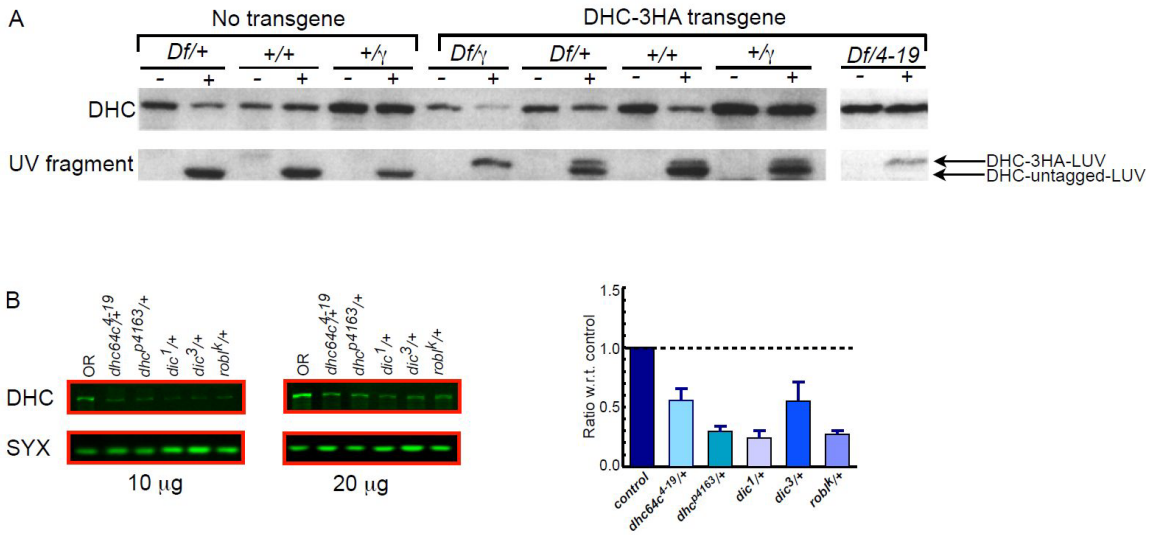


**Figure 2-5** (A-B)**.** APPYFP vesicle transport in cytoplasmic dynein and dynactin reductions. (A) Protein extracts were treated with UV-vanadate (+), or left untreated (-), and assayed by Western blot (see Methods). The blot was probed with an anti-DHC antibody that recognizes endogenous DHC, the DHC-3HA transgene product, and the LUV fragments resulting from UV cleavage of the endogenous and transgenic DHC. Tagged and un-tagged LUV fragments are resolved as a doublet. Only a single LUV band, corresponding to the larger, tagged fragment, is recognized in rescued *Df/g* flies, consistent with the absence of endogenous DHC protein expression. Similar results are seen with the DHC allele 4-19 (far right). (B) Western blot analysis of membrane-bound DHC levels in different cytoplasmic dynein reduction genotypes.

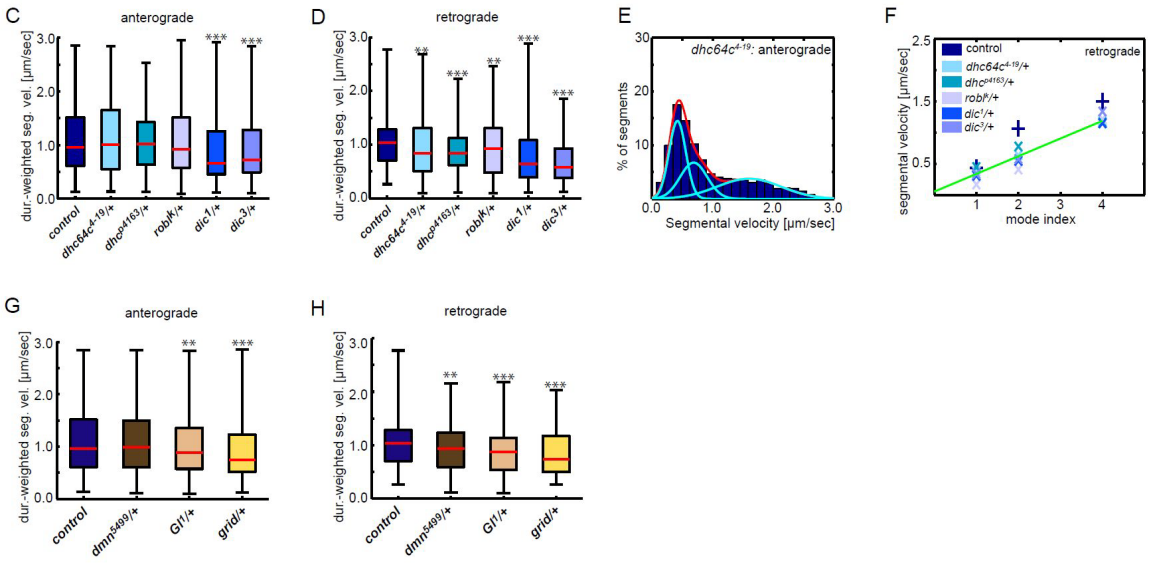


**Figure 2-5** (C-H). APPYFP vesicle transport in cytoplasmic dynein and dynactin reductions. (C-D) Effects of cytoplasmic dynein reduction on anterograde and retrograde duration-weighted segmental velocities (anterograde: control n=780 tracks; *dhc64c*$^{4-19}$/+ n=764; *dhc*$^{p4163}$/+ n=1024; *robl*$^{k}$/+ n=848; *dic*$^{1}$/+ n=743; *dic*$^{3}$/+ n=514; retrograde: control n=515 tracks; *dhc64c*$^{4-19}$/+ n=420; *dhc*$^{p4163}$/+ n=443; *robl*$^{k}$/+ n=397; *dic*$^{1}$/+ n=366; *dic*$^{3}$/+ n=418) (E) Anterograde segmental velocity distribution of *dhc64c*$^{4-19}$/+ has three modes (cyan). Red: superposition of modes (n= 1309 segmental velocities) (F) Linear regression of retrograde mode centers assembled from different dynein reduction genotypes. The centers follow approximately a ratio of 1:2:4. (G-H) Effects of dynactin reduction on (A-B) anterograde and retrograde duration-weighted segmental velocities (anterograde: control n=780 tracks; *dmn*$^{5499}$/+ n=1207; *Gl*$^{1}$/+ n=617; *grid*/+ n=624; retrograde: control n=515 tracks; *dmn*$^{5499}$/+ n=464; *Gl*$^{1}$/+ n=304; *grid*/+ n=284). * p<0.05 ** p<0.01 *** p<0.001

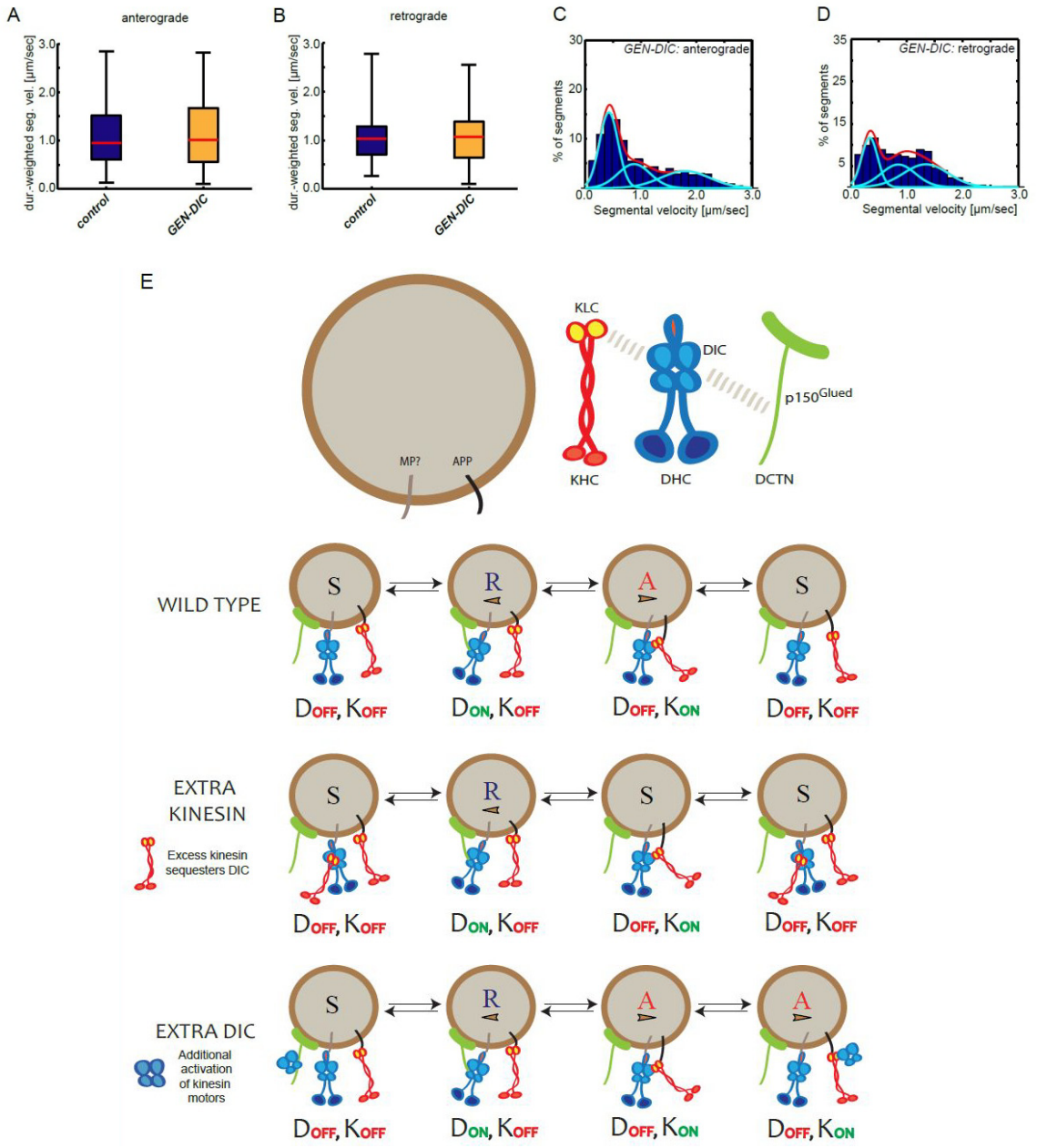


**Fig 2-6** APPYFP vesicle transport in DIC overexpression. (A-B) Effects of DIC overexpression on anterograde and retrograde duration-weighted segmental velocities (anterograde: control n=780 tracks; GEN-DIC n=936; retrograde: control n=515 tracks; GEN-DIC n=463) (C-D) Anterograde and retrograde segmental velocity distributions of GEN-DIC each have three modes. (anterograde n = 1541 segmental velocities; retrograde n = 758 segmental velocities) (E) Schematic of a proposed model for axonal transport of APP vesicles for control, overexpressed kinesin-1, and overexpressed DIC genetic backgrounds. A, R, and S labels designate transport behavior of a vesicle as anterograde, retrograde, and stationary respectively.

**Table 2-1** Summary of parameter values for all genotypes studied.

| | +/+ | *khc*$^{8}$/+ | *khc*$^{20}$/+ | *klc*$^{8ex94}$/+ | *GEN-KLC; GEN-KHC* | *dhc*$^{4-19}$/+ | *dhc*$^{p4163}$/+ |
|---|---|---|---|---|---|---|---|
| **Total number of vesicles** | 1890 | 1270 | 1263 | 1486 | 1929 | 1788 | 2046 |
| **Stationary vesicles** | 761 | 979 | 977 | 1111 | 734 | 682 | 671 |
| **Anterograde vesicles** | 613 | 174 | 142 | 240 | 784 | 684 | 930 |
| **Retrograde vesicles** | 342 | 77 | 117 | 96 | 319 | 340 | 349 |
| **Switching vesicles** | 174 | 40 | 27 | 39 | 92 | 82 | 96 |
| **Anterograde duration-weighted segmental velocity (mean±s.d.; μm/sec)** | 1.09±0.58 | 0.77±0.44 | 0.71±0.48 | 0.96±0.52 | 0.78±0.46 | 1.14±0.66 | 1.06±0.52 |
| **Tracks** | N = 780 | N = 213 | N = 169 | N = 276 | N = 875 | N = 764 | N = 1024 |
| | | | | | | | |
| **Retrograde duration-weighted segmental velocity (mean±s.d.; μm/sec)** | 1.02±0.41 | 0.65±0.36 | 0.37±0.19 | 0.76±0.39 | 0.78±0.40 | 0.93±0.50 | 0.89±0.38 |
| **Tracks** | N = 515 | N = 122 | N=143 | N = 134 | N = 411 | N = 420 | N = 443 |
| | | | | | | | |
| **Anterograde unweighted segmental velocity (mean±s.d.; μm/sec)** | 0.86±0.55 | 0.63±0.40 | 0.59±0.42 | 0.77±0.51 | 0.67±0.41 | 0.92±0.63 | 0.91±0.52 |
| **Segments** | N = 1430 | N = 449 | N = 315 | N = 500 | N = 1644 | N = 1309 | N = 1585 |
| | | | | | | | |
| **Retrograde unweighted segmental velocity (mean±s.d.; μm/sec)** | 0.87±0.45 | 0.55±0.33 | 0.35±0.18 | 0.62±0.37 | 0.64±0.38 | 0.77±0.49 | 0.80±0.40 |
| **Segments** | N = 907 | N = 310 | N = 321 | N = 260 | N = 890 | N = 800 | N = 735 |
| **Anterograde segmental pause frequency (mean±s.e.m.; sec$^{-1}$)** | 1.45±0.09 | 2.22±0.18 | 2.33±0.23 | 2.08±0.18 | 1.70±0.09 | 2.01±0.12 | 2.18±0.12 |
| **Pauses** | N = 767 | N = 339 | N = 227 | N = 325 | N = 994 | N = 745 | N = 784 |
| | | | | | | | |
| **Retrograde segmental pause frequency (mean±s.e.m.; sec$^{-1}$)** | 1.48±0.12 | 2.11±0.20 | 2.34±0.20 | 2.70±0.26 | 1.75±0.11 | 1.39±0.11 | 1.92±0.16 |
| **Pauses** | N = 434 | N = 253 | N = 269 | N = 189 | N = 586 | N = 477 | N = 387 |
| | | | | | | | |
| **Anterograde total pause frequency (mean±s.e.m.; events/sec)** | 0.11±0.01 | 0.22±0.02 | 0.19±0.02 | 0.21±0.04 | 0.14±0.01 | 0.12±0.01 | 0.10±0.01 |
| **Tracks** | N = 695 | N = 201 | N = 164 | N = 264 | N = 837 | N = 725 | N = 977 |

**Table 2-1** continued... Summary of parameter values for all genotypes studied

| | +/+ | *khc*$^{8}$/+ | *khc*$^{20}$/+ | *klc*$^{8ex94}$/+ | *GEN-KLC; GEN-KHC* | *dhc*$^{4-19}$/+ | *dhc*$^{p4163}$/+ |
|---|---|---|---|---|---|---|---|
| **Retrograde total pause frequency (mean±s.e.m.; events/sec)** | 0.09±0.01 | 0.34±0.03 | 0.46±0.08 | 0.27±0.03 | 0.17±0.01 | 0.16±0.03 | 0.12±0.03 |
| **Tracks** | N = 439 | N = 110 | N = 134 | N = 123 | N = 371 | N = 371 | N = 404 |
| **Anterograde pause duration (mean±s.e.m.; sec)** | 1.55±0.05 | 2.35±0.12 | 2.72±0.16 | 2.59±0.14 | 1.91±0.06 | 2.18±0.09 | 2.38±0.09 |
| **Pauses** | N = 767 | N = 339 | N = 227 | N = 325 | N = 994 | N = 745 | N = 784 |
| **Retrograde pause duration (mean±s.e.m.; sec)** | 1.46±0.06 | 2.33±0.14 | 2.96±0.17 | 2.74±0.18 | 1.76±0.06 | 1.75±0.08 | 1.89±0.11 |
| **Pauses** | N = 434 | N = 253 | N = 269 | N = 189 | N = 586 | N = 477 | N = 387 |
| **Anterograde run length (mean±s.e.m.; µm)** | 7.63±0.26 | 4.07±0.30 | 4.44±0.38 | 6.57±0.38 | 5.31±0.17 | 8.78±0.30 | 9.18±0.24 |
| **Segments** | N = 1430 | N = 449 | N = 315 | N = 500 | N = 1644 | N = 1309 | N = 1585 |
| **Retrograde run length (mean±s.e.m.; µm)** | 7.07±0.25 | 2.36±0.23 | 1.27±0.09 | 4.21±0.39 | 4.27±0.20 | 6.07±0.27 | 6.61±0.25 |
| **Segments** | N = 907 | N = 310 | N = 321 | N = 260 | N = 890 | N = 800 | N = 735 |
| **Total time anterograde movement (not including switchers) (mean±s.e.m.; sec)** | 13.35±0.10 | 10.93±0.29 | 11.21±0.33 | 11.84±0.26 | 12.72±0.11 | 12.78±0.13 | 13.11±0.10 |
| **Tracks** | N = 613 | N = 174 | N = 142 | N = 240 | N = 784 | N = 684 | N = 930 |
| **Total time retrograde movement (not including switchers) (mean±s.e.m.; sec)** | 13.73±0.11 | 8.83±0.43 | 8.60±0.39 | 10.31±0.50 | 12.15±0.17 | 12.77±0.16 | 13.25±0.15 |
| **Tracks** | N = 342 | N = 77 | N = 117 | N = 96 | N = 319 | N = 340 | N = 349 |
| **Total time anterograde movement (including switchers) (mean±s.e.m.; sec)** | 11.78±0.14 | 9.72±0.31 | 10.38±0.33 | 11.03±0.26 | 12.00±0.12 | 12.13±0.14 | 12.53±0.11 |
| **Tracks** | N = 780 | N = 213 | N = 169 | N = 276 | N = 875 | N = 764 | N = 1024 |

**Table 2-1** continued... Summary of parameter values for all genotypes studied

| | +/+ | *khc*$^{8}$/+ | *khc*$^{20}$/+ | *klc*$^{8ex94}$/+ | *GEN-KLC; GEN-KHC* | *dhc*$^{4-19}$/+ | *dhc*$^{p4163}$/+ |
|---|---|---|---|---|---|---|---|
| **Total time retrograde movement (including switchers) (mean±s.e.m.; sec)** | 11.53±0.18 | 8.12±0.34 | 7.81±0.35 | 9.07±0.43 | 10.95±0.19 | 11.58±0.19 | 11.70±0.20 |
| **Tracks** | N = 515 | N = 122 | N=143 | N = 134 | N = 411 | N = 420 | N = 443 |
| **Anterograde velocity mode 1 (velocity of vesicles in mode)*** | 0.37±0.11 | 0.38±0.13 | 0.30±0.10 | 0.32±0.11 | 0.42±0.14 | 0.42±0.14 | 0.44±0.16 |
| **(percentage of vesicles in mode)*** | 26.15% | 54.69% | 39.61% | 31.77% | 49.16% | 36.48% | 35.83% |
| **Anterograde velocity mode 2 (velocity of vesicles in mode)*** | 0.66±0.20 | 0.75±0.23 | 0.50±0.15 | 0.57±0.11 | 0.70±0.22 | 0.69±0.22 | 0.86±0.28 |
| **(percentage of vesicles in mode)*** | 39.40% | 31.97% | 37.31% | 30.08% | 36.37% | 27.36% | 27.92% |
| **Anterograde velocity mode 3 (velocity of vesicles in mode)*** | 1.46±0.50 | 1.36±0.44 | 1.23±0.39 | 1.32±0.40 | 1.40±0.49 | 1.60±0.53 | 1.41±0.45 |
| **(percentage of vesicles in mode)*** | 34.45% | 13.34% | 23.08% | 38.15% | 14.47% | 36.16% | 36.25% |
| **Retrograde velocity three-mode fitting: mode 1 (velocity of vesicles in mode)*†** | 0.44±0.14 | 0.30±0.09 | 0.20±0.05 | 0.32±0.10 | 0.33±0.10 | 0.38±0.12 | 0.45±0.16 |
| **mode 1 (percentage of vesicles in mode)*†** | 35.60% | 60.60% | 28.97% | 35.35% | 33.14% | 42.24% | 33.39% |
| **Retrograde velocity three-mode fitting: mode 2 (velocity of vesicles in mode)*†** | 1.07±0.33 | 0.56±0.18 | 0.34±0.09 | 0.50±0.12 | 0.50±0.13 | 0.64±0.08 | 0.78±0.23 |
| **mode 2 (percentage of vesicles in mode)*†** | 57.87% | 31.60% | 48.60% | 30.23% | 27.37% | 15.68% | 33.64% |
| **Retrograde velocity three-mode fitting: mode 3 (velocity of vesicles in mode)*†** | 1.50±0.54 | 1.09±0.39 | 0.58±0.21 | 1.03±0.31 | 0.99±0.36 | 1.20±0.44 | 1.17±0.36 |
| **mode 3 (percentage of vesicles in mode)*†** | 6.53% | 7.80% | 22.43% | 34.43% | 39.49% | 42.08% | 32.98% |
| **Retrograde velocity two-mode fitting: mode 1 (velocity of vesicles in mode)*†** | 0.44±0.14 | 0.39±0.14 | 0.28±0.09 | 0.39±0.14 | 0.40±0.13 | 0.45±0.17 | 0.52±0.20 |
| **mode 1 (percentage of vesicles in mode)*†** | 32.76% | 66.23% | 72.90% | 62.28% | 57.57% | 57.98% | 47.29% |

**Table 2-1** continued... Summary of parameter values for all genotypes studied

| | +/+ | *khc*$^{8}$/+ | *khc*$^{20}$/+ | *klc*$^{8ex94}$/+ | *GEN-KLC; GEN-KHC* | *dhc*$^{4-19}$/+ | *dhc*$^{p4163}$/+ |
|---|---|---|---|---|---|---|---|
| **Retrograde velocity two-mode fitting: mode 2 (velocity of vesicles in mode)*†** | 1.08±0.40 | 0.85±0.37 | 0.55±0.21 | 0.99±0.32 | 0.96±0.37 | 1.20±0.44 | 1.04±0.37 |
| **mode 2 (percentage of vesicles in mode)*†** | 67.24% | 33.77% | 27.09% | 37.72% | 42.43% | 42.02% | 52.71% |

**Table 2-1** continued... Summary of parameter values for all genotypes studied.

| | *robl$^{k}$*/+ | *dic$^{1}$*/+ | *dic$^{3}$*/+ | *GEN-DIC* | *dmn$^{5499}$*/+ | *Gl$^{1}$*/+ | *grid*/+ | *dic$^{3}$*/+; *grid*/+ |
|---|---|---|---|---|---|---|---|---|
| **Total number of vesicles** | 1690 | 1950 | 1785 | 1804 | 2297 | 1463 | 1372 | 1835 |
| **Stationary vesicles** | 537 | 935 | 920 | 492 | 775 | 626 | 546 | 565 |
| **Anterograde vesicles** | 752 | 646 | 446 | 847 | 1057 | 531 | 541 | 874 |
| **Retrograde vesicles** | 302 | 270 | 346 | 375 | 313 | 220 | 200 | 317 |
| **Switching vesicles** | 99 | 99 | 73 | 90 | 152 | 86 | 85 | 79 |
| **Anterograde duration-weighted segmental velocity (mean±s.d.; μm/sec)** | 1.07±0.62 | 0.91±0.60 | 0.92±0.55 | 1.14±0.67 | 1.07±0.56 | 1.00±0.53 | 0.91±0.50 | 0.83±0.42 |
| **Tracks** | N = 848 | N = 743 | N = 514 | N = 936 | N = 1207 | N = 617 | N = 624 | N = 953 |
| | | | | | | | | |
| **Retrograde duration-weighted segmental velocity (mean±s.d.; μm/sec)** | 0.93±0.53 | 0.78±0.48 | 0.68±0.37 | 1.03±0.52 | 0.93±0.44 | 0.88±0.42 | 0.85±0.44 | 0.72±0.36 |
| **Tracks** | N = 397 | N = 366 | N = 418 | N = 463 | N = 464 | N = 304 | N = 284 | N = 396 |
| | | | | | | | | |
| **Anterograde unweighted segmental velocity (mean±s.d.; μm/sec)** | 0.87±0.60 | 0.71±0.53 | 0.71±0.50 | 0.92±0.65 | 0.85±0.58 | 0.80±0.52 | 0.70±0.44 | 0.71±0.41 |
| **Segments** | N = 1408 | N = 1539 | N = 1111 | N = 1541 | N = 2061 | N = 1117 | N = 1371 | N = 1510 |
| | | | | | | | | |
| **Retrograde unweighted segmental velocity (mean±s.d.; μm/sec)** | 0.78±0.52 | 0.65±0.44 | 0.57±0.34 | 0.89±0.52 | 0.80±0.48 | 0.74±0.42 | 0.67±0.39 | 0.64±0.35 |
| **Segments** | N = 682 | N = 793 | N = 1035 | N = 758 | N = 793 | N = 580 | N = 634 | N = 736 |
| **Anterograde segmental pause frequency (mean±s.e.m.; sec$^{-1}$)** | 1.93±0.12 | 1.81±0.09 | 1.68±0.10 | 1.93±0.11 | 2.00±0.09 | 1.70±0.11 | 1.29±0.07 | 2.04±0.12 |
| **Pauses** | N = 734 | N = 1031 | N = 762 | N = 817 | N = 1197 | N = 652 | N = 876 | N = 766 |

**Table 2-1** continued... Summary of parameter values for all genotypes studied.

| | *robl*$^{k}$/+ | *dic*$^{1}$/+ | *dic*$^{3}$/+ | *GEN-DIC* | *dmn*$^{5499}$/+ | *Gl*$^{1}$/+ | *grid*/+ | *dic*$^{3}$/+; *grid*/+ |
|---|---|---|---|---|---|---|---|---|
| **Retrograde segmental pause frequency (mean±s.e.m.; sec$^{-1}$)** | 1.65±0.15 | 1.78±0.12 | 1.68±0.10 | 1.94±0.16 | 2.38±0.17 | 1.72±0.16 | 1.41±0.11 | 1.50±0.13 |
| **Pauses** | N = 368 | N = 554 | N = 764 | N = 381 | N = 455 | N = 334 | N = 398 | N = 444 |
| | | | | | | | | |
| **Anterograde total pause frequency (mean±s.e.m.; events/sec)** | 0.09±0.01 | 0.17±0.02 | 0.21±0.02 | 0.10±0.01 | 0.12±0.01 | 0.12±0.01 | 0.15±0.01 | 0.09±0.01 |
| **Tracks** | N = 807 | N = 701 | N = 486 | N = 891 | N = 1149 | N = 580 | N = 581 | N = 923 |
| | | | | | | | | |
| **Retrograde total pause frequency (mean±s.e.m.; events/sec)** | 0.21±0.05 | 0.19±0.01 | 0.24±0.03 | 0.14±0.01 | 0.12±0.01 | 0.13±0.01 | 0.16±0.01 | 0.13±0.01 |
| **Tracks** | N = 368 | N = 332 | N = 394 | N = 425 | N = 411 | N = 269 | N = 246 | N = 366 |
| | | | | | | | | |
| **Anterograde pause duration (mean±s.e.m.; sec)** | 2.03±0.07 | 1.86±0.05 | 1.87±0.06 | 2.10±0.07 | 2.29±0.06 | 1.95±0.07 | 1.37±0.03 | 2.19±0.08 |
| **Pauses** | N = 734 | N = 1031 | N = 762 | N = 817 | N = 1197 | N = 652 | N = 876 | N = 766 |
| | | | | | | | | |
| **Retrograde pause duration (mean±s.e.m.; sec)** | 1.90±0.11 | 1.81±0.07 | 1.71±0.06 | 2.03±0.11 | 2.05±0.08 | 1.82±0.09 | 1.39±0.05 | 1.96±0.09 |
| **Pauses** | N = 368 | N = 554 | N = 764 | N = 381 | N = 455 | N = 334 | N = 398 | N = 444 |
| | | | | | | | | |
| **Anterograde run length (mean±s.e.m.; μm)** | 8.64±0.27 | 5.49±0.21 | 5.31±0.24 | 9.34±0.28 | 8.10±0.21 | 7.09±0.26 | 5.35±0.21 | 6.94±0.19 |
| **Segments** | N = 1408 | N = 1539 | N = 1111 | N = 1541 | N = 2061 | N = 1117 | N = 1371 | N = 1510 |
| | | | | | | | | |
| **Retrograde run length (mean±s.e.m.; μm)** | 6.85±0.32 | 4.25±0.22 | 3.25±0.15 | 8.15±0.32 | 6.44±0.26 | 5.56±0.28 | 4.46±0.26 | 4.75±0.21 |
| **Segments** | N = 682 | N = 793 | N = 1035 | N = 758 | N = 793 | N = 580 | N = 634 | N = 736 |
| | | | | | | | | |
| **Total time anterograde movement (not including switchers) (mean±s.e.m.; sec)** | 13.17±0.10 | 12.19±0.12 | 12.00±0.16 | 13.09±0.10 | 12.65±0.10 | 12.84±0.13 | 12.94±0.11 | 13.22±0.10 |
| **Tracks** | N = 752 | N = 646 | N = 446 | N = 847 | N = 1057 | N = 531 | N = 541 | N = 874 |

**Table 2-1** continued... Summary of parameter values for all genotypes studied.

| | *robl*$^{k}$/+ | *dic*$^{1}$/+ | *dic*$^{3}$/+ | *GEN-DIC* | *dmn*$^{5499}$/+ | *Gl*$^{1}$/+ | *grid*/+ | *dic*$^{3}$/+; *grid*/+ |
|---|---|---|---|---|---|---|---|---|
| **Total time retrograde movement (not including switchers) (mean±s.e.m)** | 13.23±0.18 | 12.04±0.19 | 11.56±0.17 | 13.29±0.15 | 12.85±0.17 | 12.83±0.19 | 12.78±0.19 | 12.60±0.17 |
| **Tracks** | N = 302 | N = 270 | N = 346 | N = 375 | N = 313 | N = 220 | N = 200 | N = 317 |
| **Total time anterograde movement (including switchers) (mean±s.e.m.; sec)** | 12.35±0.13 | 11.30±0.14 | 11.08±0.18 | 12.37±0.12 | 11.79±0.11 | 11.84±0.15 | 12.07±0.14 | 12.57±0.12 |
| **Tracks** | N = 848 | N = 743 | N = 514 | N = 936 | N = 1207 | N = 617 | N = 624 | N = 953 |
| | | | | | | | | |
| **Total time retrograde movement (including switchers) (mean±s.e.m.; sec)** | 11.59±0.21 | 10.66±0.21 | 10.84±0.18 | 12.10±0.18 | 10.65±0.21 | 11.10±0.24 | 10.99±0.24 | 11.45±0.19 |
| **Tracks** | N = 397 | N = 366 | N = 418 | N = 463 | N = 464 | N = 304 | N = 284 | N = 396 |
| **Anterograde velocity mode 1 (velocity of vesicles in mode)*** | 0.34±0.13 | 0.42±0.15 | 0.34±0.11 | 0.43±0.17 | 0.24±0.08 | 0.36±0.12 | 0.40±0.10 | 0.40±0.14 |
| **(percentage of vesicles in mode)*** | 27.93% | 63.74% | 34.00% | 46.67% | 18.99% | 31.84% | 38.59% | 41.33% |
| | | | | | | | | |
| **Anterograde velocity mode 2 (velocity of vesicles in mode)*** | 0.66±0.21 | 0.82±0.26 | 0.58±0.11 | 0.88±0.29 | 0.57±0.20 | 0.65±0.19 | 0.61±0.17 | 0.80±0.27 |
| **(percentage of vesicles in mode)*** | 36.03% | 20.05% | 38.10% | 25.81% | 36.92% | 33.07% | 35.07% | 44.46% |
| | | | | | | | | |
| **Anterograde velocity mode 3 (velocity of vesicles in mode)*** | 1.49±0.55 | 1.72±0.43 | 1.34±0.50 | 1.80±0.44 | 1.35±0.49 | 1.34±0.46 | 1.26±0.47 | 1.33±0.43 |
| **(percentage of vesicles in mode)*** | 36.04% | 16.21% | 27.90% | 27.71% | 44.09% | 35.09% | 26.34% | 14.21% |

**Table 2-1** continued... Summary of parameter values for all genotypes studied.

| | *robl$^{k}$*/+ | *dic$^{1}$*/+ | *dic$^{3}$*/+ | *GEN-DIC* | *dmn$^{5499}$*/+ | *Gl$^{1}$*/+ | *grid*/+ | *dic$^{3}$*/+; *grid*/+ |
|---|---|---|---|---|---|---|---|---|
| **Retrograde velocity three-mode fitting: mode 1 (velocity of vesicles in mode)*†** | 0.17±0.05 | 0.31±0.10 | 0.30±0.09 | 0.33±0.14 | 0.24±0.08 | 0.39±0.13 | 0.32±0.07 | 0.38±0.14 |
| **mode 1 (percentage of vesicles in mode)*†** | 9.23% | 35.25% | 34.14% | 30.61% | 20.97% | 40.94% | 23.59% | 45.44% |
| | | | | | | | | |
| **Retrograde velocity three-mode fitting: mode 2 (velocity of vesicles in mode)*†** | 0.41±0.14 | 0.55±0.18 | 0.51±0.15 | 0.85±0.31 | 0.59±0.21 | 0.82±0.25 | 0.53±0.13 | 0.77±0.25 |
| **mode 2 (percentage of vesicles in mode)*†** | 35.47% | 34.52% | 40.17% | 29.82% | 28.11% | 36.41% | 42.97% | 40.78% |
| | | | | | | | | |
| **Retrograde velocity three-mode fitting: mode 3 (velocity of vesicles in mode)*†** | 1.22±0.45 | 1.15±0.43 | 1.00±0.34 | 1.34±0.40 | 1.15±0.39 | 1.27±0.37 | 1.09±0.39 | 1.13±0.37 |
| **mode 3 (percentage of vesicles in mode)*†** | 55.30% | 30.23% | 25.69% | 39.49% | 50.92% | 22.65% | 33.43% | 13.78% |
| | | | | | | | | |
| **Retrograde velocity two-mode fitting: mode 1 (velocity of vesicles in mode)*†** | 0.35±0.16 | 0.39±0.15 | 0.40±0.15 | 0.35±0.15 | 0.27±0.10 | 0.41±0.14 | 0.45±0.14 | 0.40±0.15 |
| **mode 1 (percentage of vesicles in mode)*†** | 43.30% | 58.60% | 66.96% | 31.88% | 24.89% | 41.43% | 64.04% | 47.96% |
| | | | | | | | | |
| **Retrograde velocity two-mode fitting: mode 2 (velocity of vesicles in mode)*†** | 1.11±0.45 | 1.01±0.44 | 0.92±0.36 | 1.14±0.44 | 0.98±0.43 | 0.98±0.39 | 1.06±0.39 | 0.86±0.34 |
| **mode 2 (percentage of vesicles in mode)*†** | 56.70% | 41.40% | 33.04% | 68.12% | 75.11% | 58.57% | 35.96% | 52.04% |

**Table 2-1** continued... Summary of parameter values for all genotypes studied

*: All velocity modes are in µm/sec

†: For retrograde segmental velocities in each genetic background, best-fitting modes (under the Bayesian Information Criterion) are highlighted in color

# 3 ELUCIDATING THE RELATIVE MOTOR SUBUNIT COMPOSITION OF APP VESICLES

**Abstract**

Intracellular transport along microtubules is powered by molecular motors of the kinesin and cytoplasmic dynein families. Both motors are frequently attached to the same cargo, but engage with the microtubule alternatively, resulting in constant back-and-forth motion ensuring proper distribution of intracellular materials. Although a great deal of information has been revealed regarding how these two opposite-polarity motors coordinate to achieve bi-directional motion for a variety of cargo, assessing motor subunit architectures on individual vesicles has been elusive. We present a robust quantitative immunofluorescence method to elucidate relative motor subunit composition of individual endogenous amyloid precursor protein (APP) vesicles in mouse hippocampal culture. Our data provides new insight on how select motor subunit and cargo attachment protein levels contribute to the overall architecture of these vesicles. We report that APP seems to recruit the light chain of kinesin-1 (KLC1) and the heavy chain of cytoplasmic dynein (DHC1) to the vesicle surface. Furthermore, we propose that KLC1 is in fact necessary for proper loading of DHC1 onto APP vesicles and may explain the retrograde defects observed in impaired kinesin-1 systems.

## 3.1 Introduction

Microtubule-based transport of vesicles and organelles to appropriate destinations in the cell is coordinated by kinesin (anterograde) and dynein (retrograde) motor complexes which are essential for neuronal survival and function. Recent work has demonstrated that kinesin and dynein motor proteins play critical roles in long-distance signaling events in neurons, neuronal regeneration, and in the development of neurodegenerative disease (Goldstein 2003). Mutations in genes that code for various subunits of the molecular machinery have been strongly implicated in several human neurodegenerative diseases including Alzheimer's, Parkinson's, and amyotrophic lateral sclerosis (ALS) (De Vos, Grierson et al. 2008). Elucidating the underlying fundamentals of this highly coordinated system is an essential part of understanding what happens during the progression of these devastating illnesses.

We have recently obtained a great deal of information on the overall transport for a particular type of neuronal cargo, the APP vesicle. Although much progress has been made, we are limited in our understanding of coordination mechanisms at the level of individual vesicles. In this chapter we provide a framework for high-throughput colocalization of diffraction limited fluorescent puncta in 2D immunofluorescence images and apply it to the analysis of endogenous motor content on APP vesicles. The apparent redundancy of motor subunits in mammalian systems allows us to completely remove select pieces of the motor machinery and investigate their role in determining motor architecture on individual vesicles. Several new features of coordination between opposite polarity motor subunits have been revealed and bring us a step closer to refining a general model of microtubule-based transport in neurons.

## 3.2 Methods

### 3.2.1 Data acquisition

**Selection of appropriate model system**

A wide range of relevant motor subunit antibodies were tested to detect relative subunit concentration on APP vesicles. Preliminary efforts to explore this question were attempted in dissected L3 *Drosophila* larvae (see Chapter 2 Methods). The immunofluorescence (IF) protocol has been optimized from standard *Drosophila* larval staining methods described in pertinent literature (Karr and Alberts 1986). With an elegant array of motor subunit mutants already established from the robust live-imaging analysis described in Chapter 2, relative motor concentrations can be assessed and correlated to the resulting bulk vesicle trajectory analysis in an effort to test and further elucidate the intracellular mechanisms at play. After extensive efforts to achieve punctate staining within the segmental nerves of these animals, it was determined that the overwhelming soluble fraction of kinesin in addition to unavoidable staining of the entire nerve bundle, would prove to be too much of a roadblock to surpass. Subsequent attempts to take advantage of readily available motor deficient fly stocks, led to dissociating neurons from L3 larval central nervous system in cell culture (Wu, Suzuki et al. 1983). Despite having overcome the challenge of achieving punctate motor subunit immunofluorescence staining in axons of WT and motor deficient flies, the overall axonal processes would not grow more than ~3-4 times the diameter of the cell body. This unfortunately was not amenable to the relevant investigation, since the staining data required for this robust analysis was far too meager.

After several series of trials, neonatal mouse primary hippocampal culture was selected as the best system to conduct these experiments. Because of its densely packed layers of neurons, the hippocampus has frequently been used as a model system for studying intracellular phenomena. The long projections that are seen in primary hippocampal culture make them a highly desirable system for investigating axonal transport of cargo and provide reproducible punctate staining of desired proteins. Additionally, the hippocampus is one of the first regions of the brain to suffer damage in Alzheimer's disease (Hampel, Burger et al. 2008). The specific mouse neonate primary hippocampal culture protocol has been adopted from Tomas Falzone and Sandra Encalada, postdoctoral researchers in the Goldstein lab (Falzone, Stokin et al. 2009). Pups are collected on the day they were born (or through caesarean sectioning on approximately embryonic day (E)19-E20 in the case of fragile mutants). The brain is removed and both hippocampi are extracted in cold Hank's buffer solution (500mL HBSS, 0.4g D-glucose, 0.834g HEPES, 5ml pen-strep, filter sterilized and set to pH 7.3). Cells are dissociated through manual trituration following 20 minute incubation with the cysteine protease papain. They are then subsequently plated on coverslips treated with poly-L, and left to adhere to the glass in DMEM + 10% FBS media. After 1 hr, DMEM + FBS is removed, and the cells receive an optimal growth media (49 mL Neurobasal-A, 130 µL glutamax, 1 mL B27) in which they are left to proliferate at 37°C and 5.5% $CO_2$ for 10 days. Transfections (where applicable) are carried out on day 9, while all immunofluorescence is performed on day 10. Lipofectamine 2000 (Invitrogen) was used as the transfection reagent and optimal DNA concentrations were determined for each construct separately.

**Acquiring immunofluorescence data**

The specific antibodies used to probe desired motor protein subunits and APP were carefully selected and thoroughly tested to provide a reproducible assay as determined by detailed image analysis (see Antibody Validation). The following primary antibodies were chosen for motor colocalization IF experiments: anti-Alzheimer precursor protein (APP – Millipore C-term Jonas, MAB343 – mouse monoclonal IgG), anti-kinesin light chain 1 (KLC1 – Santa Cruz V-17, sc-13362 – goat polyclonal IgG), and anti-dynein heavy chain (DHC1 – Santa Cruz R-325, sc-9115 – rabbit polyclonal IgG). Ideally, an N-terminal APP antibody would be preferred since the C-terminus can be cleaved, but extensive efforts have shown that reproducible punctate staining cannot be achieved. Furthermore, in the particle tracking studies from Chapter 2, APP is tagged on the C-terminus and therefore allows us to compare staining to live imaging data between the systems where appropriate. Corresponding secondary donkey anti-mouse (Alexa Fluor 488), donkey anti-goat (Alexa Fluor 647), and donkey anti-rabbit (Alexa Fluor 568) antibodies were selected to minimize emission overlap and maximize signal. All secondary antibodies were raised in donkey to minimize crossreactivity (see Antibody Validation). Following standard primary culture protocols, cells were fixed with 4% paraformaldehyde plus 4% glucose, for 30 min at 37°C and 5.5% $CO_2$. Fixed cells were subsequently incubated for 5 min at room temperature with 0.1% Triton X-100 (TX-100) for permeabilization, and followed by a 45 min incubation in block consisting of 10% donkey serum, 3% BSA, 0.1% TX-100 in PBS. Coverslips were incubated with primary antibodies overnight at 4°C, washed 4 times with PBS for 5 minutes, then incubated with secondary antibodies for 1 hour at room temperature. The cells were

washed 4 more times with PBS to remove all unbound secondary, then mounted on slides using ~1.5µl of ProLong Gold (Invitrogen), an antifade reagent that suppresses photobleaching and preserves the signal of fluorescently labeled target molecules. Slides were left to dry for 1 hour, then sealed with standard nail polish.

The resulting immunofluorescence images show clear punctate staining – which we interpret as vesicular – for each channel, and a high degree of colocalization between APP vesicles and kinesin and dynein motor subunits (Fig. 3-1A). Images were acquired at 100X with a 1.4NA oil objective and using both an Olympus FV1000 confocal (pinhole adjusted to the equivalent of a 0.5 airy disc) and a Deltavision RT deconvolution imaging system. After careful examination and several attempts, images acquired from the Olympus Deltavision deconvolution system were selected as the standard for these efforts. Analogous image analysis efforts have recently proven successful using a similar Deltavision deconvolution imaging setup resulting in an elegant quantitative analysis of autophagy-related protein stoichiometry (Geng, Baba et al. 2008). Immersion oil was carefully selected based on mounting media used and sample/coverslip thickness. The refractive index of the oil was found to play a significant role in the quality of images acquired; Olympus immersion oil (n=1.5180) was decided upon and used for every applicable experiment.

Achieving reliable IF data is a major challenge, particularly in regard to robust image analysis efforts. The majority of antibodies tested did not produce punctate features, reproduce staining patterns well, or pass rigorous specificity controls. The particular antibodies selected provided the cleanest and most reliable images. Antibody dilution experiments were conducted to elucidate appropriate primary concentrations. For

both motor subunit probes, serial dilutions of primary in donkey block were prepared ranging from 1:50 to 1:200. A secondary-only antibody condition provides a measure of non-specific background intensity for comparison. Analysis of each condition is based on a dataset of at least 8 axons from 4 coverslips and 2 animals, resulting in over 1000 detected APP vesicles. Three measures of intensity are used to determine optimal antibody concentrations. Intensity levels were determined using ImageJ (NIH), where a line scan overlaid directly across the axon of interest provided the overall intensity distribution of the desired process. In all cases, the data suggests that a primary dilution of 1:100 for either KLC1 or DHC1 is sufficient to saturate the sample while minimizing background noise (Fig. 3-1B). There is a severe drop in intensity levels at 1:200 indicating antibody excess had not been achieved at these lower dilutions. Once primary antibody concentration was determined, a similar approach was used to determine optimal secondary dilutions. A concentration of 1:200 sufficiently saturated the sample and was used for all subsequent experiments. Additionally, a 1:100 dilution of anti-APP antibody was deemed appropriate following analogous criteria (not shown).

Axons were distinguished from dendritic projections by morphology and traced back to the cell body when possible. Extensive care was taken to ensure axonal projections were well isolated from adjacent features and spanned the field of view (67.9 um) in one optical section, remaining entirely in focus. Ideal axonal candidates were few and far between based on the strict criteria, limiting the maximum number of images for a given dataset to ~ 3/coverslip. Although achieving robust datasets that follow such stringent criteria require many replicates, the resulting data allowed for extensive analysis of biological and experimental variability (see Results).

Image capture was done with a 12-bit CoolSnap HQ, a fast, high resolution, high quantum efficiency, cooled CCD camera resulting in 512x512 images and a pixel size of 132.6 nm/pixel. Optical sections are spaced 300nm apart in each of the three channels, reaching the diffraction limit in the z-plane. Minimizing the optical spacing any further would result in no additional information, but rather an oversampling of the data on this instrument. Exposure times for each channel (FITC – APP; Cy-5 – KLC1; Texas Red – DHC1) were empirically determined at the beginning of each series of experiments, by determining the saturation point and scaling exposure to a level approximately 30% below, leaving room for future samples potentially containing features with higher intensity profiles. Once settings were established, they were kept constant throughout data collection.

**Intensity normalization approach**

Ideally, all imaging for a particular experiment is performed on the same day to control for the age and corresponding intensity variability of the mercury light source. Indeed, in many cases, a continuous imaging session was sufficient to collect all of the desired IF data for a given experiment, but comparison of intensity profiles between images collected on separate days was problematic. To control for this inevitable variation, a normalization method was developed to facilitate comparison between samples from experiment to experiment. Molecular Probes offers a microscope image intensity calibration kit which has proven to be instrumental for quantitative image analysis applications. The calibration kit includes 2.5μm diameter InSpeck beads that can be purchased in a range of colors that correspond with commonly used emission/excitation spectra. Beads corresponding to FITC, Cy-5, and Tx-Rd channels

were selected to evaluate the reproducibility of fluorescence intensity measurements from APP, KLC1, and DHC1 respectively, when acquisitions were performed under various conditions and on different days. Extensive analysis of the Inspeck beads shows that 1) standardization is possible 2) accurate and reliable fluorescence measurements can be obtained and 3) specimens showing large differences in fluorescence intensity can be objectively compared (Souchier, Brisson et al. 2003). These beads exhibit minimal bleaching and slides prepared with these calibration standards can be reused many times over. All beads were mounted on slides using ~1.5µL of ProLong Gold antifade reagent.

InSpeck beads were imaged at the beginning and end of image collection and calibration slides were replaced with fresh beads every three months. Three images were acquired for each channel before and after image acquisition, and pooled to provide a measure of bulb intensity for a given day. Results indicate a mild, yet consistent, decrease of intensity values over a two-week calibration time course (data not shown). When comparing between two datasets, sample intensity values were scaled according to the corresponding InSpeck profiles, allowing for reliable comparison of intensity values. This kit is particularly useful for acquiring images in shared microscopy facilities where the instruments are used for a wide variety of applications by many different users. Besides the primary function of providing a normalization scheme to compare quantitative intensity measurements between different imaging events, the beads can be used to evaluate the integrity of images acquired for a particular channel on a given day. Furthermore, since these beads are uniform in intensity, one can confirm that the entire image is being collected with an unvarying degree of intensity.

**Pixel registration correction**

For diffraction limited systems in particular, chromatic aberration of the fluorescent channels can complicate analysis especially when efforts are being made to precisely detect positions of desired puncta. Additionally, since each channel is collected using a different wavelength, these small differences can lead to shifts in the true position of features. Daily calibration and instrumentation adjustments are required for high-precision imaging of fluorescent probes. To account for these wavelength shifts in 3D, the pixel data from each channel and optical section needs to be corrected for all three planes (x-y-z). TetraSpeck (Invitrogen) microspheres are useful for verifying the ability of instrumentation to colocalize and resolve objects emitting different wavelengths of light in the same optical plane. Microspheres are stained throughout with four different fluorescent dyes, yielding beads that each display four well-separated excitation/emission peaks – 365/430nm (blue), 505/515nm (green), 560/580nm (orange) and 660/680nm (dark red). Beads are available in five diameters, spanning the range from subresolution to nearly cell-sized particles. To calibrate the instrument and determined settings, 0.5μm TetraSpeck beads were selected, diluted to a concentration of ~15,000 particles/uL, and mounted on slides using ProLong Gold medium. Two images, capturing 30 beads on average, were collected before any given imaging session using the 100X 1.4NA Deltavision objective. TetraSpeck calibration is required for each objective, established settings, and instrumentation used.

The automated pixel registration correction function available in the Volocity imaging software suite (Perkin Elmer) was used to correct for chromatic aberration and wavelength shifts of desired fluorophores in 3D. Optical stacks containing the TetraSpeck

calibration beads were input, and the software provided optimal registration correction. Results indicate that no shifts were needed in the x-y plane, and images were best corrected with a one slice upward shift in the A568 (DHC1) channel (Fig. 3-2). This correction was applied to all images in a series for each experiment prior to image analysis.

Additionally, registration issues were addressed in the context of a specific sample as opposed to an 'ideal' sample, such as the synthetic microspheres. Hippocampal cells were stained with anti-APP primary followed by a mixture of different color secondaries (donkey anti-mouse 488, goat anti-mouse 568, rabbit anti-mouse 647) corresponding to the APP mouse antibody. This effectively marked the same APP positions and intensities in the three channels corresponding to the aforementioned schema. Pearson correlation coefficients were calculated for intensity data from selected axonal projections in the resulting images using a hand-drawn line scan. The correlation coefficient significantly increased from r=0.81 in uncorrected images to r=0.92 when a z-shift of 1 in the A568 channel was incorporated. This one frame shift is reproducible for the given objective using both 'ideal' and 'specific' samples and was used for the pre-processing of images prior to each experimental analysis.

**Antibody validation**

The analysis of immunofluorescence data can only be as reliable as the images that are used. It is absolutely imperative that the antibodies selected and described above to detect position and intensity information are specific to their designated targets. Since DHC1 -/- mice are unavailable, the DHC1 primary antibody was tested in DHC1 shRNA transfected hippocampal cells. Validation of shRNA constructs for reduction of DHC1

was done by transfecting N2a cells separately with 3 sequences of each target using Lipofectamine 2000 (Invitrogen). Quantitative PCR was performed to test for reduced mRNA expression of DHC1 and a ~89% decrease in message levels was observed. Western blots using the DHC1 antibody in N2A cells indicated a >66% decrease in protein levels (Encalada, S., unpublished data). To test DHC1 antibody specificity in hippocampal culture, cells were transfected on day 9 with DHC1-shRNA with an mCherry marker, and subsequently stained with DHC1 using the established IF protocol. Transfection efficiency in hippocampal primary culture is often very low, and ~3% of cells successfully received the construct. Transfected cells showed marked decreases in DHC1 staining (Fig. 3-3A-D). Average anti-DHC1 intensity/$\mu m^2$ in shRNA transfected cells (n=9) was reduced by 72% compared to control non-transfected cells (n=11) (Fig. 3-3E). The magnitude in signal reduction is analogous to decreases in protein levels assessed by western blot, and confirms reliable specificity of this selected antibody probe.

To validate the KLC1 primary, several approaches were taken. First, to confirm that the KLC1 probe was thoroughly staining its specific target, cells were transfected with a KLC1-mCherry construct after 9 days in culture and blotted with the selected anti-KLC1 antibody. The KLC1-mCherry fusion protein produces punctate fluoresce and can be compared to the analogous anti-KLC1 staining. Signal from KLC1-mCherry shows a strong linear correlation (r=0.843) to anti-KLC1 IF data (Fig. 3-4), and further investigations suggest that close to 94% of KLC1-mCherry signal is picked up by the antibody. Secondly, KLC1 staining in null mice (KLC1 -/-) is performed to directly assess the specificity of the probe (see Results). We report a linear correlation between KLC1 intensities and KLC1 copy number by immunofluorescence. Cells from each

KLC1 genotype were stained with and levels were quantified on all KLC1-associated vesicles after estimation of Gaussian curves for each point source. Mean KLC1 intensity in KLC1 -/- vesicles was reduced by >68% as compared to KLC1 +/+ vesicles, after background subtraction. Furthermore, the KLC1 intensity signal increased with increasing KLC1 copy number, and this relationship was linear with a high regression coefficient ($R^2 = 0.99$), suggesting that relative quantitation of KLC1 levels is possible to assess with this antibody (Figure 4-5A). Furthermore, while it is possible that the residual KLC1 signal observed in KLC1-/- axons might be attributed to unspecific binding of the antibody, Western blot assays from KLC1 -/- mouse brain homogenates show high antibody specificity (Figure 4-5B), suggesting that the remaining signal corresponds to background fluorescent levels. We also observed a linear relationship between amounts of KLC1 detected with the same KLC1 antibody (V-17) and KLC1 copy number in Western blots of mouse brain homogenates (Figure 4-5C). In addition, we co-stained hippocampal neurons with antibodies against KLC1 and mitochondrial Cox1, and found no significant colocalization between the two markers, in agreement with reports that mitochondrial transport is independent of KLC1 function (Glater, Megeath et al. 2006), and further suggesting that the KLC1 antibody was specific.

### 3.2.2 Motor localization

The primary goal of collecting reliable IF data is to ultimately produce a robust analysis of KLC1 and DHC1 motor content on APP vesicles. We are looking to determine relative motor subunit composition of APP in control and KLC1 mutant animals. Optical microscopes and digital imaging have advanced to the point where recording fluorescent signal from tagged or blotted features has been routine for years.

Recently, the methods for analyzing these images and for the extraction of quantitative data of the localization and intensity of biological structures have been significantly advanced. The proposed 'motor localization' software provides reliable readouts of the relative amount of motor subunits for any type of cargo. First, puncta are detected in each IF channel – APP, KLC1, DHC1 – by fitting Gaussian functions to the diffraction limited data using an algorithm developed for automated tag detection (Thomann, Rines et al. 2002; Jaqaman, Loerke et al. 2008). Several methods have been reported for automatic detection and localization of spots (Netten, Young et al. 1997; Bornfleth, Edelmann et al. 1999; Goulian and Simon 2000; Kubitscheck, Kuckmann et al. 2000; Cheezum, Walker et al. 2001; Jaqaman, Loerke et al. 2008; Anthony and Granick 2009). However, most of these formulations neglect the complex case of partially overlapping, diffraction-limited spots. The punctate features observed in hippocampal axons stained with APP, KLC1, and DHC1 are not in isolation and therefore require additional consideration.

When two tags are separated by a distance smaller than the resolution limit, the superposition of their images gives rise to a single local maximum only. Thomann et al. address the problem of unresolved tags using a module for multiple spot detection. A candidate set of mixture models is built, where the best candidate model is selected based on pre-established goodness-of-fit criteria. The mixture model consists of a superposition of $n$ kernel functions and is formulated, in the case of diffraction-limited spots, as a superposition of $n$ Gaussians, each one representing a version of the point spread function (PSF) shifted in space. Based on simulations and indirect experimental evidence, iterative PSF fitting was found to overcome the diffraction limit by a factor of 3 – thus distances

of 80-100nm can be measured without super resolution microscopy (Thomann, Rines et al. 2002; Jaqaman, Loerke et al. 2008).

For detection, the most in-focus plane (after registration correction) is extracted for each raw image stack and channel and saved as *.tif. It is imperative to note, that raw (non-deconvolved) images are used for all analysis, as the deconvolution process alters pixel intensity data, and the Gaussian fitting algorithm itself can be viewed as model based deconvolution. Candidate frames are user selected and processed using ImageJ. Next, the user is asked to input the theoretical standard deviation of the point spread function (psf σ) for each channel based on the specific wavelength and objective used. The following equation is used to determine psf σ for each channel:

$$\text{psf } \sigma = \frac{0.21 * \left(\frac{\lambda}{\text{N.A.}}\right)}{\text{pixel size}}$$

where λ is the emission wavelength in nanometers, N.A. is the numerical aperture of objective, and pixel size is given in nanometers (Thomann, Rines et al. 2002). In reality, the light path is more complicated than what is theoretically assumed, so the algorithm starts with the user defined theoretical psf σ and attempts to iteratively estimate a more practical measure based on the raw data. Typically, the practical psf σ will turn out to be somewhat larger than the theoretical one, although once determined, remains constant during detection of an experimental series. Finally, the user determines alpha-values for detection statistics and initial local maxima assessment.

Once settings are determined, the algorithm scans a given image and marks intensity maxima positions (brightest pixel within a detected point source) after local background assessment for each punctate feature. Then, the algorithm iteratively attempts

to fit one or more Gaussian functions to the area surrounding a local maxima 'seed'. Position information is achieved at sub-pixel resolution, as the 2D fitting algorithm takes into account all local intensity information. Once a Gaussian is successfully fit, the code returns an estimated measure of point source intensity by outputting the Gaussian amplitude (Jaqaman, Loerke et al. 2008). Since, the standard deviation (σ) of Gaussians used is held constant for each channel and experimental series, relative intensity levels can be directly compared to achieve reliable readouts of fluorophore amount.

This detection provides robust position and intensity information for each channel and is stored in a data structure, which is subsequently parsed using custom MatLab (MathWorks) software. The 'motor localization' function takes the sub-pixel position information from a user selected region in any channel and reports the number of colocalization events and associated intensities from analogous optical sections within a user defined radius (Fig. 3-5). For the application of investigating subunit composition on APP vesicles, anti-APP staining serves as the seed channel; colocalization with corresponding anti-KLC1 and anti-DHC1 channels is instantaneously determined. The algorithm is optimized for running time, and computational expense is minimal for large datasets.

For all motor localization analysis, the cutoff for colocalization has been set at 300nm (~2.26 pixels). Percent motor association seems to plateau at about 300nm and begins to pick up motor subunit signal from adjacent APP vesicles at cutoffs>300nm. Additionally, based on the optics, resolution limit, and relevant biological dimension (biophysical context) of the vesicles and motor subunits, 300nm was determined to be an

appropriate threshold distance to quantify colocalization in this type of system (Encalada, Szpankowski et al. 2011).

Prior to colocalization analysis, intensity thresholds are determined to filter unwanted IF signal (noise). Secondary-only control images (samples are treated exactly as described above but are not incubated with any primary antibodies) are collected for each experimental dataset, and provide a measure of background fluorescence from Alexa Fluor probes within axonal projections. Dynamic range of background intensity for each channel is established in these control images and used to threshold detected features from experimental images by removing detected puncta for each antibody probe with intensities less than what is described by 95% of background range.

Immunofluorescence images are notorious for containing staining artifacts. Although every possible measure is taken to reduce staining noise in acquired datasets, selected axonal projections are not entirely free of artificats. IF artifacts typically manifest themselves as bright, large 'blobs' that can be easily distinguished from true signal. These 'blobs' are filtered by taking all intensity measurements for a given region and sorting them from largest to smallest. Staining artifacts generally have intensities greater than $\mu + 3\sigma$, and are traced back to raw images for manual inspection. An appropriate cutoff is determined based on these criteria and used for analysis of each experimental series.

The motor localization routine uses several pieces of information to execute its function. Users must input the following information (analogous to user interface terms used in current MatLab package – 'MotorLocalization_v10.m') :

- **RADIUS** – desired cutoff for colocalization (in nm)

- **PXLSCL** – size of individual pixel used for scaling (in nm)
- **C1_Thresh** – anchor (APP) threshold intensity values [n m]; n – bottom, m – top
- **C2_Thresh** – (KLC1) threshold intensity values [n m]; n – bottom, m – top
- **C3_Thresh** – (DHC1) threshold intensity values [n m]; n – bottom, m – top
- **AMPSCALE** – scales intensity values to desired magnitude (optional)
- **GAUSSIAN_DATA_C1** – location of Gaussian detection data structures (APP)
- **GAUSSIAN_DATA_C2** – location of Gaussian detection data structures (KLC1)
- **GAUSSIAN_DATA_C3**– location of Gaussian detection data structures (DHC1)
- **IMAGE_FILE –** location of Gaussian fitted image file (*.tif) for user to select desired region of interest (ROI) for analysis
- **IMAGE_NUM:** image number corresponding to IMAGE_FILE

In the motor localization code output, four APP vesicle categories are designated, those that had KLC1 only, DHC1 only, both motor subunits, or no motor subunits associated within a 300nm radius of an APP point source. The motor localization function output is divided into several sections. First, the sub-pixel localization coordinates and associated intensity amplitude of each APP vesicle is listed, followed by a readout that places it into its designated category. Next, a summary of percent motor association for all vesicles detected is output. Third, each KLC1 'hit' – KLC1 point source associated within 300nm of an APP vesicle – is listed, including sub-pixel position, intensity, distance from associated APP, and APP intensity. An analogous list for DHC1 is subsequently provided. Lastly, position and intensity measurements are accompanied by an associated error interval or goodness-of-fit, respectively (Thomann, Rines et al. 2002; Jaqaman, Loerke et al. 2008).

**Uncertainty in position data**

Positional accuracy is mainly influenced by two factors; the SNR and the point to point to point distance. To address the influence of the signal to noise ratio (SNR), simulations on isolated spots were conducted (Thomann, Rines et al. 2002). The statistical localization error is defined as:

$$err = \sqrt{\frac{1}{N}\sum_{i=1}^{N}|x_i - x_0|^2}$$

where $x_i$ is the estimated position of the tag, which is the center position of the Gaussian PSF approximation, and $x_0$ represents the true tag position from the simulation settings. The analysis confirms the well known fact that center positions of features with a known intensity distribution, in this case the distribution of the PSF, can be determined with sub-20nm precision (Bobroff, 1986; Inoue, 1989). For applications with a high SNR, the precision even reaches the single nanometer range. In the case of intensity data, a goodness-of-fit criteria is established and reported for each Gaussian amplitude as described in Thomann et al. See section 3.3.3 for uncertainty in position and intensity measurements in context of the biological application.

**Clustering**

Intensity amplitudes for APP vesicles (Section 3.3.2) were non-normal and were fit with four Gaussian modes using the mClust package in the R statistical computing environment. Optimal fits were selected using Bayesian Information Criterion (BIC) analysis, a robust statistic based on model-based clustering, that allows comparison of models with differing clusters (Fraley, 1999). Intensity distributions for APP, KLC1 and

DHC1 generally follow a mixture of four normal distribution modes $N(\mu_i, \sigma_i), i = 1,2,3,4$ where $\mu_1 < \mu_2 < \mu_3 < \mu_4$. The weight of each mode, denoted $w_i, i$ = 1..4, represents the fraction of segmental velocities in that mode. Classification of intensity values to a specific mode follow the same criteria as described in section 3.2 of the Appendix for classifying individual velocities into appropriate clusters.

**Statistics**

Statistical significance was determined using both parametric and non-parametric tests. Normality was assessed using the Anderson Darling and Lilliefors statistical tests. We accepted that samples in a population were not normally distributed when $p < 0.05$. A two-tailed Student's *t* test was used for comparison between normally distributed populations. Most parameters were not normally distributed so a non-parametric permutation t test was used (Moore and McCabe, 2005). For all tests used, *p* values < 0.05 were considered significant.

## 3.3 Results

### 3.3.1 Relative motor composition of APP vesicles in control animals

An estimate of motor composition on APP vesicles has not been previously reported in the literature. Attempts to measure relative motor association for different cargos has been extrapolated from force measurements using optical traps (Shubeita, Tran et al. 2008), bulk cargo isolations followed by western blot (Gross, Tuma et al. 2002; Hendricks, Perlson et al. 2010; Radtke, Kieneke et al. 2010), or inferring motor number from the velocity that cargos display in vivo (Hill, Plaza et al. 2004; Kural, Kim et al. 2005; Levi, Serpinskaya et al. 2006). However, no method has tried to quantify percent motor subunit association on a total population of a specific class of cargo at the individual vesicle level. In control animals, we observed that 70.5% ± 1.2% of APP vesicles colocalized with KLC1, 49.5% ± 1.1% associated with DHC1, and 38.5% ± 1.1% of APP vesicles had both motor subunits (Fig. 3-6). We did not detect any motor subunits on 18.5% ± 1.0% of detected APP cargo. Mean percent association is calculated per axon then averaged over all images in the dataset. Accordingly, variability is determined on a per images basis and reported in terms of the standard error of the mean (s.e.m.). The dataset examined 4,050 APP axonal vesicles, from 6 neonatal pups, 11 coverslips, and 34 distinct axons in 34 images, resulting in 2,824 KLC1 hits and 2,025 DHC1 colocalization events. The reported values are derived from two complete datasets acquired several months apart. Each individual dataset provided statistically insignificant differences in estimates of motor composition on APP vesicles. Of note, we use the motor localization method to confirm that cross-reactivity of secondary antibodies, an issue that was present during initial runs, is completely negligible. When we remove the primary

antibody for KLC1 or DHC1 and leave all other parameters unchanged, motor association with APP for the subunit in question drops by 95% and 93% respectively (data not shown).

### 3.3.2 Percent motor subunit association scales proportionally to amount of APP

The motor localization software package not only returns percent association of motor subunits with APP, but also a robust measure of intensity for each of the 3 proteins involved in the colocalization study. Several groups have reported a linear relationship between protein amount and the associated fluorescence intensity (Wu and Pollard 2005; Geng, Baba et al. 2008). This suggests that, within a certain range, the fluorescence intensity is determined by protein amount independent of what protein is tagged by the fluorophore or where the tagged protein is localized. This information can be used to infer local concentrations of participating proteins in an effort to understand complicated cellular phenomena.

Resulting intensity measurements for APP showed a non-normal right-skewed distribution. To break down the observed APP intensities into statistically robust normally-distributed clusters, we used the mClust software package in R (see Methods). Intensity distributions of associated motor subunits are discussed in section 3.3.4. Bayesian Information Criteria (BIC) is employed to determine optimal clustering of resulting intensity profiles and shows that APP intensities are best described by a series of 4 clusters (Fig 3-7A). Note, that regardless of the number of bins used to display the resulting distribution, clustering results remain constant. The mean of each cluster resides at 51.0, 106.6, 214.7, and 337.4, describing 24.1%, 26.6%, 32.6%, and 16.6% of the data respectively. Cluster modes roughly correlate to a 1X, 2X, 4X, 6X pattern of APP

intensity which can be viewed as multiples of the amount of APP that resides in each particular axonal vesicle detected within the selected region of interest. Gaussian amplitude measures for each detected APP point source were classified into different modes by calculating classification thresholds (see Methods). Cluster 1 represents APP vesicles belonging to the lowest intensity group, while cluster 4 contains vesicles with the highest intensity readouts.

Motor association for all vesicle classes was determined for each separate cluster. Intriguingly, the percent of KLC1 and DHC1 motor subunit association seemed to increase proportionally with growing intensity cluster (Fig. 3-7B). In cluster 1, 61.6% ± 2.1% of APP vesicles were found to be associated with the KLC1 subunit of kinesin-1, 65.7% ± 2.0% in cluster 2, 74.3% ± 1.8% in cluster 3, and 77.8% ± 2.6% in cluster 4. This result suggests that APP plays a role in recruiting KLC1 to the vesicle surface. APP has in fact been shown to bind KLC1 in coimmunoprecipitation, sucrose gradient, and in vitro binding experiments (Kamal, Stokin et al. 2000), validating the proposed result and the robustness of the method (see Discussion). Although a direct interaction has been reported between APP and KLC1, investigations regarding APP and DHC1 association on the individual cargo level have been scarce and inconclusive. We report here that DHC1 subunit association with APP scales with increasing intensity cluster, similar to the effect noted for the light chain of kinesin-1. APP vesicles belonging to cluster 1 show a 42.2% colocalization with DHC1, 47.3% for cluster 2, 52.0% in cluster 3, and 62.8% DHC1 association within the 300nm designated radius in cluster 4.

Accordingly, association of both motor subunits for a particular APP vesicle increase with amount of APP detected from 30.45% to 51.2%, while the percentage of

cargos with no detected motor subunit decreases from 26.7% to 10.6% from clusters 1 to 4 respectively. Taken together, this information provides novel evidence for APP's role in recruitment of motor subunits to the vesicle surface.

### 3.3.3 Uncertainty in position and intensity measurements in context of the biological application

A critical consideration when interpreting position and intensity data is the relative accuracy and associated error in these components. For each detected feature in APP, KLC1, and DHC1 channels, the Gaussian fitting algorithm determines a measure of uncertainty in the x-coordinate, y-coordinate, and in the case of amplitude intensity measurements, a goodness-of-fit. The size of the detected puncta, surrounding signal to noise ratio (SNR), local background, and neighboring features all play a role in this uncertainty (see Methods).

To determine the relevant uncertainty in positional estimates in both the x- and y-coordinates for the APP anchor channel, the distribution is presented for 6 randomly selected control animals (Fig. 3-8). The average uncertainty for x- and y- is 29.6nm and 29.9nm respectively. Hence, with an established threshold of 300nm for each colocalization event, we detect features with ~90% accuracy. Additionally, 92.6% of the position data has an uncertainty of less than 60nm. For the same test set, an average intensity amplitude uncertainty of 7.2% is determined, based on the goodness-of-fit of each Gaussian function. In summary, the position and intensity measurements seem to fall within a reasonable uncertainty interval for the desired application.

### 3.3.4 APP associated motor subunit intensity analysis

Although we have determined that the percent of APP vesicles associated with a particular motor subunit scale proportionally to the amount of APP in the vesicle, intensity correlations between the motors and cargo have yet to be investigated. Many studies have confirmed the linear relationship between intensity and amount of protein (Wu and Pollard 2005; Geng, Baba et al. 2008), so to elucidate possible links between the amount of motor and amount of APP within a vesicle, we plot the correlation for three of the designated categories of cargo; those that had KLC1 only, DHC1 only, and both motor subunits (Fig. 3-9). We report a statistically significant correlation value between APP and KLC1 ($r = 0.56$), APP and DHC1 ($r = 0.24$), as well as KLC1 and DHC1 ($r = 0.34$) intensity values. To determine statistical significance for coefficients of correlation between motor subunit and APP intensities combinations, we first obtained 10,000 bootstrap replicates of each correlation coefficient to determine its distribution. We subsequently calculated the maximal (3o) range of correlation coefficients under random pairings for each intensity comparison (Fig. 3-9D; indicated by the black horizontal bar).

This finding suggests that there is some degree of coordination between the amount of motor subunits and APP on the vesicle surface. The more of each motor associated with a particular APP cargo seems to recruit more of its molecular counterpart to the surface (e.g. the more KLC1 on a vesicle, the more DHC1 is associated; see section 3.3.6). Of note, this effect does not stem from any bleed-through (crosstalk) between channels during image acquisition, as the channels are sequentially scanned and the carefully selected Alexa fluorophores used to mark each protein are well separated and show negligible spectral overlap.

APP associated KLC1 intensity distributions are non-normal and skewed to the right (Fig. 3-10A). Model-based clustering followed by BIC selection results in 4 distinct clusters that best describe the overall distribution. The mean of each cluster resides at 33.3, 63.4, 110.9, and 203.8, making up 20.6%, 26.7%, 33.3%, and 19.3% of the data respectively. Intriguingly, the mode centers follow approximately a 1:2:3:6 ratio, presumably corresponding to multiples of KLC1 associated with detected APP vesicles. It is possible that we do not see the 4X, 5X quantiles because as the data thins out at higher intensities, we do not have enough information to distinguish these modes and assign statistically significant clusters to them.

Accordingly, APP associated DHC1 intensity distribution are observed to be right skewed as well. Clustering results show 4 separate modes, with means positioned at 26.9, 60.5, 117.9, and 248.4, describing 23.8%, 24.0%, 22.3%, and 29.9% of the data respectively (Fig. 3-10B). For DHC1, the mode centers follow approximately a 1:2:4:9 ratio. The nature of the apparent multiples is somewhat less clear in the case of DHC1, yet almost 50% of the intensity data is made up by the 1X, 2X clusters.

### 3.3.5 Relative motor composition of APP vesicles in KLC1 genotypes

One of the primary goals of establishing a robust method to investigate motor subunit composition on the individual cargo level was to help explain some of the findings from tracking studies (Chapter 2). Results from our group and others have indicated an impairment of retrograde transport in kinesin-1 mutants or when kinesin-1 function is inhibited (Brady et al., 1990; Colin et al., 2008; Kim et al., 2007; Martin et al., 1999; Pilling et al., 2006; Fig. 2-3), suggesting coordination mechanisms between motor subunits on transported cargos. Reducing kinesin-1 levels in a variety of systems has

resulted in significant decreases in anterograde as well as retrograde velocities and run lengths. To account for this observation, we propose the following three hypotheses:

i) *Activation hypothesis* – Kinesin-1 activates dynein; hence, reductions in kinesin-1 impair retrograde transport by decreasing activation of dynein subunits on cargo surfaces.

ii) *Loading impairment hypothesis* – Loss of kinesin-1 on cargo leads to reduced dynein on vesicles. So, kinesin-1 mutants exhibit an impaired dynein loading phenotype.

iii) *Sampling bias hypothesis* – Distal regions of the axon perhaps display a ratio of kinesin-1:dynein-1 (K:D) > 1. This sampling bias arises when kinesin-1 levels are reduced and vesicles with (K:D) < 1 preferentially return to the cell body and ultimately do not pass through the imaging region. Our data reveal that the number of moving vesicles significantly dropped from ~30 to ~10 in all kinesin-1 reduction genotypes, an effect no other genotype exhibited (Fig. 2-4G-H).

To attempt to distinguish between these three hypotheses, a method to investigate motor levels on individual vesicles needs to be employed. Do decreases in kinesin-1 levels leads to reductions of dynein on the vesicle? Does a gradient of kinesin-1 to dynein-1 exist as a function of distance from the cell body? The sampling bias hypothesis, if true, can make confirming the effect proposed in the loading impairment hypothesis difficult to interpret. Ideally, we need to look at motor composition of APP vesicles as a function of distance from the cell body.

To investigate the phenomenon of retrograde impairment in kinesin-1 mutants, we selected mice with no copies of KLC1 (KLC1 -/-; nulls), one copy (KLC1 +/-; hets), and both copies (KLC1 +/+; WT). Neonates were acquired on embryonic day (E)19-E20 through caesarean section as KLC1 -/- pups often did not make it to birth alive. All resulting pups from an individual litter were promptly plated using the standard cell culture protocol described in the Methods section, and subsequently genotyped. The following results are based on 2 complete datasets, acquired several months apart, consisting of 10 images for each condition. The resulting analysis from 60 (10/condition per dataset) images is summarized below (Fig. 3-11).

As expected, we observe significant decreases in the amount of KLC1 associated within 300nm of a detected APP vesicle feature as KLC1 copy number is genetically reduced. For KLC1 +/+ we report that 55% ± 1.4% of APP vesicles colocalize with KLC1, 42.3% ± 1.6% for KLC1 +/-, and 23.1% ± 1.2% in KLC1 -/-. Although KLC1 levels in null KLC1 mice did not decrease to background (outside of selected axonal ROI) levels of 3.4% ± 0.43, a highly significant drop was observed. We offer an explanation including additional analysis on intensity profiles to account for this artifact (see 3.4.3 of the Discussion).

To directly address the question of DHC1 levels on APP vesicles in KLC1 reduction background, we report significant reductions of DHC1 subunit association as a function of KLC1 copy number. In KLC1 +/+ 48.9% ± 1.5% of vesicles are associated with DHC1, 37.2% ± 2.1% in KLC1 +/- and 33.0% ± 1.0% in the null KLC1 -/- animals. Background levels for DHC1 show 4.0% ± 0.7% motor association. This novel finding shows that the percentage of DHC1 associated with APP vesicles is in fact decreased as

KLC1 levels are reduced. The resulting reduction of DHC1 association from KLC1 +/+ to KLC1 +/- is highly significant, while KLC1 +/- to KLC1 -/- decreases are borderline significant depending on the exact statistical test used (p-values range from 0.033 to 0.088). Of note, for all other comparisons both the two-tailed student's t-test and the non-parametric permutation t-test result in highly significant differences.

Accordingly, we observe significant drops in the number of APP vesicles associated with both motors and substantial increases in the number of vesicles with neither motor subunit detected as a function of KLC1 copy number. Vesicles colocalizing to both motor subunits decrease from 28.3% ± 1.5% to 16.6% ± 1.5% to only 8.8%± 0.6%, while those associated with neither subunit increase from 24.5% ± 1.0% to 37.0% ± 1.8% and ultimately to 52.7% ± 1.2% in KLC1 +/+, KLC1 +/-, and KLC1 -/- genotypes respectively.

All in all, these observations refute the activation hypothesis and support predictions outlined in both the loading impairment and sampling bias hypotheses. To distinguish between the remaining theories, additional information is required. To thoroughly test for a sampling bias in the proposed data, axonal regions need to be imaged at a set distance from the cell body. This is unfortunately very difficult to accomplish since projections overlap and become extremely difficult to trace back to the cell body once one begins to move away from the clearly defined cell body. The axons tend to bifurcate presenting an additional layer of complexity. To resolve this issue, soluble cyan fluorescent protein (CFP) is transfected prior to coverslip fixation. We exploit the low transcriptional efficiency (~3%) of cultured hippocampal cells (Encalada, Szpankowski et al. 2011) to essentially mark the cell body and associated projections of a

small subset of cells allowing us to acquire images at a set distance from the cell body. This additional channel is well separated from other colors used in the protocol and hence does not interfere with the desired antibody signals. Although theoretically feasible, we have determined that acquiring this data is prohibitively challenging due to the strict criteria established for candidate axonal regions. When imaging random distances from the cell body as has been done for all reported datasets this far, we can be incredibly selective in finding suitable regions. It is imperative that these selected axonal regions are well separated from adjacent cellular features and most importantly, stay in focus in one optical plane. Since, acquiring suitable motor localization data at set distances from the cell body is not feasible with the current framework, we use other, more available, information to distinguish between the loading impairment and sampling bias hypotheses.

The sampling bias theory was first proposed based on the observation that the number of moving particles in kinesin-1 reduction mutants was reduced to ~10 per field of view compared to ~30 in all other genotypes (Fig. 2-F). The IF data used for motor localization cannot distinguish between moving and stationary particles, but we do not see any difference in the number of detected APP vesicles as a function of KLC1 gene dose (Fig. 3-12). We observe ~10 APP vesicles per 10μm of axon for each KLC1 genotype. Accordingly, the number of associated KLC1 and DHC1 motor subunits follows the same trend as outlined in the KLC1 motor subunit composition results summarized in Fig. 3-11. This suggests that a sampling bias is not present in our data, since the same number of APP features were found on average in each imaged region of the axon irrelevant of the amount of KLC1 or DHC1 present on the surface of cargo. Although this evidence is not as strong as the ideal motor localization analysis as a

function of distance from the cell body, taken together, these results support the loading impairment hypothesis outlined above.

### 3.3.6 APP associated motor subunit intensity analysis in KLC1 genotypes

To investigate changes in relative motor amount associated with APP vesicles in KLC1 genotypes, we present all 3 distributions for KLC1 and DHC1 separately (Fig. 3-13A-B). Clustering each distribution results in complicated combinations of detected modes, which prove to be difficult for statistical comparison. Instead, we overlay each genotype's motor subunit intensity measurements onto one graph for simplified evaluation. The distributions are presented as a function of relative frequency of the total number of APP vesicles detected. The intensity distribution for KLC1 +/+ closely follows what was observed in control animals presented in section 3.3.4. When one copy of KLC1 is removed, we notice a significant shift to lower Gaussian intensity amplitude values (<100) at the expense of higher amplitude values (>100). This observation suggests that although one copy of the gene is removed, we still see vesicles with multiple KLC1 subunits associated with APP. These multiples are less common than in the KLC1 +/+ animals, but a significant peak in smaller intensity values, presumably corresponding to 1 or 2 KLC1 subunits are significantly enhanced. KLC1 -/- animals show highly significant reductions for all KLC1 intensity values as expected. Theoretically, we would predict no KLC1 association on APP vesicles (or more precisely, background levels of 'KLC1' association of ~3.4% ± 0.4% in the staining data) when both copies of the gene are removed. We attribute this antibody staining 'artifact' to two possible sources; non-specific detection of the KLC2 subunit and a small fragment of KLC1 that has been observed to be left over in KLC1 -/- mutants (Chun-hong Xia,

unpublished data). Confirming the detection of the left-over KLC1 fragment is difficult and out of the scope for this study, however we attempt to shed some light on the proposed KLC2 non-specific binding cross-reactivity by reducing KLC2 message using a KLC2-shRNA construct. Results indicate minor, yet significant ($p = 0.041$) reductions in signal detected by the selected KLC1 antibody in KLC2-shRNA transfected cells, suggesting that our antibody does in fact pick up at least a subset of KCL2 signal, explaining why we do not see full reduction of KLC1 motor subunit association and intensity in KLC1 -/- animals. Furthermore, sequence analysis confirms KLC2 shares a conserved region with KLC1 where the epitope that the V-17 KLC1 antibody used for the study recognizes (a proprietary 12-20 amino acid region contained between amino acids 500-550). Lastly, since KLC1 -/- animals live to at least embryonic day 19 and in some cases until adulthood, we speculate that KLC2 may take over a portion of the transport of APP vesicles in KLC1 -/- genotypes. This redundancy of subunits has been previously proposed in mammalian systems (Encalada, Szpankowski et al. 2011). Thus, we offer that at least the unspecific detection of KLC2 by anti-KLC1 we observe can explain the resulting staining artifact.

Our data suggests that the percent of DHC1 associated within a 300nm radius of detected APP vesicles decrease as KLC1 levels are reduced. To investigate relative levels of DHC1 as a function of KLC1 gene dose, we turn to the Gaussian intensity amplitude measurements (Fig. 3-13B). We notice a significant decrease in the percentage of APP vesicles associated with multiple DHC1 subunits (intensity > 180) when comparing KLC1 +/+ and KLC1 +/- results. Surprisingly, we report no difference in the number of cargo with low intensity profiles (40 – 180) in these genotypes. The distinction between

KLC1 +/- and KLC1 -/- animals is more subtle, with no differences noticed for high intensity DHC1 features, and minor significant reductions for the lower levels. We do see that the most frequent category (low level particles 40-80 – 12.8% of total APP vesicles) in the absence of KLC1 actually are more common than either KLC1 +/- or KLC1 +/+. This finding suggests that KLC1 is required for normal DHC1 loading, and proper association of the DHC1 subunit with APP vesicles is significantly disrupted when one copy is reduced. Removing both copies perturbs the systems further, but the decreases are less pronounced. This slight drop off comes at the expense of low level amounts of the subunit while maintaining similar levels for vesicles in the higher intensity categories corresponding to multiple DHC1 associations.

**Discussion**

In this study, we set out to investigate the motor composition and associated relative amounts of kinesin light chain-1 (KLC1) and dynein heavy chain-1 (DHC1) motor subunits on APP vesicles in control animals and as a function of KLC1 gene dose. We have examined how select motor subunit reduction and overexpression affect the overall transport of APP vesicles in live *Drosophila* 3$^{rd}$ instar larvae segmental nerves (Chapter 2), but elucidating endogenous motor subunit levels and architecture on individual vesicles has been elusive. We present here a novel method to address these significant challenges using quantitative immunofluorescence (IF) in mouse primary hippocampal culture.

Previous investigations into elucidating the number and type of motor subunit associated with cargos have been limited for various reasons. Efforts to isolate cargos of interest followed by quantitative analysis of motor protein levels by western blot have been done for a number of systems (Gross, Tuma et al. 2002; Hendricks, Perlson et al. 2010; Radtke, Kieneke et al. 2010). For example, it has been shown that vesicles can be isolated using membrane floats on sucrose gradients. However, these data are difficult to collect and the results from experiment to experiment are highly variable. Additionally, this type of 'bulk' analysis does not shed light on relative motor composition on the individual cargo level, but rather as a whole population. This type of observation substantially limits the amount of information that can ultimately be extracted since motor number may vary from cargo to cargo or even on single cargo over time.

Furthermore, several studies attempt to infer motor number from the velocity that cargos display in vivo; faster cargos are assumed to have more motors engaged (Hill,

Plaza et al. 2004; Kural, Kim et al. 2005; Levi, Serpinskaya et al. 2006). Although informative, the interpretation of this indirect measure is likely complex as the loads that cargos display in vivo may not be high enough to explain observed velocity variations and it is unresolved whether velocities are also modulated by regulatory factors. Other methods have attempted to determine motor number on individual cargo more directly by using force measurements (Shubeita, Tran et al. 2008). Estimates for the number of engaged motors are achieved by calculating the force needed to stall a moving cargo. Theoretical considerations predict that such stall forces are proportional to the number of active motors. In vitro, this has been confirmed for both kinesin and cytoplasmic dynein. Nevertheless, these force measurements are technically challenging and achieving robust datasets has proven difficult, particularly in the case of vesicle transport in axons. Additionally, direct force measurements used to determine the number of actively engaged motors on a particular cargo provides little insight into overall motor composition of these cargos. Since vesicles switch directions and presumably alter which motor or set of motors are actively engaged in millisecond time frames, overall motor composition is certainly critical to the overall understanding of coordination mechanisms.

The quantitative immunofluorescence method we present has the advantage of looking at motor association for a wide variety of cargos in vivo. Further, it can produce substantially large datasets describing the overall population of vesicle composition which can be used for robust analysis of intensity and percent association measures. The Gaussian fitting algorithm we use has several advantages over previous methods described for spot detection. First, it does not neglect the complicated case of partially overlapping spots which occurs when fluorescent markers are positioned at distances

below the diffraction limit. Other studies have provided frameworks for dealing with these cases, but since they are only interested in the number of present spots they do not localize the spots individually, considerably restricting the level of accuracy for diffraction-limited colocalization studies.

The Gaussian amplitude based intensity readouts that we achieve for APP and the motor subunits KLC1 and DHC1 can be used to indirectly infer motor amount on vesicles. First, for both KLC1 and DHC1 intensity distributions (Fig. 3-10), we observe that a substantial amount of the data occurs in peaks corresponding to 1X, 2X multiples, presumably corresponding to 1 or 2 associated motors respectively. In the case for KLC1, we even see a significant peak at 3X. This evidence is encouraging in the sense that these apparent multiples are in line with many of the current estimates of motor number per vesicle based on other methods and the overall physical size of the molecular players involved. Realistically, it does not seem that we can have dozens of motors associated with an individual vesicle of average size given the apparent dimensions of the complex (Fig 1-1).

We report several interesting new features of motor subunit coordination based on our method. First, we report a relative readout of KLC1 and DHC1 subunit association on APP vesicles for control animals. A measure of the percentage of cargo that colocalize with a particular subunit is novel and critical to extend our understanding of axonal coordination mechanisms. Intriguingly, we find that KLC1 and DHC1 relative amounts and general association with APP scales proportionally as a function of APP amount in vesicles. In this view, APP seems to recruit these motor subunits to the vesicle surface, which is in line with reports that observe direct interaction between APP and the TPR

domain of KLC1 (Kamal, Stokin et al. 2000). However, this sort of interaction has not been reported for DHC1 and APP. Secondly, we provide a rigorous analysis of motor subunit amount and percent composition in 3 KLC1 genotypes. Our results propose that KLC1 is in fact necessary for proper loading of DHC1 on APP vesicles and may explain retrograde defects associated with kinesin-1 reductions.

The method we developed for super-resolution colocalization of diffraction limited fluorescent puncta can be applied to a variety of systems. This method can assess relative association between any number of tagged proteins or cellular features in diffraction limited systems. The immediate application was used to assess motor subunit concentration on APP vesicles, but was additionally used to characterize the composition of motor machinery on $PrP^C$ vesicles in a recent published study (Encalada, Szpankowski et al. 2011). The assay has been tested on transfected KLC1-mCherry and APP-YFP constructs and performs well. In fact, motor association of KLC1-mCherry and APP-YFP result in strikingly similar readouts of the relative amount of motor subunit associated when compared to the tightly controlled immunofluorescence data. All in all, this method can bypass the use of super-resolution microscopy and predict underlying position information as well as relative concentrations for proteins of interest. Super-resolution microscopy systems, like stimulated emission depletion microscopy (STED), photo-activated localization microscopy (PALM), stochastic optical reconstruction microscopy (STORM), or the Deltavision OMX (from Applied Precision Instruments) can result in higher spatial resolution image stacks in multiple colors are becoming more common. However, these instruments are often prohibitively expensive and may require special, and sometimes limiting, preparation protocols. Furthermore, the colocalization method

we propose can easily be used to analyze existing datasets and extract information that was previously buried and unreachable.

Chapter 3, in part, is currently being prepared for submission. Szpankowski, L., S.E. Encalada, L.S.B. Goldstein. “Elucidating the Relative Motor Subunit Composition of APP Vesicles.” The dissertation author was the primary investigator and author of this paper.

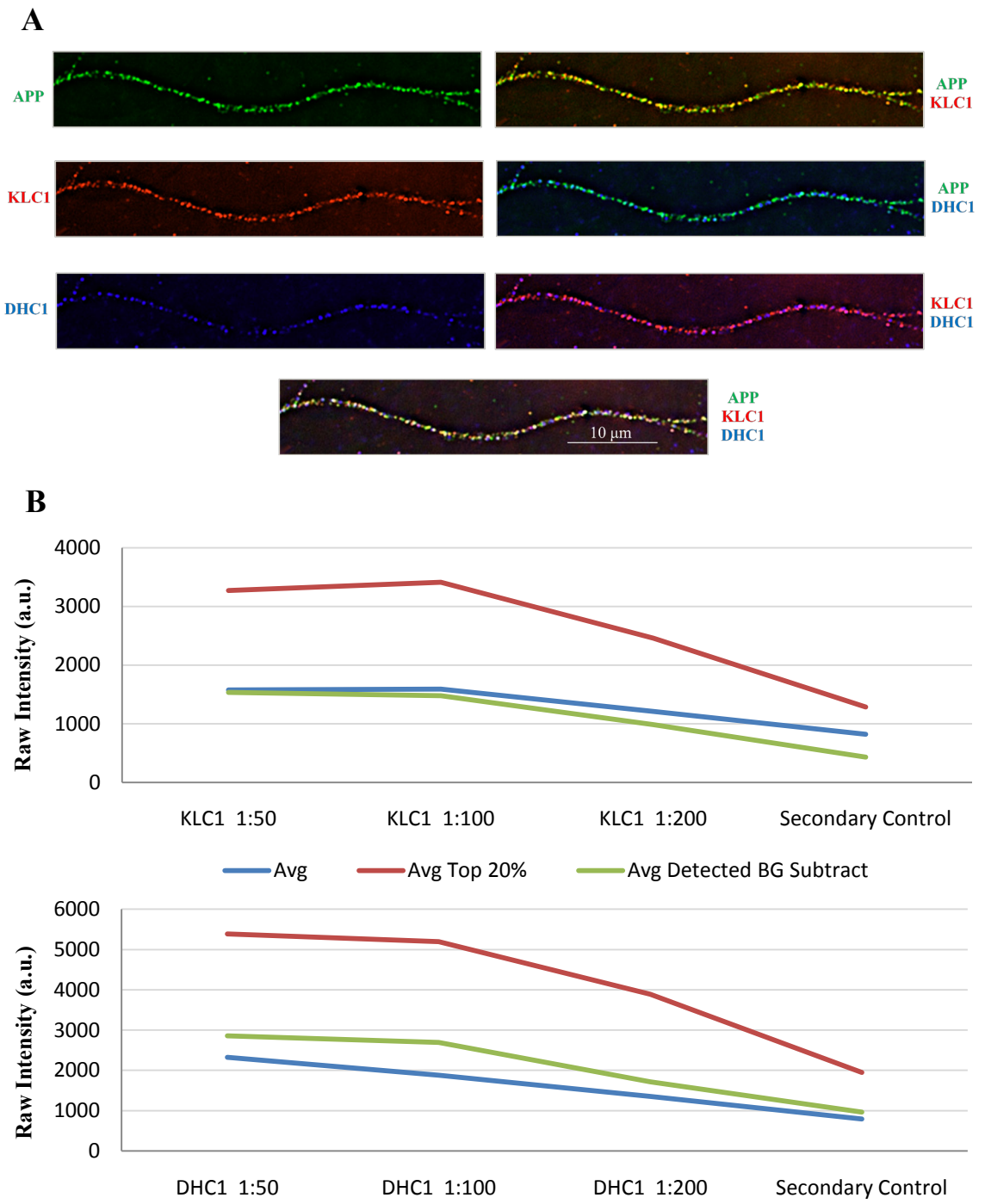


**Figure 3-1** Acquiring robust immunofluorescence data. A) Mouse primary hippocampal culture system produces punctate immunofluorescence staining for each selected protein. There is a high degree of colocalization between APP and motor subunits KLC1/DHC1 in axons. Images acquired at 100X. B) A 1:100 dilution of KLC1 and DHC1 antibody probes sufficiently saturate the sample. Three measures of intensity are shown: Avg – mean intensity of all signal within axon; Avg Top 20% - mean intensity of top 20 % of axonal signal; Avg Detected BG Subtract – mean intensity of detected axonal puncta (local max) after background subtraction. For each measurement: $N_{animal} = 2$; $N_{coverslip} = 4$; $N_{axon} = 8$; $N_{intensity\_value} > 1000$.

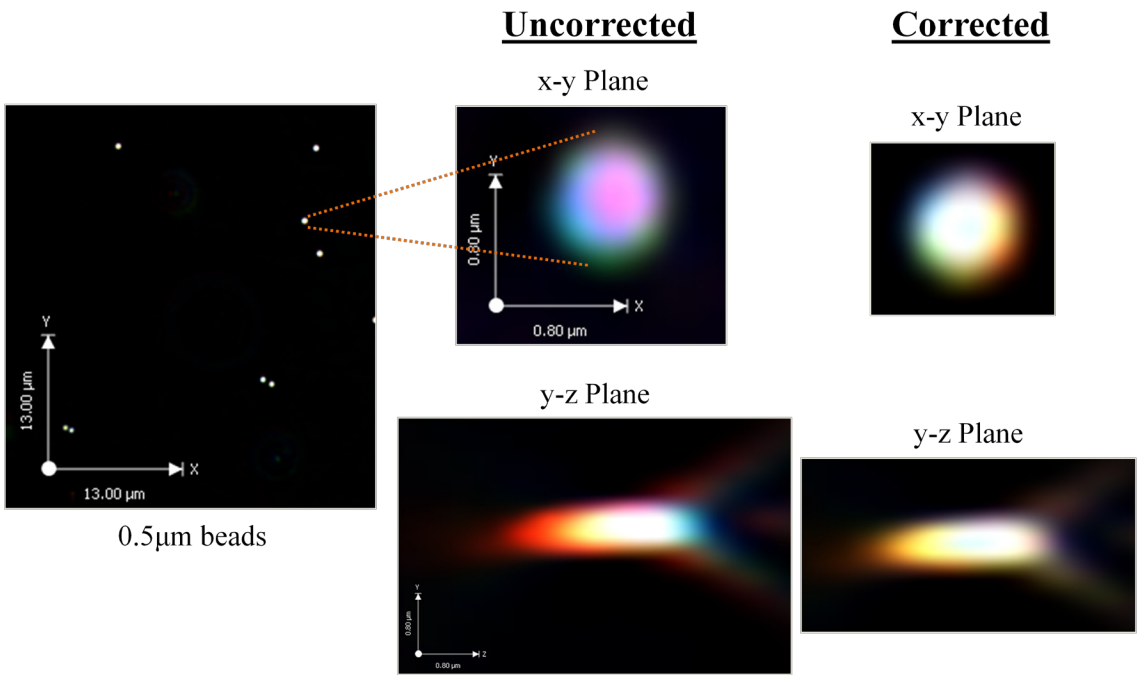


**Figure 3-2** Alignment of A647, A488 and A568 fluorescent channels with TetraSpeck microspheres. Left panel shows a portion of a raw bead image acquired using a 100X 1.4NA objective on the RT DeltaVision Deconvolution system. Middle panel shows a zoomed uncorrected (raw) single bead in both the x-y and y-z planes. Volocity software pixel registration correction indicates a +1 optical slice upward shift in A568 is sufficient to align signal and account for aberration. (A488: anchor; A647: x=0,y=0,z=0; A568: x=0, y=0, z=+1). Right panel shows microsphere in x-y and y-z planes after correction.

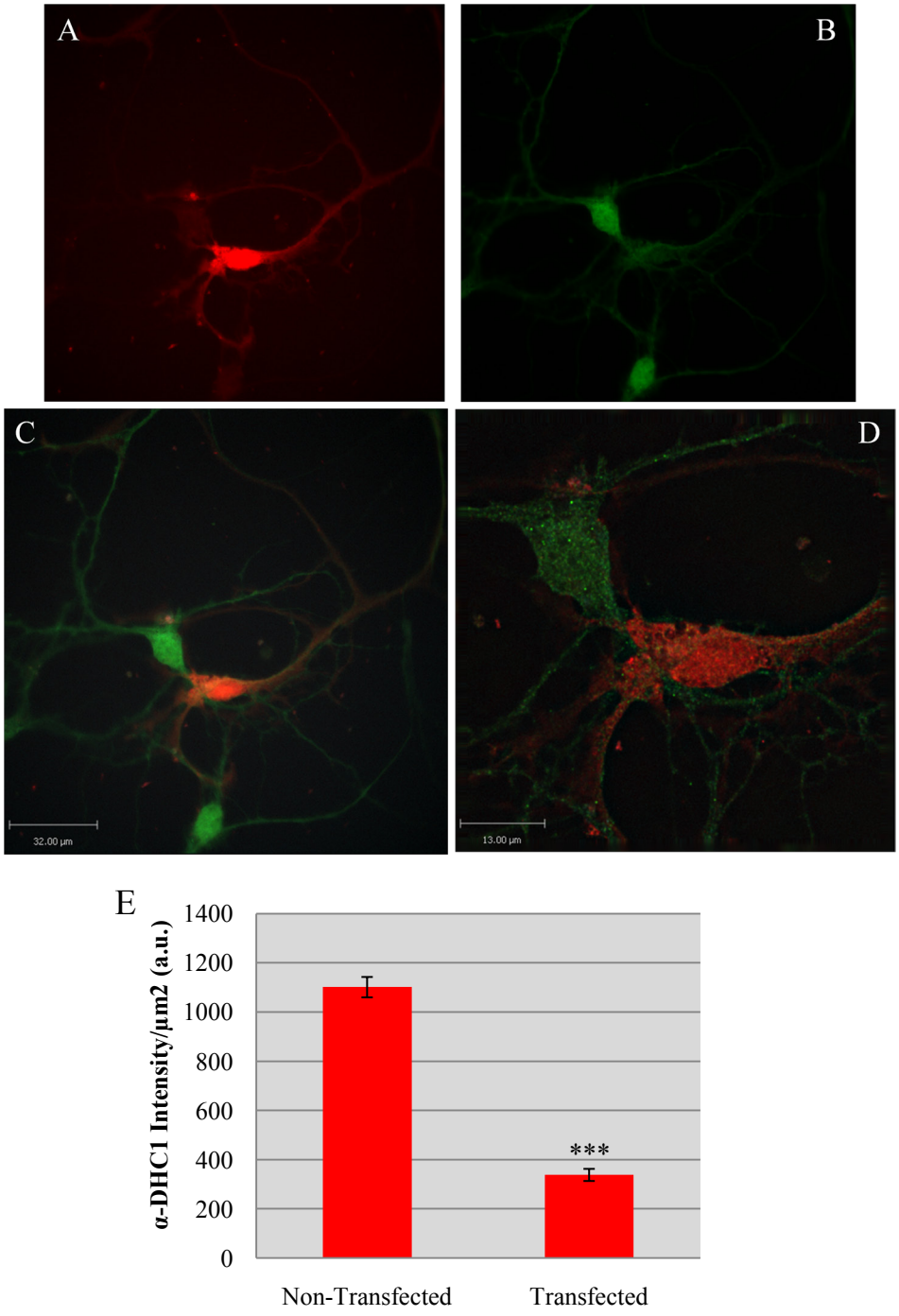


**Figure 3-3** Validating DHC1 antibody specificity. A) 40X image showing three hippocampal cells, only one of which is transfected with DHC1-shRNA mCherry. B) Image shows anti-DHC staining at 40X, indicating a strong decrease in DHC1 intensity in the transfected cell. C) Merge at 40X (C). D) Merge at 100X – upper non-transfected cell shows normal DHC1 staining, while lower transfected cell indicates a marked decrease. E) Quantification of intensity/$\mu m^2$ decrease in transfected cells ($N_{cells}$=9) versus non-transfected cells ($N_{cells}$=11). (D). Error bars show s.e.m. * $p<0.05$ ** $p<0.01$ *** $p<0.001$

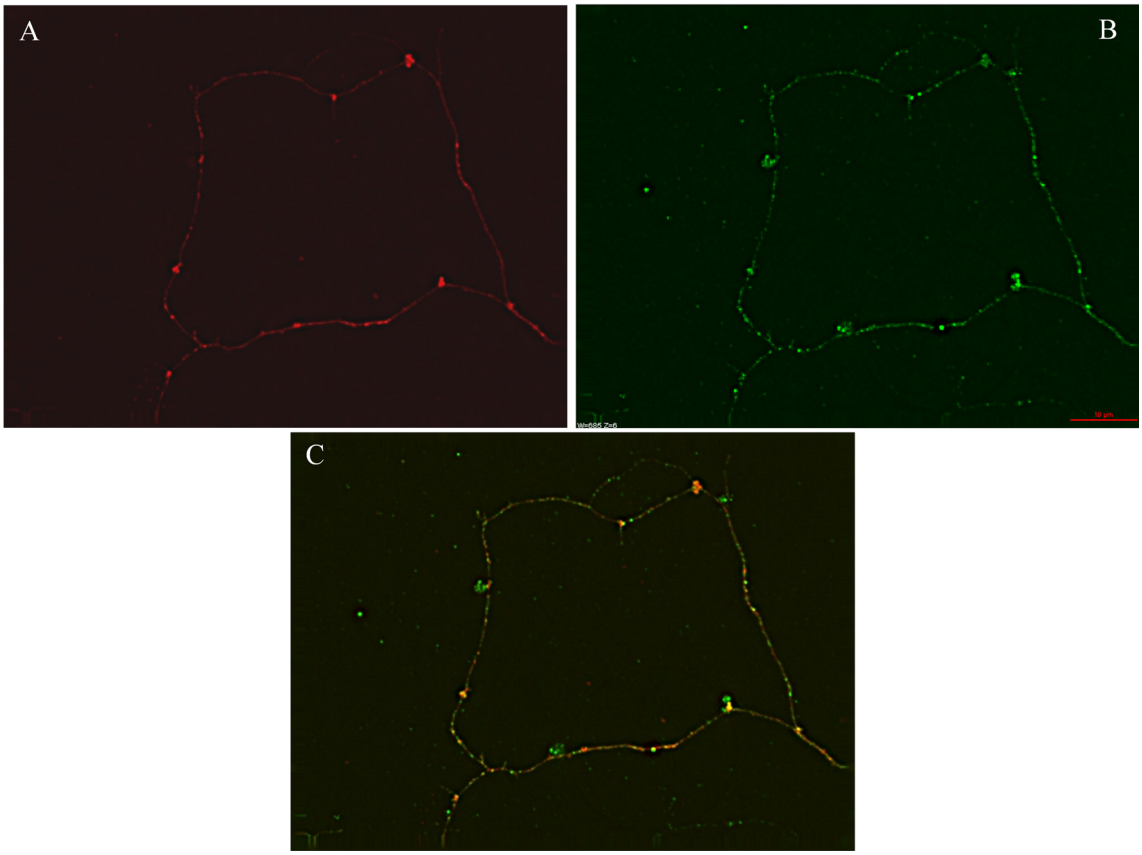


**Figure 3-4** Validating KLC1 antibody specificity. Anti-KLC1 probe sufficiently detects overwhelming majority of KLC1-mCherry signal. A) KLC1-mCherry transfected hippocampal axon. B) Anti-KLC1 staining. C) Merge. All images at 100X. Scale bar reads 10µm.

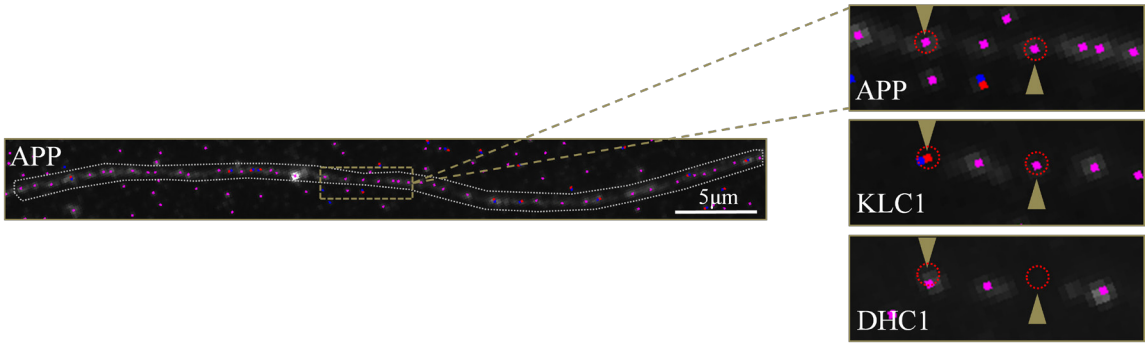


**Figure 3-5** Motor localization. Left panel shows detected APP features within an axon. Blue dots precisely map local maxima, red dots mark approximate position of Gaussian fits, and overlap of blue and red is shown in pink. Grey contour shows user defined region of interest (ROI), only capturing desired axonal features to be used for colocalization. Right panels depict an enlargement of all 3 channels, corresponding to anti-APP (anchor), anti-KLC1, and anti-DHC1 IF staining. Red circles define the 300nm cutoff for colocalization centered at the precise position of each APP Gaussian fitting. Beige arrows point to 2 separate APP detected vesicles, showing association with KLC1 only (right) or both KLC1 and DHC1 (left).

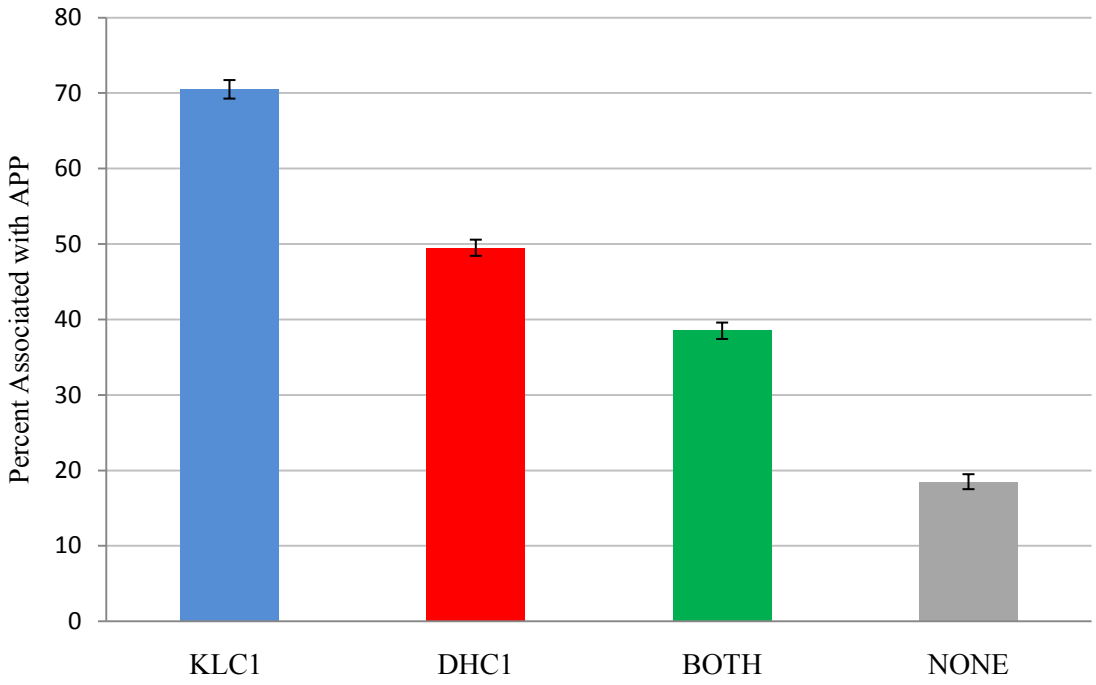


**Figure 3-6** Motor subunit composition of APP vesicles in control animals. The majority of APP vesicles are associated with a KLC1 subunit, about half with DHC1, and less than one out of five have neither subunit. Almost 40% of APP vesicles within hippocampal axons are associated with both types of motor proteins. $N_{Vesicles}$ = 4,050; $N_{Animals}$ = 6; $N_{Coverslips}$ = 11 ; $N_{Images}$ = 34. Percentages are averaged per image first then overall. Error bars show s.e.m.

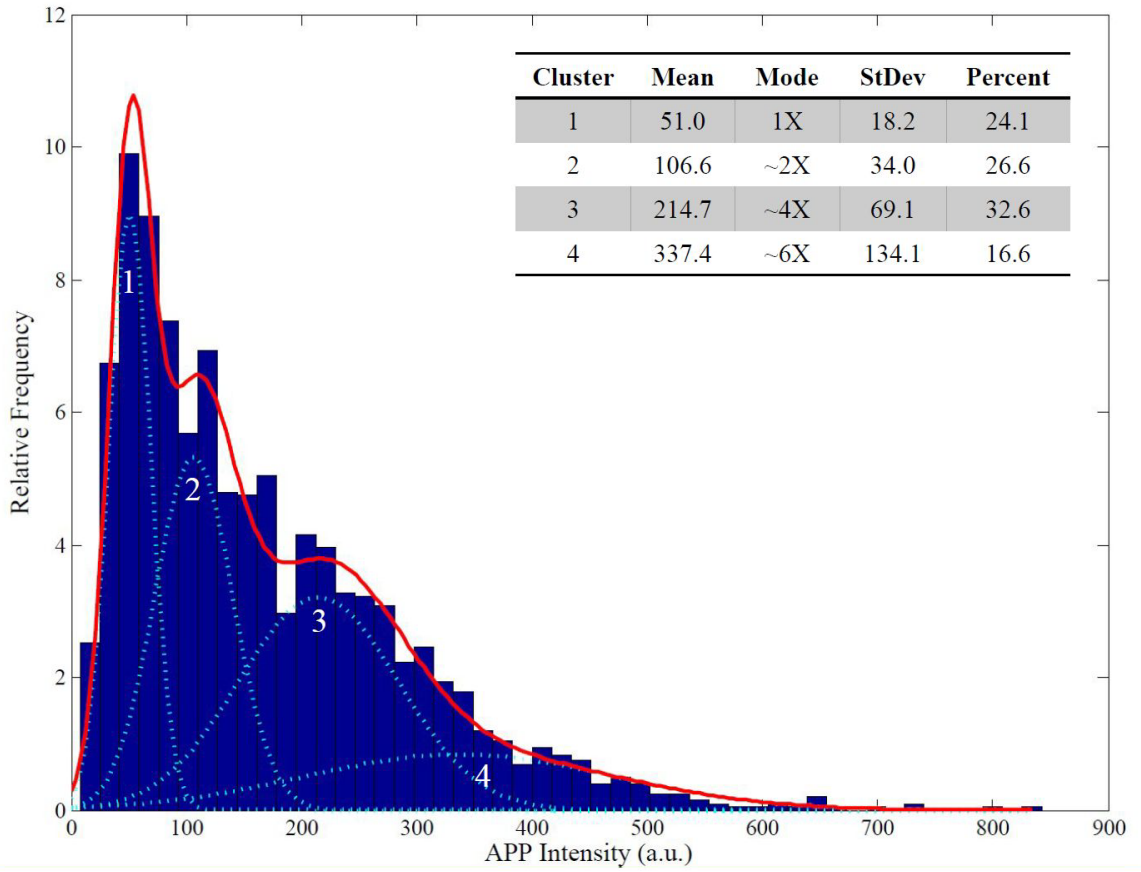


| Cluster | Mean | Mode | StDev | Percent |
|---|---|---|---|---|
| 1 | 51.0 | 1X | 18.2 | 24.1 |
| 2 | 106.6 | ~2X | 34.0 | 26.6 |
| 3 | 214.7 | ~4X | 69.1 | 32.6 |
| 4 | 337.4 | ~6X | 134.1 | 16.6 |

**Figure 3-7** A. Clustering the APP intensity profile in control animals. Model based clustering (mClust) followed by BIC is employed to determine optimal clustering of resulting intensity profiles and shows that APP intensities are best portrayed by a series of 4 normally-distributed clusters. The mean, mode relative to cluster 1, standard deviation, and percent of data described by each cluster is listed in the table. Data is presented for 1 complete dataset to avoid normalization variability during clustering. $N_{Vesicles}$ = 2,020; $N_{Animals}$ = 3; $N_{Coverslips}$ = 6; $N_{Images}$ = $N_{Axons}$ = 17.

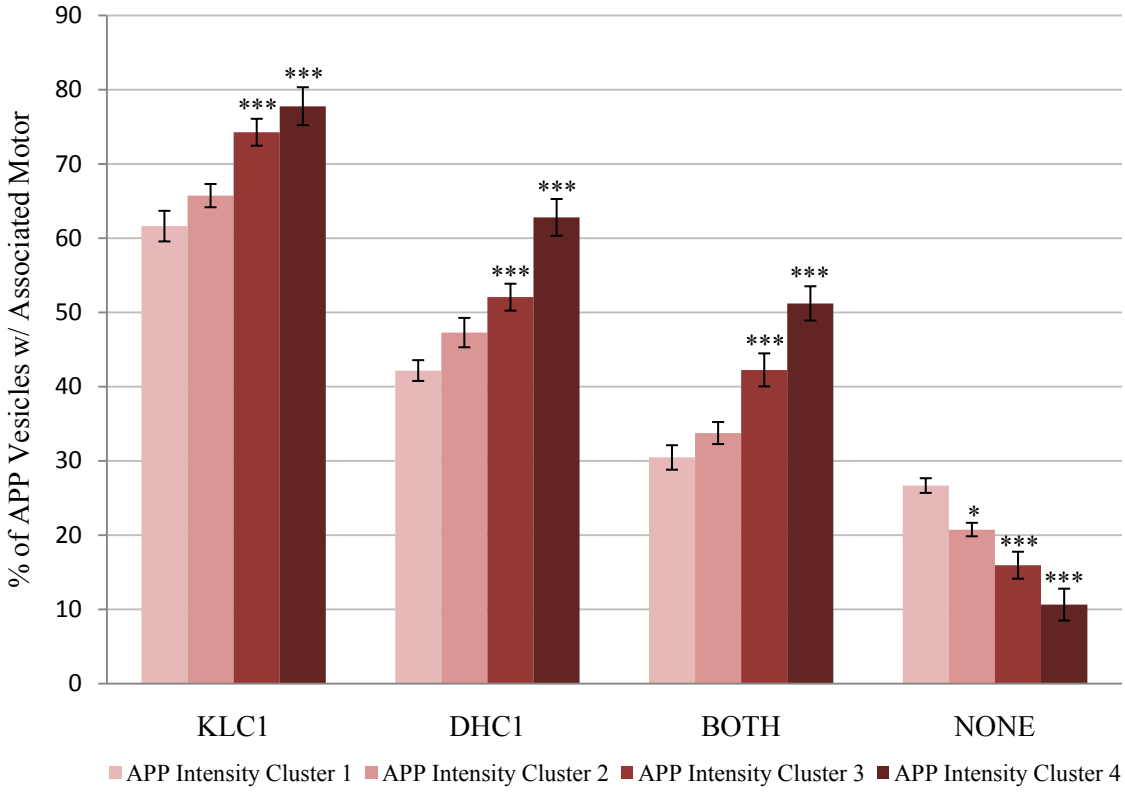


**Figure 3-7** B. Motor presence as a function of APP intensity. Percent motor subunit association significantly increase as a function of APP amount in vesicles. Cluster 1: $N_{APP}$ = 487; Cluster 2: $N_{APP}$ = 538; Cluster 3: $N_{APP}$ = 659; Cluster 4: $N_{APP}$ = 336; $N_{Vesicles}$ = 2,020; $N_{Animals}$ = 3; $N_{Coverslips}$ = 6 ; $N_{Images}$ = $N_{Axons}$ = 17.

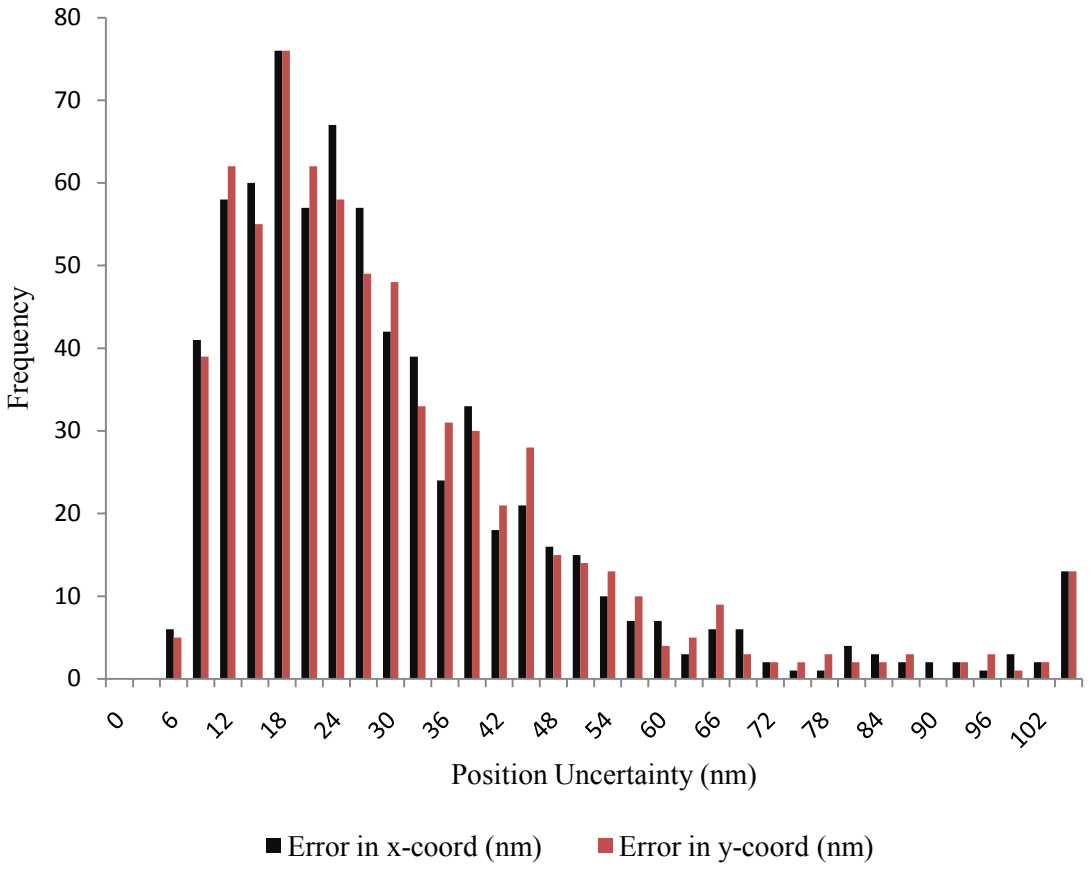


**Figure 3-8** Observed uncertainty in feature position estimation for APP in control animals. The mean position uncertainty in x- and y- is 29.6nm and 29.9nm respectively. 92.6% of the position data has an error of less than 60nm. $N_{Vesicles} = 705$. $N_{images} = N_{axons} = 6$.

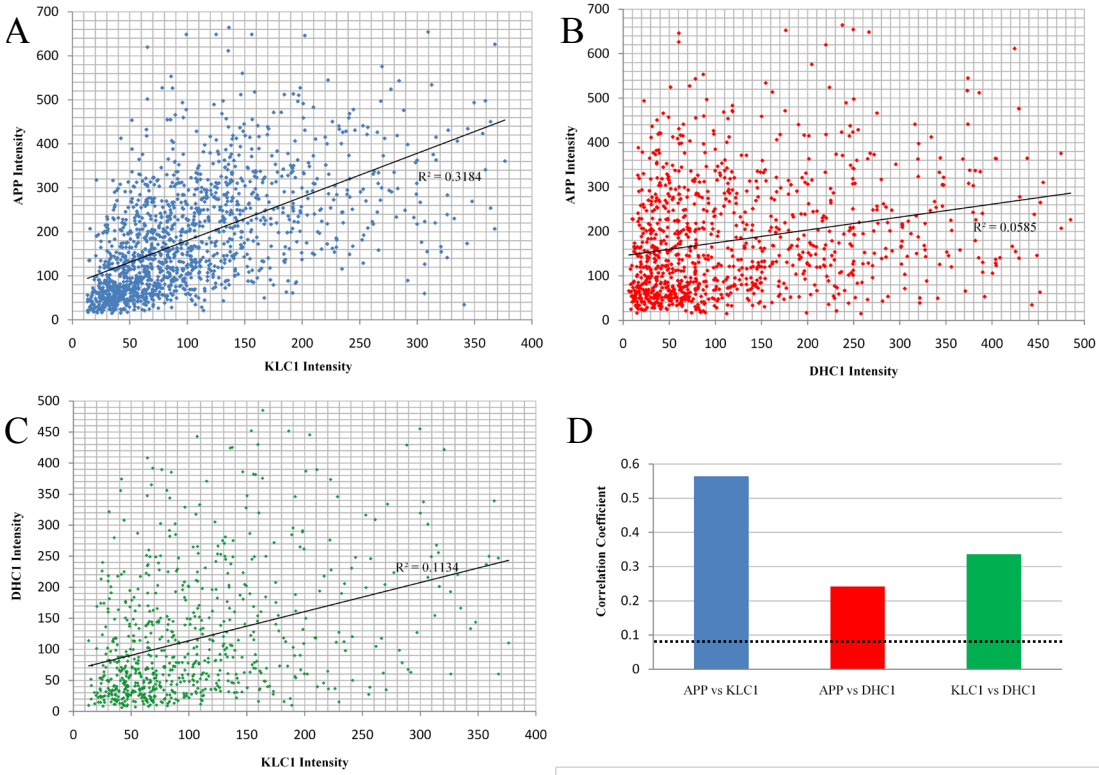


**Figure 3-9** Motor subunit Gaussian amplitude intensity comparisons. A) Scatter plot of KLC1 vs. APP for all APP associated KLC1 intensities. $N_{Vesicles}$ = 1,516 B) Scatter plot of DHC1 vs. APP for all APP associated DHC1 intensities. $N_{Vesicles}$ = 1,014 C) Scatter plot of KLC1 vs. DHC1 for all APP vesicles associated with both subunits. $N_{Vesicles}$ = 757 D) Coefficients of correlation for each pair of intensity measures listed above. The horizontal black line indicates the maximal (3σ) range of correlation coefficients under random pairings for each intensity comparison.

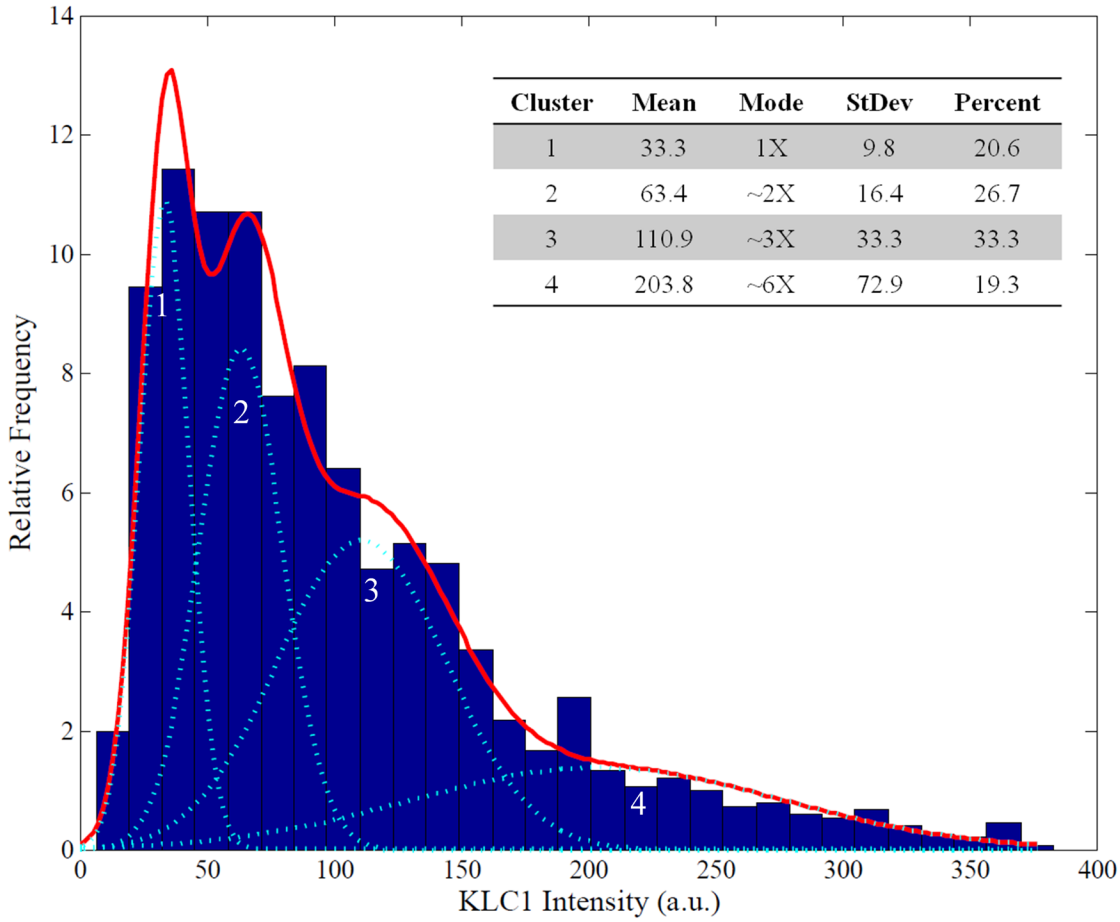


| Cluster | Mean | Mode | StDev | Percent |
|---|---|---|---|---|
| 1 | 33.3 | 1X | 9.8 | 20.6 |
| 2 | 63.4 | ~2X | 16.4 | 26.7 |
| 3 | 110.9 | ~3X | 33.3 | 33.3 |
| 4 | 203.8 | ~6X | 72.9 | 19.3 |

**Figure 3-10** A. KLC1 motor subunit intensity clustering. KLC1 intensities are best portrayed by a series of 4 normally-distributed clusters. The mean, mode relative to cluster 1, standard deviation, and percent of data described by each cluster is listed in the table. Data is presented for 1 complete dataset to avoid normalization variability during clustering. $N_{Vesicles}$ = 1,516; $N_{Animals}$ = 3; $N_{Coverslips}$ = 6; $N_{Images}$ = $N_{Axons}$ = 17.

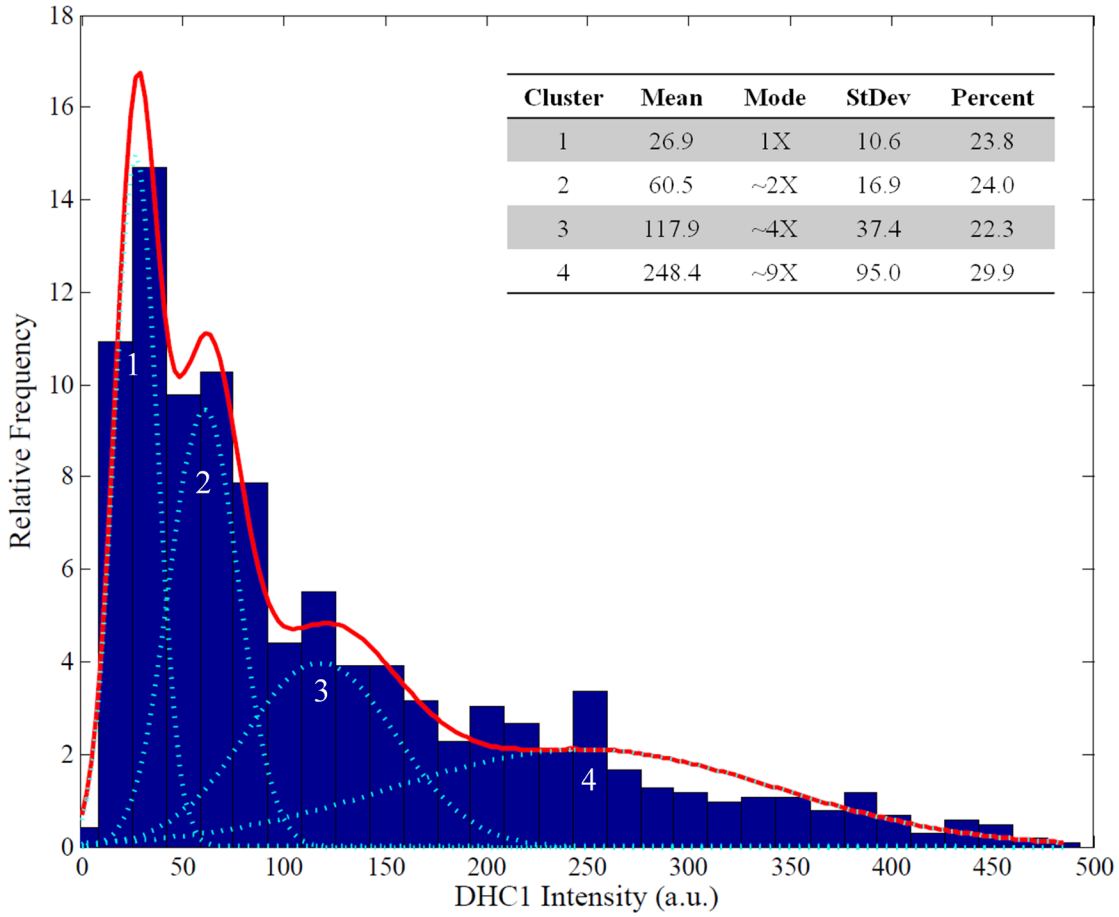


| Cluster | Mean | Mode | StDev | Percent |
|---|---|---|---|---|
| 1 | 26.9 | 1X | 10.6 | 23.8 |
| 2 | 60.5 | ~2X | 16.9 | 24.0 |
| 3 | 117.9 | ~4X | 37.4 | 22.3 |
| 4 | 248.4 | ~9X | 95.0 | 29.9 |

**Figure 3-10** B. DHC1 motor subunit intensity clustering. DHC1 intensities are best portrayed by a combination of 4 normally-distributed clusters. The mean, mode relative to cluster 1, standard deviation, and percent of data described by each cluster is listed in the associated table. Data is presented for 1 complete dataset to avoid normalization variability during clustering. $N_{Vesicles}$ = 1,014; $N_{Animals}$ = 3; $N_{Coverslips}$ = 6; $N_{Images}$ = $N_{Axons}$ = 17.

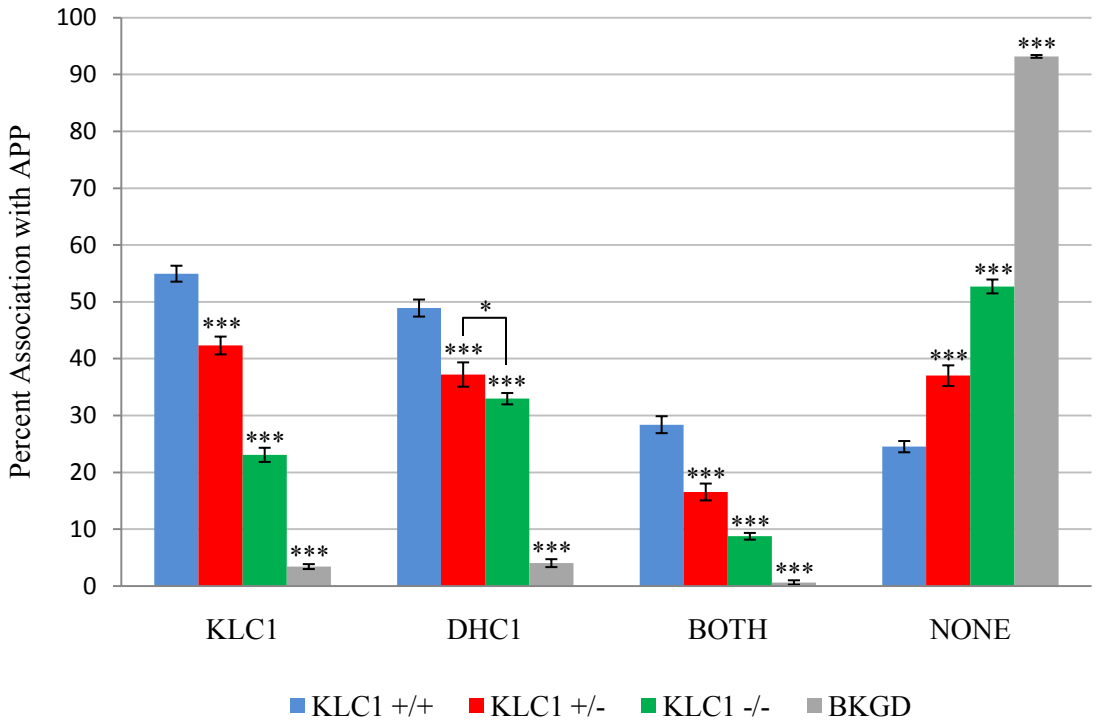


**Figure 3-11** Motor subunit composition of APP vesicles in KLC1 genotypes. As expected, we observe significant decreases in the amount of KLC1 associated within 300nm of a detected APP vesicle feature as KLC1 copy number is genetically reduced. Interestingly, we also report significant reductions of DHC1 subunit association as a function of KLC1 copy number. KLC1 +/+: $N_{Vesicles}$ = 1,676, $N_{Animals}$ = 4 $N_{Coverslips}$ = 10, $N_{images}$ = $N_{axons}$ = 20; KLC1 +/-: $N_{Vesicles}$ = 1,760, $N_{Animals}$ = 4 $N_{Coverslips}$ = 10, $N_{images}$ = $N_{axons}$ = 19; KLC1 -/-: $N_{Vesicles}$ = 1,569, $N_{Animals}$ = 3 $N_{Coverslips}$ = 10, $N_{images}$ = $N_{axons}$ = 17.

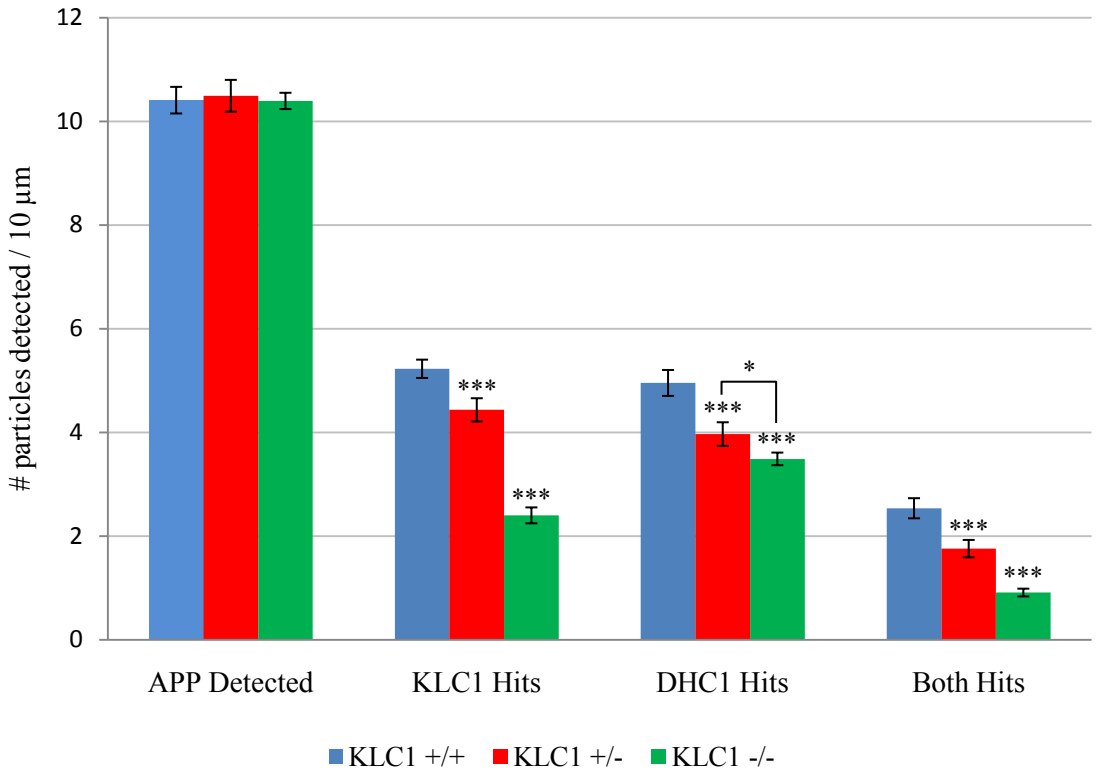


**Figure 3-12** Number of features detected per 10 µm in KLC1 genotypes. We report no differences in the number of APP vesicles detected between KLC1 genotypes. KLC1 +/+: $N_{Vesicles}$ = 1,676, $N_{Animals}$ = 4 $N_{Coverslips}$ = 10, $N_{images}$ = $N_{axons}$ = 20; KLC1 +/-: $N_{Vesicles}$ = 1,760, $N_{Animals}$ = 4 $N_{Coverslips}$ = 10, $N_{images}$ = $N_{axons}$ = 19; KLC1 -/-: $N_{Vesicles}$ = 1,569, $N_{Animals}$ = 3 $N_{Coverslips}$ = 10, $N_{images}$ = $N_{axons}$ = 17.

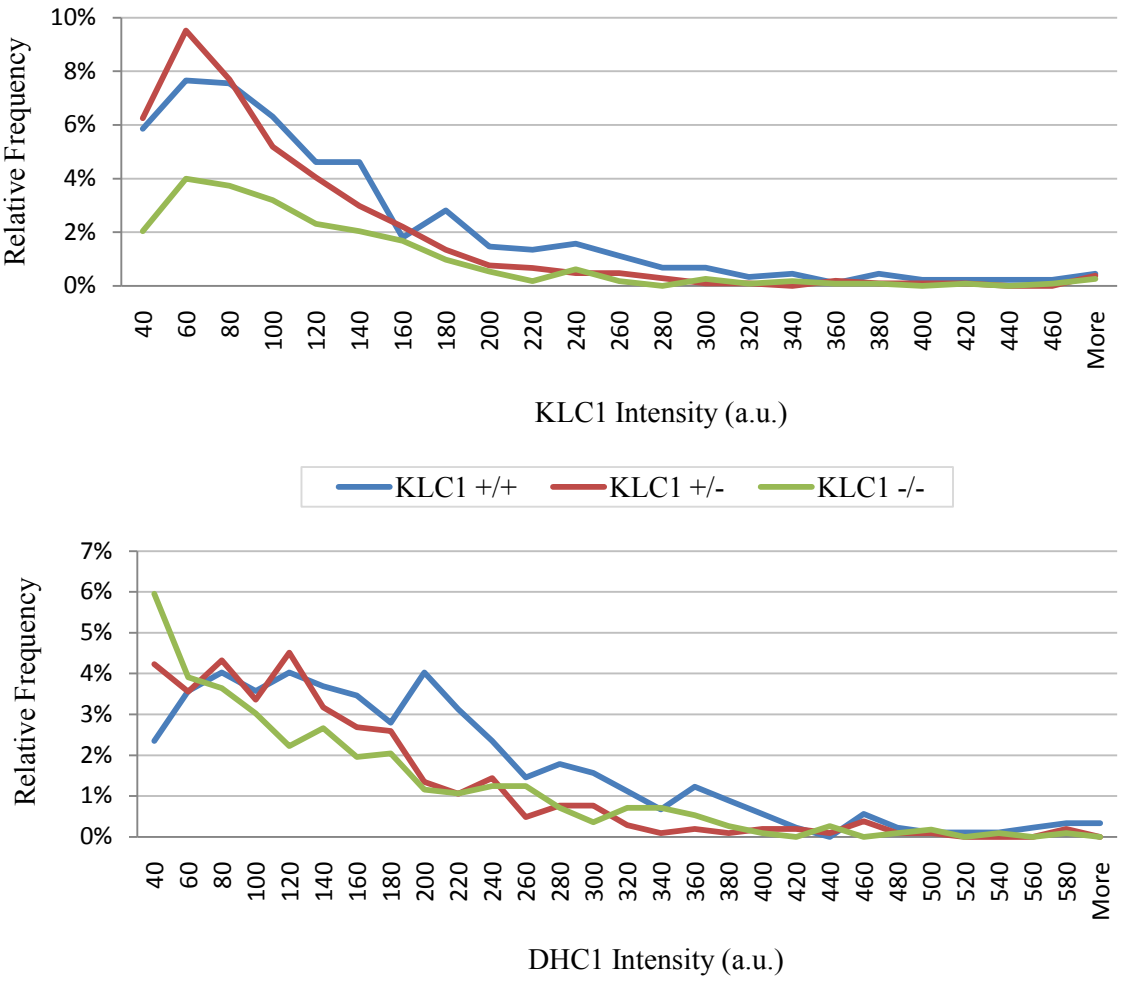


**Figure 3-13** Motor subunit Gaussian amplitude intensity distributions in KLC1 genotypes. See section 3.3.6 in text for discussion of results. KLC1 +/+: $N_{Vesicles} = 895$, $N_{Animals} = 2$ $N_{Coverslips} = 5$, $N_{images} = N_{axons} = 10$; KLC1 +/-: $N_{Vesicles} = 1{,}041$, $N_{Animals} = 2$ $N_{Coverslips} = 5$, $N_{images} = N_{axons} = 10$; KLC1 -/-: $N_{Vesicles} = 1{,}126$, $N_{Animals} = 2$ $N_{Coverslips} = 5$, $N_{images} = N_{axons} = 10$.

# 4 STABLE KINESIN AND DYNEIN ASSEMBLIES DRIVE THE AXONAL TRANSPORT OF MAMMALIAN PRION PROTEIN VESICLES


## Abstract

Kinesin and dynein are opposite-polarity microtubule motors that drive the tightly regulated transport of a variety of cargos. Both motors can bind to cargo but their overall composition on axonal vesicles and whether this composition directly modulates transport activity, is unknown. Here we characterize the intracellular transport and steady state motor subunit composition of mammalian prion protein ($PrP^C$) vesicles. We identify kinesin-1 and cytoplasmic dynein as major $PrP^C$ vesicle motor complexes, and show that their activities are tightly coupled. Regulation of normal retrograde transport by kinesin-1 is independent of dynein-vesicle attachment, and requires the vesicle association of a complete kinesin-1 heavy and light chain holoenzyme. Furthermore, motor subunits remain stably associated with stationary as well as with moving vesicles. Our data suggest a coordination model where $PrP^C$ vesicles maintain a stable population of associated motors whose activity is modulated by regulatory factors instead of by structural changes to motor-cargo associations.

## 4.1 Introduction

The viability and proper function of neurons depends on the active axonal transport of diverse cargos (Hirokawa and Takemura 2005; Goldstein, Wang et al. 2008; Verhey and Hammond 2009). The microtubule (MT)-based motors driving these movements are kinesin and cytoplasmic dynein, which use the energy of ATP hydrolysis to translocate along MT tracks in plus- (anterograde), and minus-end (retrograde) directions. Cytoplasmic dynein consists of a core processive dynein heavy chain (DHC) motor that interacts with a large assembly of accessory subunits and with dynactin, to drive most retrograde transport (Karki and Holzbaur 1999; Kardon and Vale 2009). Kinesin-1 is a heterotetramer consisting of a homodimer of one of three kinesin heavy chains (KHC; kinesin-1A, -1B, and -1C, formerly KIF5A, -B, and –C; (Xia, Rahman et al. 1998), that can interact in vitro with a homodimer of either of two accessory kinesin light chains (KLC1 and KLC2; Rahman et al., 1998). It is unknown what complexes of heavy and light chains form in vivo to drive the movement of any vesicular cargo studied to date (Rahman, Friedman et al. 1998; DeBoer, You et al. 2008).

Intracellular transport is often bidirectional, as cargos regularly reverse course en route to their final destinations. These dynamics have been observed for mitochondria, peroxisomes, melanosomes, endosomes, lipid droplets, synaptic vesicle precursors, and viral particles, where transport of opposite polarity motors is often coordinated (Sato-Yoshitake, Yorifuji et al. 1992; Plitz and Pfeffer 2001; Gross, Tuma et al. 2002; Welte 2004; Kural, Kim et al. 2005; Shubeita, Tran et al. 2008; Lyman and Enquist 2009; Soppina, Rai et al. 2009). An important question in transport regulation is how motor activity is controlled in cells to achieve bidirectionality. Because kinesin-1 and dynein are

uni-directional motors, coordination could occur either by the alternating association/dissociation of motors of either polarity to/from cargo, which generates motor activation by cargo-binding; by the modulation of activity of both types of motors that simultaneously bind to cargo; or by generation of opposing forces of simultaneously cargo-bound motors in a tug-or-war (TOW) (Gross 2004; Welte 2004). It has been proposed that motor regulation by association/dissociation might be a generalized mechanism of transport regulation, as motors can exist in inactive, un-bound forms, and autoinhibition can be released by binding to cargo (Verhey and Hammond 2009; Akhmanova and Hammer 2010). Alternatively, there is evidence that certain neuronal cargos in vitro or non-neuronal cargos in vivo experience opposing TOW forces such that the total number of motors associated with cargo determines activity (Soppina, Rai et al. 2009; Hendricks, Perlson et al. 2010). However, in coordination models of axonal transport, the extent of plus- and minus-end motor association with cargo, and whether cargo association relates to changes in motor activity, remains unclear. To test whether motor-cargo association modulates motor activity in axons and to build an in vivo model of bidirectional transport, it is imperative to characterize the steady-state composition of total motor assemblies on a single type of vesicular cargo, and relate this analysis to live movement data for the same cargo.

Analyzing motor composition of cargo in vivo has been experimentally challenging because of the difficulty in isolating populations of a *single* type of cargo, and the absence of quantitative methods to characterize motor composition on them. Biochemical purifications of heterogeneous membrane populations or of melanosomes have yielded estimates of co-fractionating plus- and minus-end motors (Gross, Tuma et

al. 2002; Hendricks, Perlson et al. 2010). However, these represent indirect estimates of average levels of bound motors, as motor-cargo associations could vary from cargo to cargo and over time. Likewise, stall-force measurements have provided estimates of numbers of active motors (Kural, Kim et al. 2005; Shubeita, Tran et al. 2008; Soppina, Rai et al. 2009), but it is unclear whether bidirectionality is dictated by the rapid association/dissociation of these active motors, or whether these engaged motors represent a subgroup of a regulated but stable assembly of cargo-bound motors. Thus, the steady-state composition of motor assemblies on any single type of cargo remains undefined.

To distinguish between regulatory versus association/dissociation models of bidirectional transport, we characterized the mechanism of axonal transport of vesicles containing the cellular mammalian prion protein ($PrP^C$). $PrP^C$ is a neuronally enriched glycosyl-phosphatidylinositol (GPI) anchored protein that follows the secretory pathway inside the lumen of vesicles toward the cell surface (Harris 2003; Caughey, Baron et al. 2009). $PrP^C$ can convert to a pathogenic form called PrP-scrapie ($PrP^{Sc}$), which has been implicated in neurological disorders including Creutzfeldt-Jakob disease in humans (Caughey et al., 2009). The function of $PrP^C$ is unclear, but evidence suggests that while at the cell surface it can interact with proteins involved in cell adhesion and signaling (Mouillet-Richard, Ermonval et al. 2000; Malaga-Trillo, Solis et al. 2009), as well as with $PrP^{Sc}$ (Caughey, Baron et al. 2009). Thus, trafficking of $PrP^C$ to the plasma membrane via an intact transport system might be relevant to $PrP^C$ function and for the initiation of neurodegenerative pathologies. While $PrP^C$ is transported in nerves (Rodolfo, Hassig et al. 1999; Moya, Hassig et al. 2004; Butowt, Abdelraheim et al. 2006), the mechanism of

intracellular $PrP^C$ vesicular transport is unknown. Here, we developed assays to characterize relative motor subunit composition on individual $PrP^C$ vesicles, and used live imaging to identify kinesin-1C/KLC1 and DHC1 as the major axonal motor complexes driving $PrP^C$ vesicle transport. Live tracking and motor composition analyses demonstrate that opposing motors positively coordinate each other's activities independently of cargo-association mechanisms. This coordination mechanism requires the formation and vesicle association of an intact kinesin-1 complex composed of heavy and light chains.

## Results

### 4.2.1 Mammalian $PrP^C$ vesicles move bidirectionally in hippocampal axons

Previous studies showed that mammalian and avian $PrP^C$ are transported along peripheral and central nervous system nerves in anterograde and retrograde directions (Borchelt, Koliatsos et al. 1994; Rodolfo, Hassig et al. 1999; Moya, Hassig et al. 2004; Butowt, Davies et al. 2007). We confirmed these observations using a protein accumulation paradigm in mouse sciatic nerves (supplementary information; (Encalada, Szpankowski et al. 2011).

To characterize the intracellular transport of $PrP^C$ vesicles in live neurons, we tracked individual moving vesicles in 10-day old cultured mouse hippocampal axons from neurons transfected with a YFP-$PrP^C$ fusion construct (Borchelt, Davis et al. 1996); Figures S1C-E). We restricted analyses to axons at day 10-post plating, which have a largely uniform microtubule polarity with plus-ends directed toward axonal termini and minus-ends toward cell bodies (Baas, Deitch et al. 1988). To quantify YFP-$PrP^C$ vesicular movement, we used a MATLAB based custom particle tracking software (LAPTrack; Reis et al., see Chapter 2), to generate a comprehensive data set of trajectories at a spatial and temporal resolution of 0.126 um, and 10Hz, respectively.

In wild-type neurons, YFP-$PrP^C$ vesicles moved in anterograde and retrograde directions, and a large percentage were stationary (Figs. 4-1A&B). The remaining vesicles reversed directions at a frequency of 0.027 switches/sec (± 0.004 switches/sec SEM). Vesicle trajectories were broken into segments, defined as uninterrupted periods of movement framed by pauses (see Appendix). Mean anterograde and retrograde segmental velocities were 0.85 mm/sec (± 0.036 mm/sec SEM), and 0.86 mm/sec (± 0.06

mm/sec SEM; Fig. 4-1C), respectively, similar to those reported for kinesin-1 and cytoplasmic dynein in vitro (Mazumdar, Mikami et al. 1996; Howard 2001). Analysis of segmental velocity distributions showed a wide range of anterograde and retrograde velocities that included maximal velocities of 2.8 mm/sec and 2.6 mm/sec, respectively (Fig. 4-1D). Retrograde particles had shorter mean run lengths (4.8 mm ± 0.4 mm SEM) than anterograde ones (6.2 mm ± 0.5 mm SEM), but paused as long and as frequently (Figs. 4- 1E-G). These run lengths were longer than the 1-2 mm reported for kinesin-1 and dynein in vitro (Thorn, Ubersax et al. 2000; King, Brown et al. 2003). Thus, vesicles containing YFP-$PrP^C$ move bidirectionally en route to the synapse in primary hippocampal neurons with dynamics that are consistent with MT-dependent fast axonal transport mediated by kinesin and dynein motor proteins.

### 4.2.2 Kinesin-1 and cytoplasmic dynein associate with $PrP^C$ vesicles in vivo

To understand the mechanism of axonal transport of $PrP^C$ vesicles, we sought to identify the motor proteins moving these vesicles in axons. Because $PrP^C$ and kinesin-1 are predominantly expressed in brain, we tested the hypothesis that kinesin-1 is a $PrP^C$ vesicle motor protein. We first tested whether the KLC1 cargo-binding subunit associated biochemically with $PrP^C$ vesicles in floated membrane fractions (Fig. 4-2A). Using an antibody against KLC1 to pull-down associated membrane components, we found that $PrP^C$ and KHC (as detected by an antibody that recognizes primarily kinesin-1C) immunoprecipitated with KLC1, as did the amyloid precursor protein (APP), previously identified in a complex with KLC1 ((Kamal, Stokin et al. 2000); Fig. 4-2B). Because $PrP^C$ is in the vesicular lumen, the reverse immunoprecipitation experiment using $PrP^C$ antibodies to pull-down KLC1 was not possible without breaking vesicular membranes.

To further test whether kinesin-1 subunits interact with $PrP^C$ vesicles, we imaged fixed hippocampal cell axons stained with antibodies against $PrP^C$, and KLC1, kinesin-1C or kinesin-1A. The fluorescent signal observed was punctate, suggesting that these proteins were localized to vesicular structures (Fig. 4-2C). We observed significant colocalization between $PrP^C$ and KLC1 (58% $PrP^C$ vesicles colocalized with KLC1 ± 1.5% SEM; $N_{vesicles}$=510), and $PrP^C$ and kinesin-1C (35% $PrP^C$ vesicles colocalized with kinesin-1C ± 1.5% SEM; $N_{vesicles}$ =80), but not between $PrP^C$ and kinesin-1A. Complete colocalization was not expected as kinesin-1 also mediates transport of other cargos, and because other kinesin motors might also transport $PrP^C$ vesicles in addition to kinesin-1.

To test whether cytoplasmic dynein transports $PrP^C$ vesicles, we quantified YFP-$PrP^C$ vesicle movement in hippocampal cells co-transfected with YFP-$PrP^C$ and with a short hairpin RNA (shRNA)-mCherry construct targeted to reduce the amount of dynein heavy chain 1 (DHC1; referred to as DHC1 shRNA). Imaging was restricted to axons co-expressing YFP and mCherry markers. Using the live imaging assay, we found that 2 days after co-transfection, reduction of DHC1 (mRNA reduced by 80-90%, protein reduced by 66%), disrupted bidirectional YFP-$PrP^C$ vesicle transport, decreasing run lengths and increasing the frequency of pauses (Figs. 4-2D&E). Mean segmental velocities remained unchanged. To confirm DHC1 association with $PrP^C$ vesicles, we stained hippocampal axons and found that DHC1 partially colocalized with $PrP^C$ vesicles (43% $PrP^C$ vesicles colocalized with DHC1 ± 2.9% SEM; $N_{vesicles}$= 388; Fig. 4-2C). Thus, KLC1, kinesin-1C, and DHC1, but not kinesin-1A, associate with $PrP^C$ vesicles in vivo. The interaction between kinesin-1 and $PrP^C$ is not a direct one, as immunoisolations from vesicular fractions using a KLC1 antibody in the presence of detergent did not pull down

$PrP^C$ (data not shown). Furthermore, disruptions of dynein inhibited bidirectional transport, indicating that dynein is required for normal retrograde movement, and is involved in the activation of the plus-end anterograde transport of these vesicles.

### 4.2.3 Kinesin-1 light chains mediate anterograde transport and activate retrograde movement of $PrP^C$ vesicles

Previous work showed that either of two KLCs can form complexes with any of the three KHCs (Rahman, Friedman et al. 1998). However, it is unknown what combinations of KLC and KHC subunits interact in vivo to transport any cargo. Having shown that KLC1 and kinesin-1C interact with $PrP^C$ vesicles, we next tested whether these physical interactions translated into functional transport requirements. Thus, we systematically reduced the function of each kinesin-1 subunit and assayed for defects in $PrP^C$ vesicle transport.

We tested KLC1 by analyzing YFP-$PrP^C$ vesicle transport in hippocampal cells from mice homozygous for a gene-targeted KLC1 deletion (referred to as KLC1 -/- neurons; (Rahman, Kamal et al. 1999). We tested KLC2 in wild-type hippocampal neurons co-transfected with YFP-$PrP^C$ and a KLC2 shRNA-mCherry construct, which reduced KLC2 by ~ 83% (referred to as KLC2 shRNA neurons). Reducing the function of each KLC subunit caused a significantly decreased percentage of anterograde-moving vesicles, and a higher frequency of stalled particles (Figs. 4-3A&B). Noticeably, the percentage of retrograde moving $PrP^C$ particles was also reduced in the absence of KLC1, suggesting that this subunit might be involved in promoting dynein-based movement. Observed and estimated run lengths were reduced in KLC1-/- and shRNA KLC2 axons, respectively (Figs. 4-3C&D), and vesicles paused more often (Fig. 4-3E). Given the

pronounced reductions of bidirectional movement, mean segmental velocities were surprisingly largely unaffected in KLC mutants, with the exception of slight increases in KLC1 -/- neurons contributed solely by the small number of reversing vesicles. Thus, KLC1 and KLC2 mediate anterograde transport of YFP-$PrP^C$ vesicles and also activate retrograde motility.

**4.2.4 Activation of bidirectional transport by a neuronal kinesin-1 heavy chain**

To test whether KHC is required for the transport of $PrP^C$ vesicles, we analyzed YFP-$PrP^C$ vesicle movement in hippocampal neurons from kinesin-1A -/-, and kinesin-1C -/- mice, and from conditional kinesin-1B mice (Cui, Wang et al. 2010). Conditional kinesin-1B neurons were treated post-plating with a cre-recombinase adenovirus at a multiplicity of infection (MOI) of 100 or 400, to remove kinesin-1B genomic DNA flanked by two loxP sites and to create functional null cells.

In kinesin-1C -/- axons, the proportion of anterograde moving $PrP^C$ vesicles declined, run lengths in both directions were significantly decreased, and these vesicles paused more frequently when moving in both directions (Figs. 4-4A-C). As was the case for DHC1 and KLC reduction, mean segmental velocities were unchanged (Fig. 4-4D). In kinesin-1B-cre axons, increasing adenoviral-cre MOI resulted in an increase in stationary vesicles (Fig. 4-4E). However, anterograde movement was either unchanged (pause frequencies; Fig. 4-4G), or activated as demonstrated by longer runs, and strikingly faster mean segmental velocities (Figs. 4-4F-H). While the basis for the enhanced mean velocities is uncertain, perhaps a faster kinesin-1C motor, which we showed above is required for normal YFP-$PrP^C$ anterograde motion, could be responsible for these increases. We did not observe major changes in YFP-$PrP^C$ transport in kinesin-1A -/-

axons, as only a minor decrease in retrograde run lengths and slight changes in segmental velocity distributions were observed (Figs. 4-4A-D&I; see next section). These results suggest that kinesin-1A, and -1B are not major components of the $PrP^C$ vesicular transport machinery, and are consistent with our immunofluorescence data that showed no significant colocalization between $PrP^C$ and kinesin-1A. We conclude that kinesin-1C is required for normal anterograde YFP-$PrP^C$ transport, and can act as an activator of retrograde movement. The requirements of both the neuronal-specific kinesin-1C and of DHC1 to activate each other's transport suggest that the activities of these motors are tightly coupled.

**4.2.5 Reduction of kinesin-1 does not affect global transport in axons**

To test whether transport defects caused by reducing kinesin-1 were specific to YFP-$PrP^C$ vesicles and not due to global disruptions of axonal transport, we characterized the movement of synaptophysin, a synaptic vesicle protein previously identified as a Kinesin-3 cargo (Okada, Yamazaki et al. 1995). We tracked the movement of synaptophysin-mCherry vesicles in hippocampal cultured cells following identical conditions as described above for YFF-$PrP^C$ vesicles. Reducing the function of any of the kinesin-1 subunits either did not change, or modestly stimulated bidirectional synaptophysin-mCherry transport, as observed by increased mean segmental velocities and reduced percentage of stationary vesicles. Thus, while kinesin-1 reduction alters transport dynamics of synaptophysin-mCherry vesicles, it is clearly not required for synaptophysin-mCherry transport.

### 4.2.6 Disrupting kinesin-1 or dynein decreases velocity distributions consistent with downregulation of motor activity

Reducing kinesin-1 or DHC1 results in bidirectional decreases in run lengths, and increases in pause frequencies, consistent with downregulation of opposing motor activity (Figs. 4-3 and 4-4). Surprisingly however, mean segmental velocity, a parameter also influenced by motor activity, was largely unaffected (Fig. 4-4D). Because possible redundancy among kinesin-1 subunits or incomplete removal of DHC1 might mask differences in average velocities, we analyzed segmental velocity distributions to test if these reflected reductions in opposing motor activity.

Wild-type anterograde and retrograde segmental velocity distributions were non-normal and showed a right-skewed bias (Fig. 4-1D). To analyze these distributions further, we performed cluster mode analysis by fitting non-normal distributions observed in wildtype and in kinesin-1 and DHC1 mutant axons, with predicted Gaussian modes using the mClust package in the R statistical computing environment (Fraley 1999). Optimal mode fits were generated by the Bayesian Information Criterion (BIC; see Appendix). In wildtype, three and two modes best fit the anterograde and retrograde distributions, respectively (Figs. 4-2F, 4-3F, and 4-4I). Strikingly, reduction of KLC1 or kinesin-1C reduced velocity distributions in both directions, suggesting that these two subunits pair to form the main holoenzyme that normally drives anterograde, and activates retrograde $PrP^C$ vesicle movement. Decreasing DHC1 also resulted in bidirectional shifts from higher to lower velocity modes and in a decreased number of modes (Fig. 4-2F). Notably, reducing kinesin-1A and -1B also slightly reduced a mode or the proportion of vesicles within higher anterograde modes (Fig. 4-4I), suggesting that

these motors might also play a role in the anterograde transport of $PrP^C$ vesicles, albeit a minor one since we did not observe major defects in other movement parameters. We conclude that segmental velocities represent a measure of the activity of motors, and that velocity distributions are reduced as a result of removal or decreases of opposite polarity motors, suggesting that regulation of motors can contribute to these activity changes.

### 4.2.7 Kinesin-1C is not required for the vesicle-association of DHC1 and KLC1

Our tracking data suggest that kinesin-1C and DHC1 activities are tightly coupled, since disruption of either inhibited opposite-polarity $PrP^C$ vesicle transport. Moreover, both KLC1 and kinesin-1C are required for normal retrograde motion. To investigate the role of kinesin-1 in bidirectional motion, we tested whether reduction of retrograde activity following removal of kinesin-1C was the result of the dissociation of the primary retrograde motor DHC1, from $PrP^C$ vesicles. We also tested whether KLC1 association with vesicles is needed for normal retrograde motion. We developed a robust imaging method to quantify association of motor subunits on individual endogenous $PrP^C$ vesicles of hippocampal axons in the presence or absence of kinesin-1C. Wild-type and kinesin-1C -/- neurons were fixed and stained with antibodies against $PrP^C$, DHC1, and KLC1 (Fig. 4-5A), and immunofluorescence images of diffraction limited $PrP^C$, DHC1, and KLC1 vesicle point sources were fitted with 2D Gaussians to estimate their point spread function, and to precisely map their coordinates and intensity amplitudes (Jaqaman, Loerke et al. 2008). A custom-built 'motor colocalization' algorithm quantified presence or absence and intensity amplitudes of each detected DHC1 and/or KLC1 puncta within 300nm of each $PrP^C$ vesicle (L.S., S.E.E. et al.; see Chapter 3).

DHC1 and KLC1 antibody specificities were evaluated as described (see Chapter 3 Methods).

We designated four $PrP^C$ vesicle categories, those that had only DHC1, only KLC1, both motor subunits, or no motor subunits associated with them (Fig. 4-5B). We found that in wild-type axons, 43% of $PrP^C$ vesicles colocalized with DHC1 (± 2.9% SEM), 57% of $PrP^C$ vesicles associated with KLC1 (± 1.5% SEM), and 25% of $PrP^C$ vesicles had both motor subunits (± 1.5% SEM). We did not detect motor subunits on 23% of $PrP^C$ vesicles (± 1.8% SEM). Removing kinesin-1C resulted in almost identical DHC1- and KLC1-associated $PrP^C$ vesicle pools (Fig. 4-5B). In addition, relative amounts of $PrP^C$ vesicle-associated DHC1 and KLC1, as measured by intensity distributions, were very similar between wild-type and kinesin-1C -/- axons (permutation t-test $p = 0.04$, and $p = 0.0681$ for DHC1 and KLC1 comparisons, respectively; Figs. 4-5C and 4-5D). Thus, while the DHC1 intensity distribution was borderline significantly different in kinesin-1C-/- axons as compared to wildtype, DHC1 certainly did not appear to dissociate from $PrP^C$ vesicles. We conclude that kinesin-1C is not required for DHC1 or KLC1 association with $PrP^C$ vesicles. Thus, impairment of retrograde movement observed after removing kinesin-1C is likely a result of coordination between kinesin-1C and DHC1 activities, rather than by altering DHC1-vesicle associations. Furthermore, because our tracking data show that retrograde movement is reduced after removal of KLC1 or kinesin-1C, but removal of kinesin-1C did not change the association of KLC1 with vesicles, we conclude that KLC1 is necessary but not sufficient to activate normal retrograde transport of $PrP^C$ vesicles. Thus, in the absence of KLC1 or kinesin-1C, retrograde movement is impaired suggesting that maximal activation of retrograde

motion requires the formation and association of a complete KLC1-kinesin-1C holoenzyme with $PrP^C$ vesicles. It is possible that redundancy with KLC2 and kinesin-1A or kinesin-1B might stimulate residual retrograde motion still observed in KLC1 and kinesin-1C mutant axons.

### 4.2.8 $PrP^C$ vesicles associate with heterogeneous but stable motor subunit assemblies

To further confirm the presence of stable motor assemblies on $PrP^C$ vesicles, and characterize the nature of this motor composition, we asked whether motor subunits of both polarities were distributed evenly and stably on these vesicles. The non-normal distributions of wild-type KLC1 and DHC1 intensity amplitudes detected on $PrP^C$ vesicles were mode-fitted and selected using mClust and BIC (Figs. 4-5E&F). The predicted modes on each KLC1 and DHC1 distributions showed three peaks corresponding to 1X, 2X, and 3X increments of intensities. Because the fluorescent intensity distribution of single molecules has a single Gaussian peak (Sugiyama, Kawabata et al. 2005), and the intensity of fluorescently labeled proteins has been shown to increase with increasing molecule concentration (Dixit, Ross et al. 2008), the multiple predicted modes in our data suggest the presence of a heterogeneous population of $PrP^C$ vesicles associated with 1X, 2X and 3X multiples of KLC1 or DHC1 motor subunits. We also tested that the KLC1 and DHC1 antibody signals scaled linearly with copy number, and were in linear range. The KLC1 and DHC1 quantal intensity modes did not change after removal of kinesin-1C (Figs. 4-5E&F), indicating that a stable motor subunit population on vesicles is not affected by the presence or absence of other motors.

To further assess the distribution of motor subunits on vesicles, we divided $PrP^C$ vesicles into those associated with a single motor subunit (either KLC1 or DHC1), or

with both, and quantified their intensity distributions and the percentage of vesicles within each predicted mode. When $PrP^C$ vesicles were associated only with KLC1, vesicles were distributed evenly in each of the 1X, 2X, and 3X motor subunit number modes (Fig. 4-5G), while the majority of $PrP^C$ vesicles associated only with 1X DHC1. No changes to these distributions were observed when both KLC1 and DHC1 were associated simultaneously with vesicles or when kinesin-1C was removed, suggesting that presence of KLC1 on the vesicle did not influence the association of DHC1 and vice versa (Fig. 5H). We conclude that the population of endogenous $PrP^C$ vesicles in axons is heterogeneous, having vesicles with overall associated motor subunit amounts in quantal multiples of 1X, 2X, 3X. However, this composition remained stable, and the presence of motor subunits on vesicles did not affect the binding of other subunits.

### 4.2.9 Motor subunits are associated with stationary and moving $PrP^C$ vesicles

Many cargo-bound proteins and organelles stop and function at specified axonal micro-domains. Thus, mitochondria are largely stationary in axons at sites where there is a high demand for ATP (Kang, Tian et al. 2008). While stoppage can be achieved via changes in external factors such as $Ca^{2+}$ levels or via interaction with docking adaptors (Kang, Tian et al. 2008), it is unknown whether a motionless state is achieved via dissociation of motors from cargo. Our system afforded us the opportunity to test this hypothesis because while $PrP^C$ vesicles move robustly in both directions, the majority are stationary (~70%; Fig. 4-1B). To ask whether motor subunits are differently associated with *individual* stationary versus moving vesicles in vivo, we developed a 'vesicle mapping' technique to characterize relative amounts of KLC1 and DHC1 on YFP-$PrP^C$ vesicles following recording of their individual live motion (see Methods). Hippocampal

cells were plated in microfluidic chambers to promote the growth of straight axons, and were transfected with YFP-$PrP^C$ (Taylor, Blurton-Jones et al. 2005); Fig. 4-6A). Movement of vesicles was imaged and cells were fixed with paraformaldehyde for subsequent staining with KLC1 and DHC1 antibodies, but the trajectories of vesicles pre- and post-fixation were recorded (Fig. 4-6B). Fixed images were superimposed to live movement kymographs to map (colocalize) fixed vesicles to their trajectories, after obtaining their precise Gaussian position coordinates and intensity amplitudes (Fig. 4-6B). The advantage of this method is that we are able to assess motor subunit composition on vesicles for which we have recorded individual vesicular trajectories (anterograde, retrograde, or stationary).

Our data revealed that both KLC1 and DHC1 associated with stationary as well as moving vesicles (Fig. 4-6C). Interestingly, we observed a correlation between KLC1 and DHC1 motor association on stationary vesicles, suggesting simultaneous increasing association of KLC1 and DHC1 (Fig. 4-6D). Our data show motor subunits associate to vesicles regardless of whether they were moving or not, indicating that motor subunit association is necessary but not sufficient for active translocation along microtubules.

## 4.3 Discussion

We identified kinesin-1C and DHC1 as major anterograde and retrograde motors required to transport $PrP^C$ vesicles in mammalian axons, and showed that they reciprocally promote their activity independently of motor-association mechanisms. We developed an assay to robustly assess the relative amounts of motors on vesicular cargo, and thus provided the characterization of motor composition in vivo on a single type of vesicle. We report that $PrP^C$ vesicles have a stable complement of motor subunits regardless of changes in motor activity suggesting that regulation of activity, and not motor-vesicle attachment, determines directionality.

### 4.3.1 Differential requirements of kinesin-1 subunits in $PrP^C$ vesicle transport

Previous studies showed that $PrP^C$ moved in anterograde and retrograde directions in nerves, but the mechanism of intracellular movement was unknown (Borchelt, Koliatsos et al. 1994; Rodolfo, Hassig et al. 1999; Moya, Hassig et al. 2004; Butowt, Abdelraheim et al. 2006). Using a combination of genetic, live imaging, biochemical, and immunofluorescence approaches, we dissected the requirements of each kinesin-1 subunit and of dynein, and identified kinesin-1C and DHC1 as the main plus- and minus-end motors, respectively, with a minor role attributed to kinesin-1A and kinesin-1B. Reduction of any one KHC did not result in complete disruption of anterograde transport, suggesting either some redundancy, or the requirement of another as yet unidentified motor. Interestingly, kinesin-1C mRNA expression was upregulated in kinesin-1B null extraembryonic membranes, pointing to a possible redundant function between these KHCs (Tanaka, Kanai et al. 1998). Whether higher transcript levels result in increased vesicle association of kinesin-1C in kinesin-1B -/- cells is unknown.

Our data also provide evidence for a role of KLC1 and KLC2 in $PrP^C$ vesicle transport. KLCs have been implicated in cargo-binding and transport regulation through their binding to KHCs, but are not always required. Mitochondria for example, are transported by KHC and a complex formed by Milton and Miro, but lack KLC association (Glater, Megeath et al. 2006). For $PrP^C$ vesicles, redundancy between KLC1 and KLC2 is likely, as disruption of either KLC did not result in complete blockage of transport. We tested this by combining velocity distributions after reducing each KLC, and observing the partial reconstitution of the wild-type anterograde distribution but not the retrograde one (Fig. 4-3G). Our data further point toward the pairing of neuronally enriched KLC1 and kinesin-1C as a primary $PrP^C$ vesicle transport complex: vesicle immunoisolations with KLC1 brought down kinesin-1C, and disrupting either of these motor subunits resulted in almost identical bidirectional phenotypes, more severe than seen with other subunits, including the decrease in bidirectional velocity distributions. Thus, our work establishes KLC1, KLC2, kinesin-1C and DHC1 as main motor subunits for $PrP^C$ vesicle transport. These requirements appear specific, as movement of synaptophysin vesicles is not inhibited following their disruption. Differential use of kinesin-1 components might be important for the selective targeting of different types of $PrP^C$ vesicles to distinct axonal domains. Whether the subunits are used in different cellular contexts is unknown, and functional experiments to address this issue for $PrP^C$ vesicles still need to be performed.

### 4.3.2 Uncoupling motor-association from motor-activation mechanisms to drive bidirectional transport

To characterize transport mechanisms we assessed $PrP^C$ vesicle movement by live

imaging, as well as motor-vesicle associations using immunofluorescence assays. Our data support the hypothesis that the total composition of motor subunits on $PrP^C$ vesicles is constant even when pronounced changes in motor activity are detected. Activity changes were revealed after impairing kinesin-1 and DHC1, which resulted in $PrP^C$ vesicles that traveled shorter distances, paused more frequently, and had altered velocity distributions (Figs. 4-3 and 4-4). The lower distribution of velocities observed here are in contrast to at least one in vivo study on *Drosophila* embryo lipid droplets that showed that average velocities were slightly higher following reductions in anterograde motor copy number (Shubeita, Tran et al. 2008). While inherent differences between *Drosophila* lipid droplets versus axonal transport systems might explain the contrasting observations, it is also possible that mean velocities might not reveal differences that can be detected only in analyses of velocity distributions. Indeed, mean velocities were generally unaffected after reduction of motors in our system (Fig. 4-4D).

Are the changes in observed motor activity directly correlated to the amount and composition of motors associated to those vesicles? Previous in vitro studies estimated the number of cargo-bound motors and suggested that these directly correlate to level of movement activity during TOW (Shubeita, Tran et al. 2008; Soppina, Rai et al. 2009; Hendricks, Perlson et al. 2010). However, during in vivo axonal transport of cargos undergoing regulatory coordination, although cargos can be moved by multiple motors, it is unclear whether all motors associated with cargo are active. Our data show that in axons in vivo, removing or reducing a motor reduces parameters of opposite-polarity transport, thus providing support for regulatory motor coordination, and against simple TOW scenarios. In this regulatory coordination setting, we show that a stable motor

subunit complement associates with $PrP^C$ vesicles regardless of their activity level or directionality. A combination of motor-interactions and regulatory coordination could be at play in vivo, as motors of opposite-polarities can mechanically interact to influence their motility (Ally, Larson et al. 2009). Thus, the mechanism of motor activity regulation in axons in vivo appears to be uncoupled from the one that regulates motor-vesicle associations. Consistent with this stable motor association model, previous work showed that kinesin-2 and dynein levels from purified melanosomes did not change during directionality switches, although these were bulk estimates and therefore it was unclear whether motor levels were unchanged on a per cargo basis (Gross, Tuma et al. 2002).

We thus propose a coordination model in which a stable population of kinesin-1 subunits and DHC1 associate with $PrP^C$ vesicles and a subset of these activate bidirectional movement, while the rest remain vesicle-bound but inactive (Fig. 4-7A). Stationary states are likely achieved by regulatory inhibition of bound motors. Thus, this model does not support cargo-binding as the sole mechanism of motor activation (Akhmanova and Hammer 2010). Indeed, in vitro work has shown that inactive motors can bind cargo and diffuse along the MT lattice (Lu, Ali et al. 2009). The ability of inactive motors to remain vesicle-bound could allow them to be activated "on the spot" according to cues specific to the cargo being transported.

### 4.3.3 Coordination of bidirectional transport in axons

Our data show that coordination of retrograde activity by kinesin-1C is independent of DHC1-vesicle association, but involves the simultaneous attachment of both types of motors to vesicles (Fig. 4-5B). Kinesin-1C thus appears to perform a dual function as a mediator of anterograde movement, and as an activator of retrograde

transport, but is not required for cargo binding by dynein. How might this retrograde activation occur? Our data suggest that it does so by the formation and vesicle association of an intact kinesin-1C/KLC1 complex, which is required for proper retrograde activity. The absence of either kinesin-1C or KLC1 precludes normal retrograde activation (Fig. 4-7B). However, KLC1 remains vesicle associated in kinesin-1C mutants, so its presence alone is not sufficient to activate normal retrograde motion. Likewise, kinesin-1C is decreased but still present in KLC1 -/- cells (Rhiannon Killian, personal communication), suggesting that this KHC subunit alone cannot induce normal retrograde activity. It is possible that kinesin-1C can bind to KLC2 in KLC1 -/- axons, as our data shows KLC2 is also required for normal levels of bidirectional movement, and is likely responsible for the residual retrograde motion observed. However, such a putative interaction is clearly not sufficient to rescue normal retrograde transport. A possible outcome of requiring a complete vesicle-bound kinesin-1 complex is that it could facilitate rapid activation and/or autoinhibition, which has been shown to occur via KLC with KHC interactions (Verhey, Lizotte et al. 1998; Cai, Hoppe et al. 2007). Changes in kinesin-1 autoregulation could translate to changes in dynein activity. Thus, our data is consistent with a model for bidirectional coordination in which activities of kinesin-1 and dynein might be linked via physical contacts (Martin, Iyadurai et al. 1999), and points to a role of KLCs in this linkage. Whether contact occurs via KLC interactions with dynein accessory subunits, dynactin, and/or other unidentified components has been suggested but is unclear (Martin, Iyadurai et al. 1999; Ligon, Tokito et al. 2004). Alternatively, direct motor-motor interactions could coordinate movement, as mechanical pulling of plus- and minus-end motors against each other has been suggested to be necessary and sufficient to

activate opposing motor activity (Ally, Larson et al. 2009). In the case of $PrP^C$ vesicles, coordination of a stable population of simultaneously bound motors is likely to be important for their efficient transport and delivery to various axonal regions or to the cell surface, where $PrP^C$ has been implicated in signal transduction and cell adhesion (Mouillet-Richard, Ermonval et al. 2000; Malaga-Trillo, Solis et al. 2009). This mechanism might also be a strategy for efficient distribution of many other cargos along axons, with stable complexes of motors loading onto vesicles presumably at or near the cell body, where motors are produced. Stable associations would allow differential regulation and coordination of subsets of motors, either by themselves or by factors specific to the vesicular cargo.

## Methods

### Mice and cell culture

Mice used throughout this study were in the C57/Bl6 background. KLC1, kinesin-1A -/-, and conditional kinesin-1B mice were described previously (Rahman, Kamal et al. 1999; Xia, Roberts et al. 2003; Cui, Wang et al. 2010). Generation of kinesin-1C -/- mice is detailed in Supplemental Experimental Procedures. Hippocampal cultures were plated from either E15-E18 or 1 day old pups (Falzone, Stokin et al. 2009).

### Transfection and adenovirus cre-recombinase transduction

Transfections of hippocampal neurons were done 10 days post-plating following a standard Lipofectamine 2000 protocol (Invitrogen). Cells were imaged or fixed 18-24 hours later. Plated hippocampal cells from conditional homozygous kinesin-1B II/II mice were treated 10 days post-plating with 0, 100 or 400 MOI adenovirus cre-recombinase (Ad5CMVCre from the University of Iowa, Gene Transfer Vector Core), corresponding to 0, 1.1e-7, and 4.4e-7 plaque forming units (PFU), respectively.

### Vesicle immunoisolation

Vesicle immunoisolations were performed with antibodies against KLC1 or GFP to pull-down vesicular membrane components obtained from floated membrane fractions (Supplemental Experimental Procedures).

### Immunofluorescence and microscopy

Hippocampal neurons and N2a cells were fixed with 4% paraformaldehyde, permeabilized, and stained with antibodies against KLC1 and DHC1. Fixed immunofluorescence images were taken on a Deltavision RT deconvolution system, and live images were taken with a Nikon Eclipse TE2000-U inverted microscope.

**Live imaging microscopy, motor colocalization, and vesicle mapping**

Live imaging of YFP-$PrP^C$, synaptophysin-mCherry, or synaptophysin-YFP was done on 10 or 11-day old hippocampal neuron axons, within 24 hours after transfection. Transfection rates were ~3%, which facilitated imaging of single axons. Plates were maintained at 37˚C and in a 5.5% $CO_2$ environment throughout the imaging period, for a maximum of 40 minutes. Images were taken exclusively from axons and we distinguished axons from dendrites by morphology. Axons are thinner and uniform in diameter, are longer, have fewer branches, and exhibit prominent growth cones (Baas, Deitch et al. 1988; Baas, Black et al. 1989). Axons were traced from termini to cell body and imaged within a region >180 um from either end. Live images were taken with a Nikon Eclipse TE2000-U inverted microscope equipped with a Coolsnap HQ camera (Roper Scientific) and a 100X/1.4 NA oil objective. Movies were 15 seconds long and collected at 10 frames per second at 100ms exposure (10Hz), at a resolution of 0.126um using Metamorph stream acquisition software (MDS Analytical Technologies).

For motor colocalization studies (also see Chapter 3 Methods), cells were fixed with 4% paraformaldehyde plus 4% glucose, for 30 minutes at 37˚C and in a 5.5% $CO_2$. Cells were incubated for 5 minutes at room temperature with 0.1% triton X-100 (TX-100) for permeabilization, and followed by a 45 minute incubation in block consisting of 10% donkey serum, 3% BSA, 0.1% TX-100 in PBS. Images of fixed wild-type and Kinesin-1C -/- hippocampal cells stained with antibodies against $PrP^C$, KLC1 and DHC1 were taken on the same day and under the exact exposure conditions for each experimental condition. Fixed immunofluorescence images were taken on a Deltavision RT deconvolution system mounted on an Olympus IX70 inverted microscope equipped with

a mercury lamp, with bandpass excitation and emission filters for FITC, Rhodamine and Cy-5 and a 100X objective/1.4 NA PlanApo. Images of 0.5 mm TetraSpeck fluorescent microspheres (Invitrogen), which were used to calibrate the X-Y-Z alignment of the microscope to account for spherical and chromatic aberration of the fluorescent channels, were also collected on the same day. For some colocalization analyses, fluorescent intensity calibration between experiments was done using 2.5 mm green, red, and deep red 0.3% relative intensity fluorescent microspheres from an InSpeck Microscope Image Intensity Calibration Kit (Invitrogen).

For vesicle mapping analyses, hippocampal neurons (~275,000) were plated in microfluidic chambers as described previously (Taylor, Blurton-Jones et al. 2005). Movies of intracellular YFP-$PrP^C$ movement from transfected cells were taken as described above, from axonal regions inside microchannels. While live imaging, culture media was removed from chambers and replaced with 4% paraformaldehyde to fix neurons and stain with KLC1 and DHC1 antibodies. Images of YFP-$PrP^C$, KLC1 and DHC1 channels from fixed axons were taken from the exact location where live movies were acquired, and these images were subsequently mapped back onto kymographs of the live YFP-$PrP^C$ movement using Adobe Photoshop. Individually mapped YFP-$PrP^C$ vesicles were classified according to transport class (anterograde, retrograde or stationary), and were fitted with Gaussians. The X-Y coordinates of each mapped $PrP^C$ vesicle were used to determine co-localization with KLC1 and/or DHC1 Gaussian-fitted point sources. The combination of live and fixed analyses was used because simultaneous live visualization of motor and vesicle movement via co-expression of fluorescent tags

attached to motors is challenging due to the overwhelming signal of presumably inactive soluble motors that results in a non-localized cytoplasmic fluorescence.

**Data and statistical analysis**

Trajectories of individual YFP-$PrP^C$ or synaptophysin-mCherry vesicles (i.e. tracks) were detected using a custom-made semi-automated particle tracking software written in MATLAB (Mathworks) and C++ (see Chapter 2). Definitions and calculations for each parameter are detailed in the Appendix.

'Motor colocalization' and 'vesicle mapping' analyses are detailed above. All tracking parameters reported herein were first tested for normality using the Lilliefors test implemented in the *nortest* package of R. Most parameters were not normally distributed so a non-parametric permutation t-test was used for comparison between genotypes (Moore and McCabe 2005). Differences in medians were also compared between genotypes for all parameters using the Wilcoxon-Mann-Whitney rank-sum test.

* Additional descriptions of methods can be found in the supplementary information associated with the published manuscript (Encalada, Szpankowski et al. 2011).

Chapter 4, in part, is a reprint of the following published manuscript. Encalada, S.E., L. Szpankowski, C. Xia, L.S.B. Goldstein. (2011). "Stable Kinesin and Dynein Assemblies Drive the Axonal Transport of Mammalian Prion Protein Vesicles." *Cell* 144(4): 551-565. The dissertation author was the secondary investigator and author of this paper and co-led the development, implementation, and analysis of the quantitative immunofluorescence method.

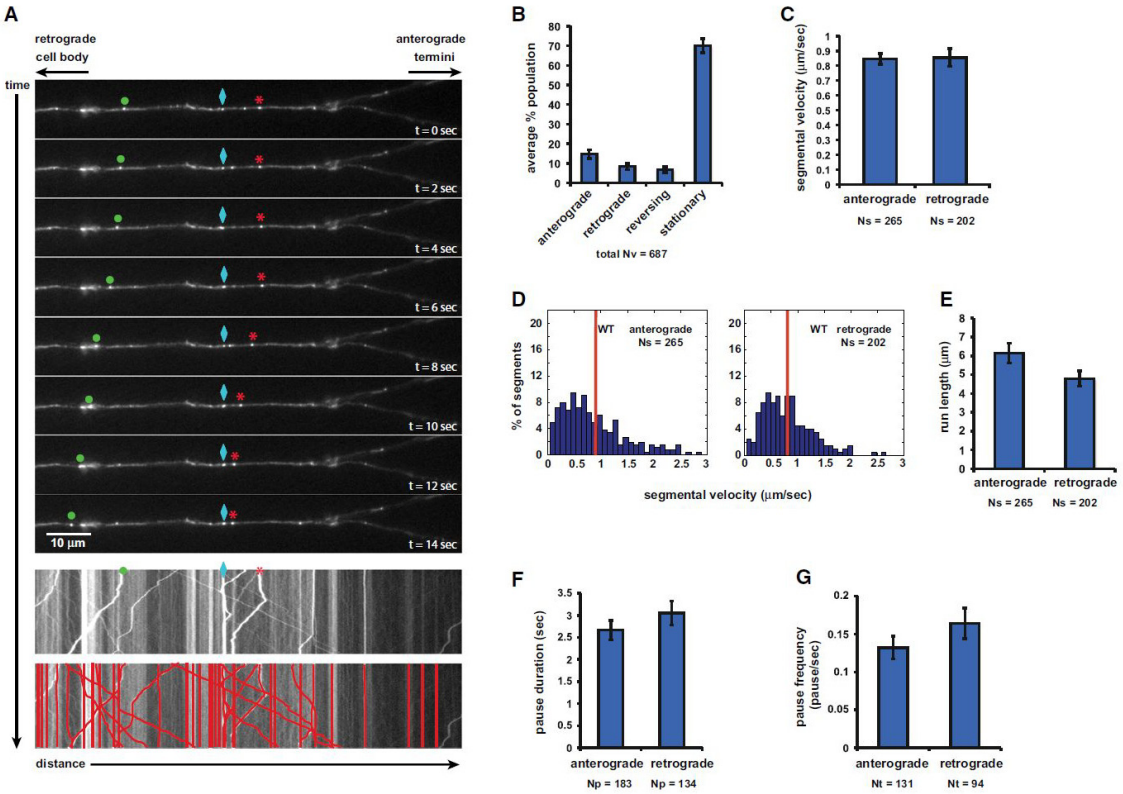


**Figure 4-1** $PrP^C$ vesicles are transported bidirectionally in wild-type hippocampal axons. (A) Top panels: sequential images of YFP-$PrP^C$ vesicle movement in a hippocampal axon. Vesicles moving bidirectionally (*), in a retrograde direction (•), and a stationary one (◊) are followed for a period of 14 seconds. Middle panel: kymograph generated from movie in (A). Bottom panel: same kymograph depicting individual particle traces generated by particle tracking software. (B) Population breakdown of YFP-$PrP^C$ vesicles. (C) Mean segmental velocity; (D) Segmental velocity histograms. Red lines show mean. (E) run length, (F) pause duration, and (G) pause frequency of YFP-$PrP^C$ vesicles. Nv = # vesicles; Np = # pauses; Nt = # tracks; Ns = # segments. All values are shown as mean ± SEM.

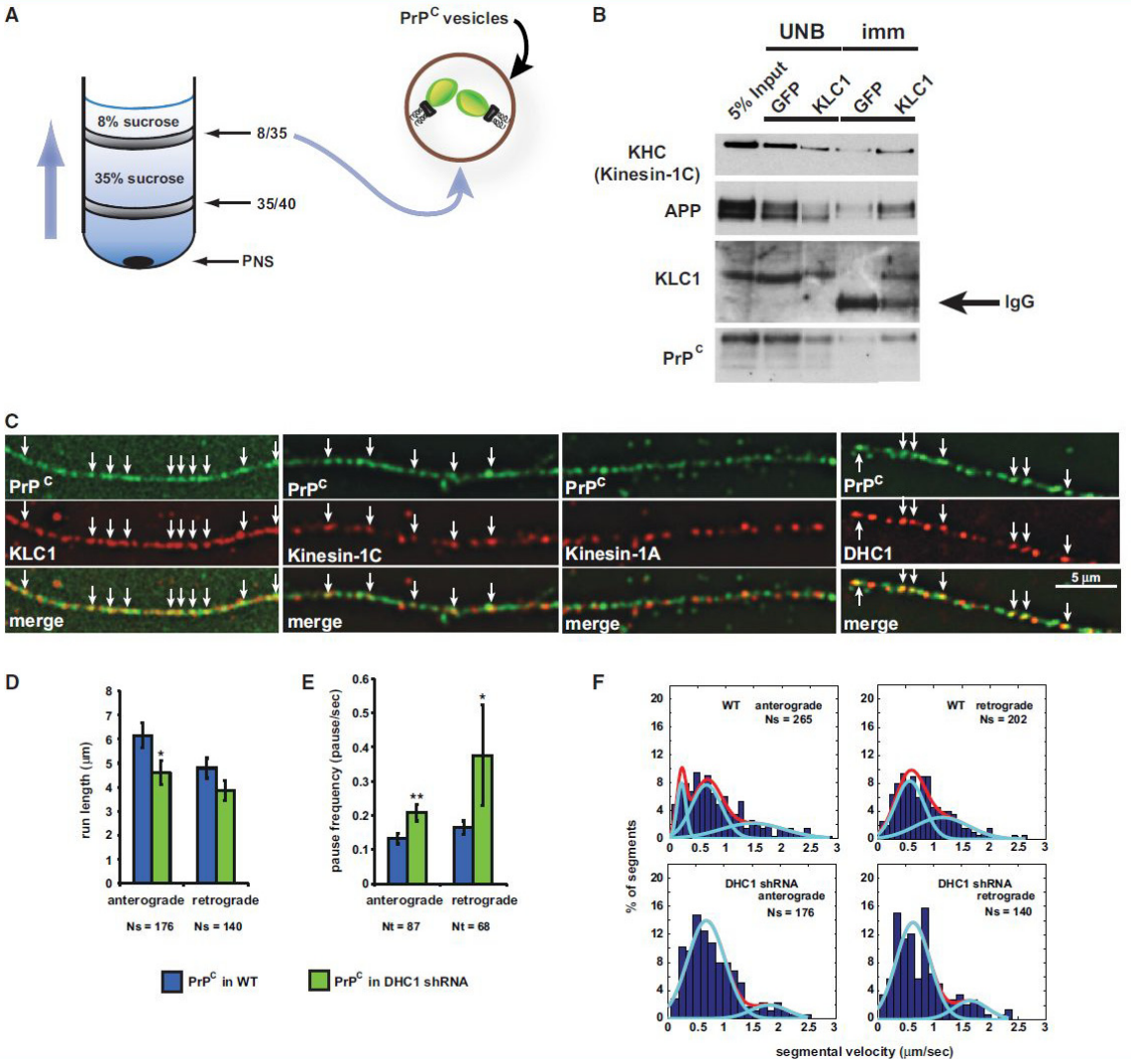


**Figure 4-2** $PrP^C$ vesicles associate with kinesin-1 and dynein. (A) Schematic diagram of a membrane flotation experiment showing the 8/35 fraction used as starting material for the vesicle immunoisolation in (B). Wild-type post-nuclear supernatant (PNS) obtained from wild-type mouse brain homogenate was bottom loaded. Buffers used did not contain detergent to prevent breaking of membranes. (B) An antibody against KLC1 was used to pull down associated membrane components from 8/35 fractions, including $PrP^C$-containing vesicles. KHC antibody recognizes mostly kinesin-1C. UNB = unbound fraction; imm = immunoisolation. Anti-GFP was used as a control. (C) Deconvolved images of vesicles stained with antibodies against $PrP^C$ and KLC1, kinesin-1C, kinesin-1A, or DHC1. Arrows point to some colocalization events. (D) Run length and (E) pause frequency in DHC1 shRNA axons. All values are shown as mean ± SEM. **p<0.01, *p<0.05, permutation t-test. (F) Segmental velocity histograms (shown as percent of segments) of YFP-$PrP^C$ transport in wild-type and DHC1 shRNA axons. Red and light blue curves represent the overall and predicted Gaussian modes, respectively. Ns = # segments; Nt = # tracks.

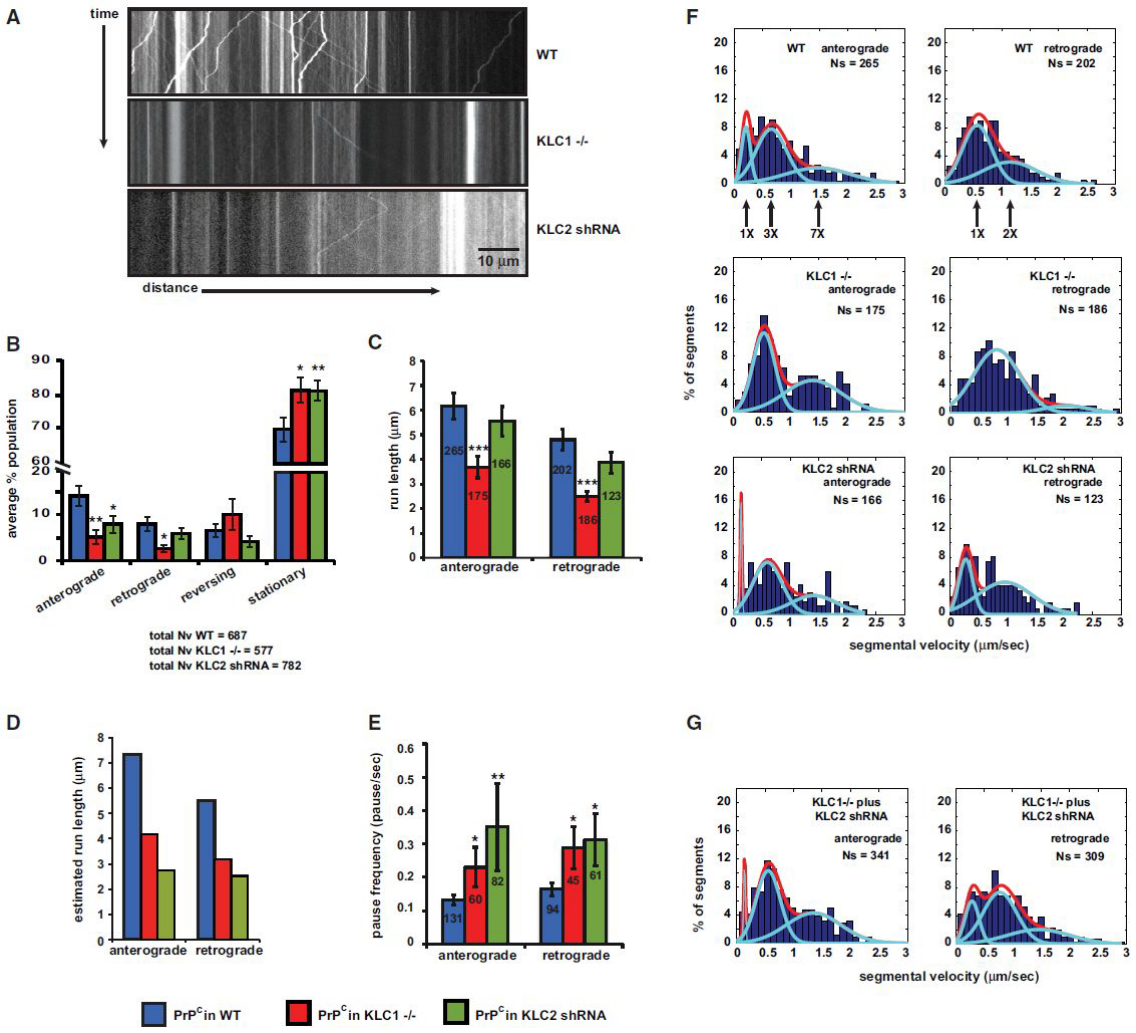


**Figure 4-3** PrP$^C$ vesicular transport is inhibited in kinesin light chain mutant axons. (A) Repre-sentative kymograph of YFP-PrP$^C$ vesicle movement in wild-type (top panel), KLC1 -/- (middle panel), and KLC2 shRNA (bottom panel) hippocampal axons. (B-E) Transport parameters in KLC1 -/- and KLC2 shRNA axons. (B) Population breakdown of YFP-PrP$^C$ vesicles (Nv = # vesicles), (C) run length, (D) estimated run length, and (E) pause frequency. Numbers inside bars are segments (run length in C), and tracks (pause frequency in E). All values are shown as mean ± SEM. ***p<0.001, **p<0.01, *p<0.05, permutation t-test. (F) Segmental velocity histograms (shown in percent of segments) in wild-type, KLC1 -/-, and KLC2 shRNA axons. Red and light blue curves represent the overall and predicted Gaussian modes, respectively. (G) Anterograde and retrograde wild-type segmental velocity histograms (shown as percent of segments) were reconstituted from adding together histograms of KLC1 -/- and KLC2 shRNA axons (in F).

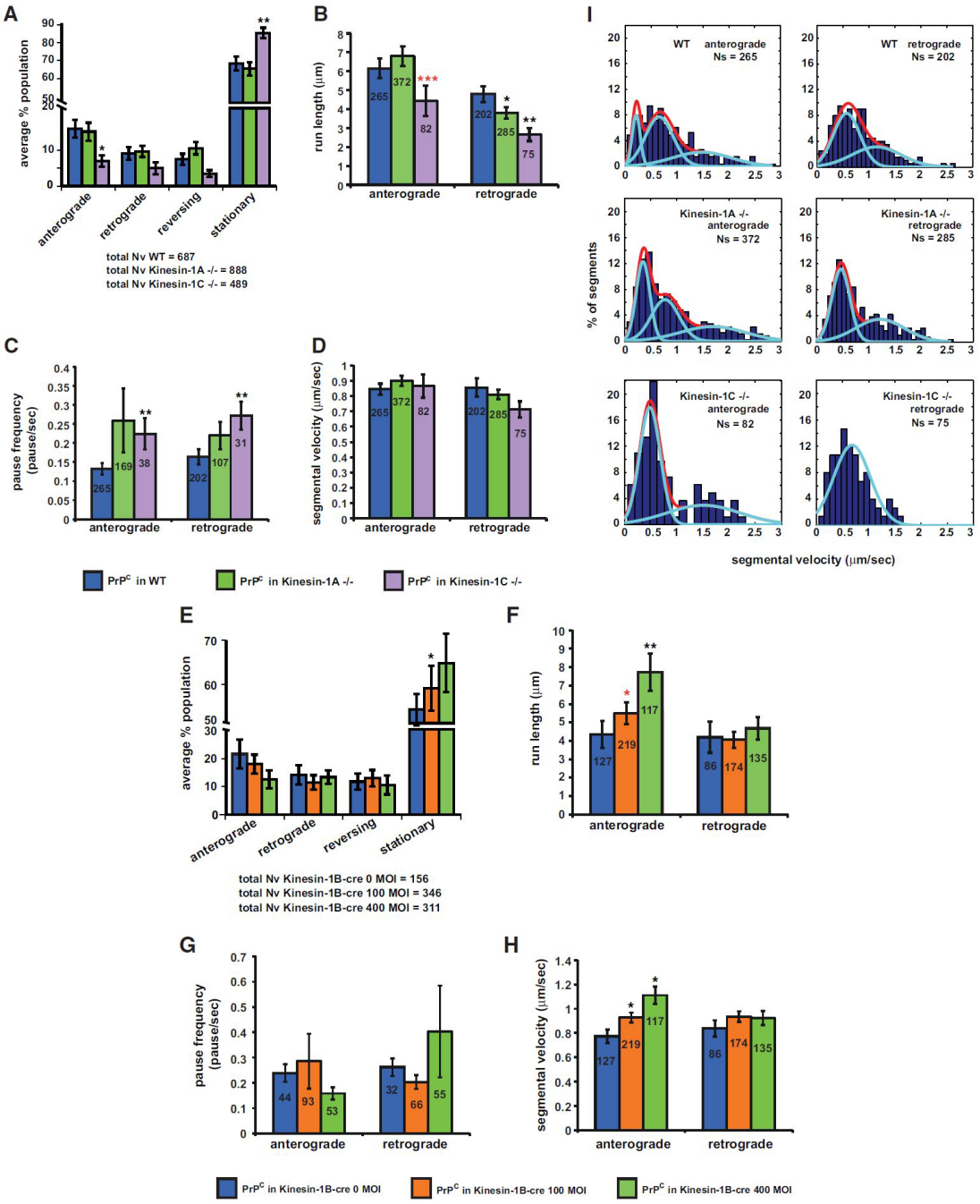


**Figure 4-4** $PrP^C$ vesicular transport is inhibited in kinesin-1C mutant axons. Transport parameters in kinesin-1A -/-, kinesin-1C -/-, and kinesin-1B-cre axons. (A,E) Population breakdown of YFP-$PrP^C$ vesicles (Nv = # vesicles), (B, F) run length, (C, G) pause frequency, (D, H) segmental velocity. ***p<0.001, **p<0.01, *p<0.05, permutation t-test (black asterisks), Wilcoxon-Mann-Whitney test (red asterisks). Numbers inside bars are segments (run length in B and F, segmental velocity in D and H), and tracks (pause frequency in C and G). All values are shown as mean ± SEM. (I) Segmental velocity histograms (shown as percent of segments) in wild-type, kinesin-1A -/-, and kinesin-1C -/- axons. Red and light blue curves represent the overall and predicted Gaussian modes, respectively.

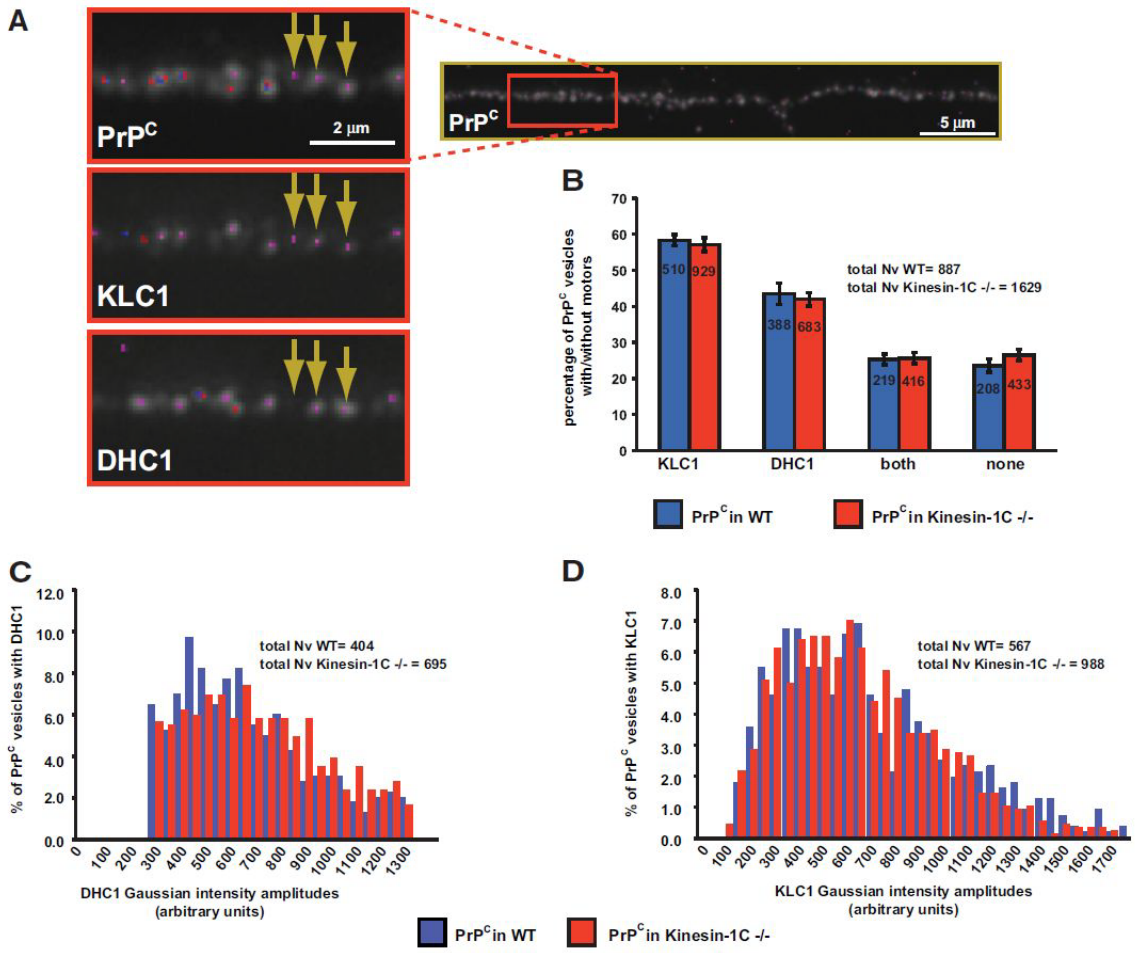


**Figure 4-5** (A-D). Composition of motor subunits on $PrP^C$ vesicles. (A) Representative immunofluorescence image of a hippocampal axon stained with antibodies against $PrP^C$, KLC1, and DHC1. Insets show enlargement with arrows pointing to three and two point sources in KLC1 and DHC1 channels, respectively, that associate with $PrP^C$ vesicles. Dots represent the location of fitted Gaussian functions. (B) Percentage of $PrP^C$ vesicles that have only KLC1, only DHC1, both, or no motor subunits associated with them. Inside bars are the numbers of vesicles for each category. All values are shown as mean ± SEM. (C-D) Gaussian intensity amplitude distributions comparing the frequency of $PrP^C$ vesicles associated with (C) DHC1 and (D) KLC1 intensities, in wild-type and kinesin-1C -/- axons.

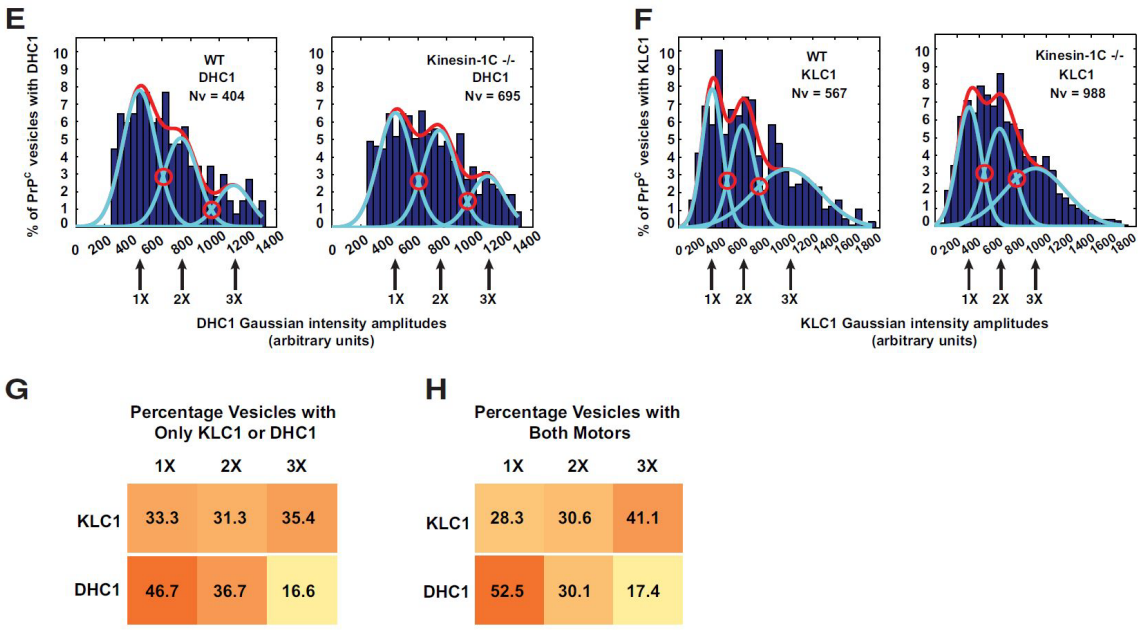


**Figure 4-5** (E-H). Composition of motor subunits on $PrP^C$ vesicles. (E-F) Histograms of the same Gaussian intensity amplitude distributions shown in (C, D), depicting percent of $PrP^C$ vesicles associated with (E) DHC1 and (F) KLC1. Red and light blue curves represent the overall and predicted Gaussian modes, respectively. Red open circles point to intersections between modes. (G-H) Distribution of $PrP^C$ vesicles with (G) one or (H) both associated motor subunits. Numbers in boxes are percentages of $PrP^C$ vesicles in each category. Color gradient represents higher to lower percentage of $PrP^C$ vesicles in each category. Nv = # vesicles.

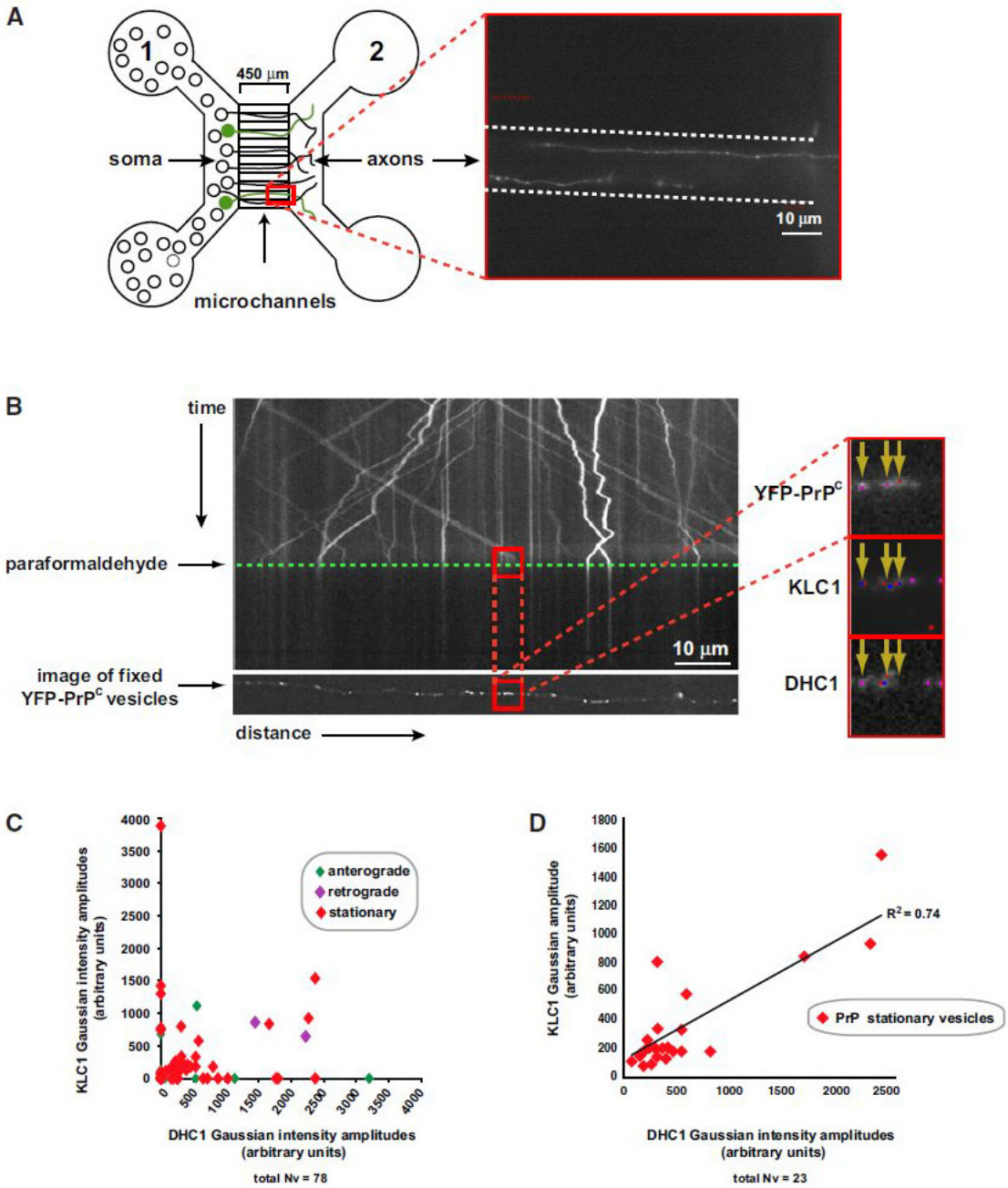


**Figure 4-6** Association of motor subunits with stationary and moving YFP-PrP$^C$ vesicles. (A) Left panel: schematic diagram of a microfluidic chamber device. Transfected neurons are shown in green. Right panel: inset of two axons transfected with YFP-PrP$^C$ growing through a single microchannel (outlined with dotted lines). (B) Kymograph of YFP-PrP$^C$ movement in the wild-type hippocampal axon shown in (A). Time of paraformaldehyde application is indicated by green dotted line. The panel below the kymograph is of the deconvolved image of the same fixed axon showing the YFP-PrP$^C$ channel. Red squares correspond to the same anterograde-moving vesicles in the kymograph that have been mapped to those in the fixed deconvolved image. Deconvolved images (inset) were taken of all three fixed/stained channels. Point sources were fitted with Gaussian functions (colored dots). (C, D) Scatter plots of KLC1 versus DHC1 Gaussian intensity amplitudes of (C) all moving and stationary mapped vesicles from n = 7 axons (with and without associated motor subunits), and of (D) stationary vesicles with detected motor subunits.

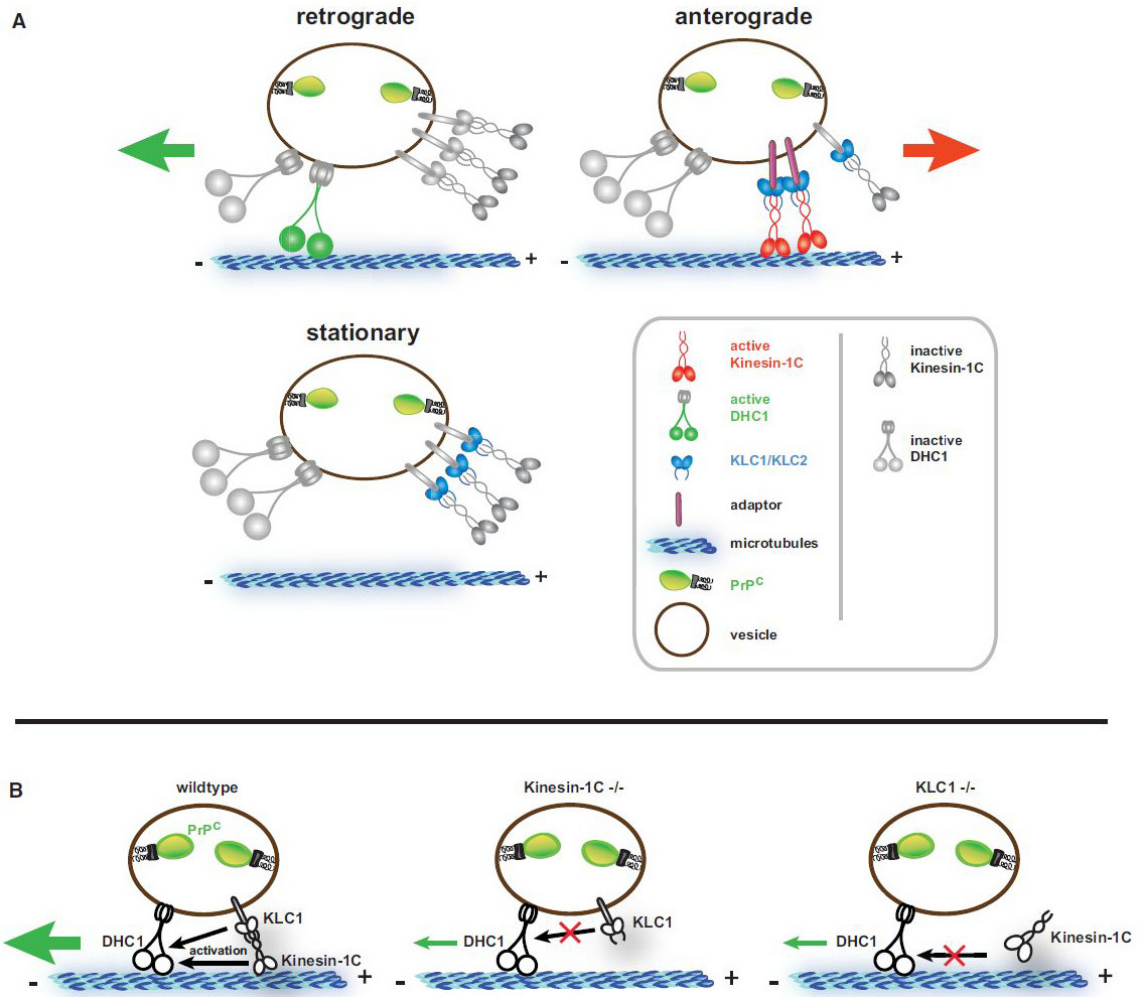


**Figure 4-7** A stable motor association and coordination model of $PrP^C$ vesicle transport. (A) A stable motor subunit composition on anterograde, retrograde, or stationary vesicles is depicted, but only a subset of those are active to drive transport in either direction. Our data suggests a coordination model whereby kinesin-1 and dynein act as alternating activators of opposite polarity transport. Number of motors depicted is arbitrary. See Discussion for details. (B) Activation of retrograde motility requires the vesicle association of a complete kinesin-1 holoenzyme comprised of both KLC1 and kinesin-1C. Removal of either subunit downregulates activation of DHC1, but does not dissociate DHC1 from $PrP^C$ vesicles. Thus, kinesin-1C can activate DHC1 via interaction with KLC1.

# APPENDIX

## 1. Definition of terms used in data analysis

**[Definition 1: track]** We define a *track* as a cargo trajectory that lasts through all frames of a time-lapse video. In this study, the track of a cargo is represented by its 2D position coordinate series over time $(x_1, y_1), (x_2, y_2), ..., (x_N, y_N)$, where $(x_i, y_i)$ represents its coordinate in the $i^{th}$ frame and $N$ is the total number of frames in the video.

**[Definition 2: track center]** We define the ***center*** of a track as the mean of its position coordinates over time. Denoted as $(x_c, y_c)$, it is calculated as:

$$x_c = \frac{1}{N}\sum_{i=1}^{N} x_i, \;\; y_c = \frac{1}{N}\sum_{i=1}^{N} y_i ,$$

In all of our time-lapse videos, the axon is approximately aligned with the horizontal image axis.

**[Definition 3: reversal (switch)]** We define a cargo as undergoing a ***reversal* (*switch*)** at its position $(x_k, y_k)$ in frame $k$, where $1 < k < N$, if it satisfies two conditions. First, two points $(x_{k-m}, y_{k-m}), (x_{k+n}, y_{k+n})$ are located at a distance greater than or equal to a threshold distance $c_{min}$ from $(x_k, y_k)$, i.e.

$$\sqrt{(x_{k-m} - x_k)^2 + (y_{k-m} - y_k)^2} \geq c_{min} \qquad 1 \leq m < k$$

$$\sqrt{(x_{k+n} - x_{k+n})^2 + (y_{k+n} - y_{k+n})^2} \geq c_{min} \qquad 1 < n \leq N - k .$$

For this study we chose $c_{min} = 550$ nm (determination of $c_{min}$ is discussed below). Second, vectors connecting $(x_k, y_k)$ with $(x_{k-m}, y_{k-m})$ and $(x_{k+n}, y_{k+n})$ point to opposite directions,

i.e.,

$$\left(x_{k-m}-x_k, y_{k-m}-y_k\right)\cdot\left(x_{k+n}-x_k, y_{k+n}-y_k\right)<0\,.$$

This definition is motivated by the fact that cargos can undergo small and random motion locally along their trajectories. The minimum distance $c_{min}$ allows us to avoid false positives in reversal detection caused by small local random movement. Based on this definition, several neighboring cargo positions may qualify as reversal points. In such cases, these positions are first clustered into a group and then sorted according to their horizontal coordinates. The leftmost (or rightmost) position is reported as the reversal position.

The value $c_{min}$ is determined empirically in two steps. First, we acquired a conservative estimation of the range of random motion of stationary cargos (see definition of stationary cargos below). This provides a lower limit for $c_{min}$. Then, $c_{min}$ is empirically adjusted so that results of reversal detection by our software match those of manual selection.

**[Definition 4: pause]** We define a cargo as undergoing a ***pause*** at its location $\left(x_k, y_k\right)$ in frame $k$, where $1<k<N$, if its instantaneous velocity at this location is below a threshold $V_{min}$. The instantaneous velocity of the cargo at $\left(x_k, y_k\right)$ is calculated using a sliding window approach:

$$V_{inst}=\frac{1}{T\cdot\left(2W+1\right)}\sum_{i=k-W}^{k+W}\sqrt{\left(x_i-x_{i-1}\right)^2+\left(y_i-y_{i-1}\right)^2}$$

Here $T$ is the sampling period, which equals 0.1 s in this study, and $W$ is chosen to be 3 frames, making the full sliding window width equal to 7 frames. $V_{min}$ is set to 0.075

pixel/frame (equivalent to ~0.10 μm/sec under the imaging settings of this study) to match the definition of pauses with the detection of stationary cargos (see the definition of stationary cargos below).

**[Definition 5: segment]** We define a ***segment*** (or a ***track segment***) as part of a track in which no reversal or pause is detected (i.e., a cargo moves consistently towards either the anterograde or the retrograde direction within a given segment). By definition, a track with no pause and no reversal qualifies as a segment. In this study, a track is first broken at its reversal positions (if detected) and then further broken into segments at frames immediately before and after individual pauses (if detected).

**[Definition 6: stationary cargo]** We define a cargo as ***stationary*** if its maximum deviation distance from the track center is no larger than a threshold value $d_{max}$, where $d_{max}$ represents the upper limit of allowed deviation from the track canter. That is, the trajectory of the cargo satisfies

$$\sqrt{\left(x_i - x_c\right)^2 + \left(y_i - y_c\right)^2} \le d_{max} \quad for \;\; i = 1..\mathrm{N}$$

In this study, we set $d_{max}$ to be 700 nm. This value is empirically determined in two steps. First, trajectories in kymographs are visually inspected, and stationary trajectories are manually selected. Second, the maximum deviation of all selected stationary tracks from their centers is calculated and chosen as $d_{max}$. For most stationary tracks, deviation from the track center is around 300~400 nm, which is substantially lower than the upper limit of 700 nm.

**[Definition 7: anterograde cargo]** A cargo is called ***anterograde*** if it is not stationary, has no reversal, and moves towards the synapse (i.e. towards the right in our videos). An anterograde cargo may or may not pause within its trajectory.

**[Definition 8: retrograde cargo]** A cargo is called ***retrograde*** if it is not stationary, has no reversal, and moves towards the neuronal cell body (i.e. towards the left in our videos). A retrograde cargo may or may not pause within its trajectory.

**[Definition 9: reversing cargo]** We refer to a cargo as ***reversing*** **(or *switching*)** if it undergoes at least one reversal.

## 2. Cargo motion descriptors

### 2.1 Population descriptors

In this study, a total of 10 animals were imaged for each genotype. For each animal, a total of 4 time lapse videos, each 15 seconds long, were collected. For each video, software tracked cargos were classified as being either stationary, anterograde, retrograde, or reversing, where $N_{stat}$, $N_{ante}$, $N_{retro}$, and $N_{rev}$ represent their numbers, respectively.

**[Definition 10: Fraction of stationary cargos]**

$$F_{stat}^{A} = \frac{N_{stat}}{N_{stat} + N_{ante} + N_{retro} + N_{rev}},$$

**[Definition 11: Fraction of anterograde cargos]**

$$F_{ante}^{A} = \frac{N_{ante}}{N_{stat} + N_{ante} + N_{retro} + N_{rev}},$$

**[Definition 12: Fraction of retrograde cargos]**

$$F_{retro}^{A} = \frac{N_{retro}}{N_{stat} + N_{ante} + N_{retro} + N_{rev}},$$

**[Definition 13: Fraction of reversing cargos]** The fraction of stationary cargos per animal is the average of the stationary cargo fraction calculated for each of its four time lapse movies. Fractions of anterograde, retrograde, and reversing cargos per animal are calculated similarly. For each genotype, the mean and standard error of the fraction of a given cargo type are calculated based on data of the 10 animals of this genotype.

$$F_{rev}^{A} = \frac{N_{rev}}{N_{stat} + N_{ante} + N_{retro} + N_{rev}}$$

**2.2 Velocity descriptors**

Each track is broken into segments, first at positions of reversals (if detected) and then at frames immediately before or after pauses (if detected). This ensures that within each segment there is no reversal or pause. A track without reversals will only have anterograde or retrograde segments; a track with reversals will have both.

**[Definition 14: Segmental velocity] Unit: μm/second.** The segmental velocity of a cargo within its track is defined for its individual segments. Specifically, for a track segment *k* starting at frame *P* and ending in frame *Q*, its segmental velocity is defined as the total distance it travels divided by the segment duration, i.e.

$$V_{seg}^{k} = \frac{1}{T(Q-P)} \sum_{i=P+1}^{Q} \sqrt{\left(x_i^k - x_{i-1}^k\right)^2 + \left(y_i^k - y_{i-1}^k\right)^2} \ ,$$

where *T* is the sampling period (0.1 sec in this study). Depending on the direction of the cargo movement within the segment, this velocity is reported as either an anterograde segmental velocity or a retrograde segmental velocity. Tracks with reversals have

segmental velocities in both directions. For each genotype, the mean and standard error of this parameter in each direction are calculated using segmental velocities of different segments in that direction pooled from all tracks.

**[Definition 15: Duration-weighted segmental velocity] Unit: μm/second.** The anterograde (retrograde) duration-weighted segmental velocity of a cargo within its track is defined as the sum of its anterograde (retrograde) segmental velocities weighted by their durations and divided by the sum of the durations. That is, for track *k* containing a total of $S_k$ segments in a given direction, this velocity is calculated as:

$$V_{dw\_seg}^{k} = \frac{\sum_{i=1}^{S_k} V_{seg}^{i} \cdot t_i}{\sum_{i=1}^{S_k} t_i},$$

where $V_{seg}^{i}$ and $t_i$ are the segmental velocity and duration of segment *i*, respectively. Under this definition, segmental velocities of longer durations are given higher weights. Anterograde (retrograde) duration-weighted segmental velocity is calculated based on anterograde (retrograde) segments for individual tracks. Tracks with reversals have duration-weighted segmental velocities in both directions. For each genotype, the mean and standard error of this parameter in each direction are computed using duration-weighted segmental velocities in that direction pooled from all tracks.

**2.3 Pause descriptors**

**[Definition 16: Total pause frequency] Unit: times/sec.** The total pause frequency of a cargo within its track is defined as its total number of pauses divided by its total time of movement (i.e. the duration of the time-lapse video minus the total duration of pauses). For track *k*, this frequency is calculated as

$$TPF_k = \frac{N_{pause}^k}{T \cdot N - \sum_{i=1}^{N_{pause}^k} t_{pause,i}^k}$$

where $N_{pause}^k$ is the number of pauses in track $k$, $t_{pause,i}^k$ is the duration of the $i^{th}$ pause, and $N$ is the total number of frames. The total pause frequency is calculated for tracks rather than segments. For each genotype, this parameter is calculated for each track in the anterograde or retrograde direction. Tracks with reversals have total pause frequencies in both directions. For each genotype, the mean and standard error of this measurement in each direction are computed using non-zero total pause frequencies in that direction pooled from all tracks.

**[Definition 17: Segmental pause frequency] Unit: times/sec**. The segmental pause frequency of a cargo within its track is defined for its individual pauses. For the $i^{th}$ pause of a track $k$, if the preceding segment lasts $T_k^i$ before pausing, the segmental pause frequency of this pause is defined as

$$SPF_k^i = \frac{1}{T_k^i}$$

As this parameter depends only on the duration of the preceding segment, it is calculated for individual segments rather than tracks. For each genotype, it is calculated for each pause in the anterograde or retrograde direction (defined by the direction of the segment in which this pause resides). Tracks with reversals have both anterograde and retrograde segmental pause frequencies. For each genotype, the mean and standard error of this measurement in each direction are computed using non-zero segmental pause frequencies of different pauses in that direction pooled from all tracks.

**[Definition 18: Pause duration] Unit: sec.** The pause duration of a cargo within its track is defined for its individual pauses, i.e. it is calculated for individual pauses rather than tracks. For each genotype, this parameter is calculated for each pause in the anterograde or retrograde direction (defined by the direction of the segment in which this pause resides). Vesicles with reversals have pause durations in both directions. For each genotype, the mean and standard error of this parameter in each direction are computed using non-zero pause durations of different segments in that direction pooled from all tracks.

**2.4. Run length descriptor**

**[Definition 19: Run length] Unit: µm.** The run length of a cargo is defined for each of its individual segments. For segment *i* of track *k*, which starts at frame *P* and ends at frame *Q*, the run length is defined as

$$RL_k^i = \sum_{j=P+1}^{Q} \sqrt{\left(x_k^j - x_k^{j-1}\right)^2 + \left(y_k^j - y_k^{j-1}\right)^2}$$

For each genotype, the mean and standard error of this parameter are computed separately for the anterograde and retrograde direction pooling data from all tracks.

**2.5. Reversal (switch) descriptor**

**[Definition 20: Switch frequency] Unit: times/sec.** The switch frequency of a cargo within its track is defined as the number of reversals per second. For track *k***,** it is calculated as

$$SF_k = \frac{N_{rev}^k}{T \cdot N},$$

where $N_{rev}^{k}$ is the number of detected reversals. Reversal frequency is direction neutral, so it is *not* reported separately for anterograde and retrograde populations. For each genotype, reversal frequency is calculated for tracks rather than segments. The mean and standard deviation of this parameter are computed using switch frequencies pooled from all tracks.

## 3. Statistical data analysis

### 3.1 Statistical tests

Distributions of segmental velocities and duration weighted segmental velocities follow a mixture of multiple normal distribution modes rather than a single normal distribution. For this reason we chose non-parametric permutation t-tests (Moore and McCabe 2005) to assess differences between means. When differences between means of segmental velocities of different genotypes were not statistically significant, we further assess their differences by comparing their distributions in terms of their medians using Wilcoxon-Mann-Whitney rank-sum tests. Black asterisks are used when the permutation t-test indicates significant changes. Red asterisks are used when the permutation t-test does *not* indicate significant changes but the Wilcoxon-Mann-Whitney test does,

We used permutation t-tests to assess differences between average fractions of anterograde, retrograde, reversing, and stationary cargo populations (see descriptors 1-4) as their distributions are generally bell-shaped. Distributions of pause frequency and pause duration generally are not bell-shaped but instead resembled exponential distributions. We used Wilcoxon rank-sum tests to assess differences between average pause frequencies and duration of the various genotypes analyzed.

Distributions of run lengths generally are generally bell-shaped but do not follow a single normal distribution. We therefore used non-parametric permutation t-tests to assess differences between their means in different genotypes. Again, when differences were not statistically significant, we further assessed differences between their distributions in terms of their medians using Wilcoxon-Mann-Whitney rank-sum tests. Black asterisks are used when the permutation t-test indicates significant changes. Red asterisks are used when the permutation t-test does *not* indicate significant changes but the Wilcoxon-Mann-Whitney test does.

**3.2 Classification of segmental velocities into different modes**

Segmental velocities generally follow a mixture of three normal distribution modes $N(\mu_i, \sigma_i), i = 1,2,3$, where $\mu_1 < \mu_2 < \mu_3$. The weight of each mode, denoted $w_i, i = 1..3$, represents the fraction of segmental velocities in that mode. Classification of a segmental velocity $v_i$ to a specific mode is based on the following rules

If $0<v_i \le t_1$, $v_i$ belongs to mode 1
If $t_1<v_i \le t_2$, $v_i$ belongs to mode 2
If $v_i > t_2$, $v_i$ belongs to mode 3

where $t_1$ and $t_2$ are two classification thresholds (Theodoridis and Koutroumbas 2008) that satisfy $t_1 < t_2$. Threshold $t_1$ is a solution of the following equation

$$\frac{w_1}{\sigma_1\sqrt{2\pi}} exp\left(-\frac{(x-\mu_1)^2}{2\sigma_1^2}\right) = \frac{w_2}{\sigma_2\sqrt{2\pi}} exp\left(-\frac{(x-\mu_2)^2}{2\sigma_2^2}\right),$$

It can be calculated as a root of the following quadratic equation

$$\left(\frac{1}{2\sigma_2^2}-\frac{1}{2\sigma_1^2}\right)x^2+\left(\frac{\mu_1}{\sigma_1^2}-\frac{\mu_2}{\sigma_2^2}\right)x+\left(\frac{\mu_2^2}{2\sigma_2^2}-\frac{\mu_1^1}{2\sigma_1^2}-log\frac{w_2\sigma_1}{w_1\sigma_2}\right)=0$$

Similarly, threshold $t_2$ can be calculated as a solution of the following equation

$$\frac{w_2}{\sigma_2\sqrt{2\pi}}exp\left(-\frac{(x-\mu_2)^2}{2\sigma_2^2}\right)=\frac{w_2}{\sigma_3\sqrt{2\pi}}exp\left(-\frac{(x-\mu_3)^2}{2\sigma_3^2}\right),$$

**3.3 Calculation of mode transition probabilities**

For a specific genotype, let $v_i^-$ and $v_i^+$ denote a pair of segmental velocities before and after a pause. Let *N* denote the total number of such pairs of segmental velocities. The probability of cargo staying in the same mode before and after pause is calculated as $\frac{N_0}{N}$, where $N_0$ is the number of velocity pairs in which $v_i^-$ and $v_i^+$ belong to the same mode. Similarly, the probability of cargo changing to a neighboring mode (a change of mode index by 1, i.e. $1\leftrightarrow 2$ or $2\leftrightarrow 3$) is calculated as $\frac{N_1}{N}$, where $N_1$ represents the number of segmental velocity pairs under this category; the probability of cargo jumping between modes (a change of mode index by 2; i.e. $1\leftrightarrow 3$), is calculated as $\frac{N_2}{N}$ where $N_2$ is the number of qualified segmental velocity pairs.

## REFERENCES


Akhmanova, A. and J. A. Hammer, 3rd (2010). "Linking molecular motors to membrane cargo." Curr Opin Cell Biol **22**(4): 479-487.

Ally, S., A. G. Larson, et al. (2009). "Opposite-polarity motors activate one another to trigger cargo transport in live cells." J Cell Biol **187**(7): 1071-1082.

Amaratunga, A., P. J. Morin, et al. (1993). "Inhibition of kinesin synthesis and rapid anterograde axonal transport in vivo by an antisense oligonucleotide." J Biol Chem **268**(23): 17427-17430.

Anthony, S. M. and S. Granick (2009). "Image analysis with rapid and accurate two-dimensional Gaussian fitting." Langmuir **25**(14): 8152-8160.

Baas, P. W. (1999). "Microtubules and neuronal polarity: lessons from mitosis." Neuron **22**(1): 23-31.

Baas, P. W., M. M. Black, et al. (1989). "Changes in microtubule polarity orientation during the development of hippocampal neurons in culture." J Cell Biol **109**(6 Pt 1): 3085-3094.

Baas, P. W., J. S. Deitch, et al. (1988). "Polarity orientation of microtubules in hippocampal neurons: uniformity in the axon and nonuniformity in the dendrite." Proc Natl Acad Sci U S A **85**(21): 8335-8339.

Blackman, S. (1999). Design and analysis of modern tracking systems, Artech House Publishers.

Blasius, T. L., D. Cai, et al. (2007). "Two binding partners cooperate to activate the molecular motor Kinesin-1." J. Cell Biol. **176**(1): 11-17.

Block, S. M. (1995). "Nanometres and piconewtons: the macromolecular mechanics of kinesin." Trends Cell Biol **5**(4): 169-175.

Block, S. M., L. S. Goldstein, et al. (1990). "Bead movement by single kinesin molecules studied with optical tweezers." Nature **348**(6299): 348-352.

Borchelt, D. R., J. Davis, et al. (1996). "A vector for expressing foreign genes in the brains and hearts of transgenic mice." Genet Anal **13**(6): 159-163.

Borchelt, D. R., V. E. Koliatsos, et al. (1994). "Rapid anterograde axonal transport of the cellular prion glycoprotein in the peripheral and central nervous systems." J Biol Chem **269**(20): 14711-14714.

Bornfleth, H., P. Edelmann, et al. (1999). "Quantitative motion analysis of subchromosomal foci in living cells using four-dimensional microscopy." Biophys J **77**(5): 2871-2886.

Bowman, A. B., R. S. Patel-King, et al. (1999). "Drosophila roadblock and Chlamydomonas LC7: a conserved family of dynein-associated proteins involved in axonal transport, flagellar motility, and mitosis." J Cell Biol **146**(1): 165-180.

Boylan, K. L. M. and T. S. Hays (2002). "The Gene for the Intermediate Chain Subunit of Cytoplasmic Dynein Is Essential in Drosophila." Genetics **162**(3): 1211-1220.

Brendza, R. P., K. B. Sheehan, et al. (2000). "Clonal tests of conventional kinesin function during cell proliferation and differentiation." Mol Biol Cell **11**(4): 1329-1343.

Butowt, R., S. Abdelraheim, et al. (2006). "Anterograde axonal transport of the exogenous cellular isoform of prion protein in the chick visual system." Mol Cell Neurosci **31**(1): 97-108.

Butowt, R., P. Davies, et al. (2007). "Anterograde axonal transport of chicken cellular prion protein (PrPc) in vivo requires its N-terminal part." J Neurosci Res **85**(12): 2567-2579.

Cai, D., A. D. Hoppe, et al. (2007). "Kinesin-1 structural organization and conformational changes revealed by FRET stoichiometry in live cells." J Cell Biol **176**(1): 51-63.

Caughey, B., G. S. Baron, et al. (2009). "Getting a grip on prions: oligomers, amyloids, and pathological membrane interactions." Annu Rev Biochem **78**: 177-204.

Cheezum, M. K., W. F. Walker, et al. (2001). "Quantitative comparison of algorithms for tracking single fluorescent particles." Biophys J **81**(4): 2378-2388.

Chevalier-Larsen, E. and E. L. Holzbaur (2006). "Axonal transport and neurodegenerative disease." Biochim Biophys Acta **1762**(11-12): 1094-1108.

Crevenna, A. H., S. Madathil, et al. (2008). "Secondary structure and compliance of a predicted flexible domain in kinesin-1 necessary for cooperation of motors." Biophys J **95**(11): 5216-5227.

Cui, J., Z. Wang, et al. (2010). "Targeted Inactivation of Kinesin-1 in Pancreatic {beta}-Cells in vivo Leads to Insulin Secretory Deficiency." Diabetes.

de Cuevas, M., T. Tao, et al. (1992). "Evidence that the stalk of Drosophila kinesin heavy chain is an alpha-helical coiled coil." J Cell Biol **116**(4): 957-965.

De Vos, K. J., A. J. Grierson, et al. (2008). "Role of Axonal Transport in Neurodegenerative Diseases." Annual Review of Neuroscience **31**(1): 151-173.

DeBoer, S. R., Y. You, et al. (2008). "Conventional kinesin holoenzymes are composed of heavy and light chain homodimers." Biochemistry **47**(15): 4535-4543.

Dixit, R., J. L. Ross, et al. (2008). "Differential regulation of dynein and kinesin motor proteins by tau." Science **319**(5866): 1086-1089.

Duncan, J. E. and L. S. Goldstein (2006). "The genetics of axonal transport and axonal transport disorders." PLoS Genet **2**(9): e124.

Duncan, J. E. and R. Warrior (2002). "The cytoplasmic dynein and kinesin motors have interdependent roles in patterning the Drosophila oocyte." Curr Biol **12**(23): 1982-1991.

Encalada, S. E., L. Szpankowski, et al. (2011). "Stable kinesin and dynein assemblies drive the axonal transport of mammalian prion protein vesicles." Cell **144**(4): 551-565.

Falzone, T. L., G. B. Stokin, et al. (2009). "Axonal stress kinase activation and tau misbehavior induced by kinesin-1 transport defects." J Neurosci **29**(18): 5758-5767.

Ferreira, A., J. Niclas, et al. (1992). "Suppression of kinesin expression in cultured hippocampal neurons using antisense oligonucleotides." J. Cell Biol. **117**(3): 595-606.

Fraley, C. (1999). "MCLUST: Software for Model-Based Cluster Analysis." Journal of Classification **16**: 297-306.

Fraley, C. and A. E. Raftery (2002). "Model-based clustering, discriminant analysis and density estimation." J American Statistical Association **97**: 611-631.

Geng, J., M. Baba, et al. (2008). "Quantitative analysis of autophagy-related protein stoichiometry by fluorescence microscopy." J Cell Biol **182**(1): 129-140.

Gennerich, A., A. P. Carter, et al. (2007). "Force-induced bidirectional stepping of cytoplasmic dynein." Cell **131**: 952-965.

Gennerich, A. and R. D. Vale (2009). "Walking the walk: how kinesin and dynein coordinate their steps." Current Opinion in Cell Biology **21**(1): 59-67.

Gindhart, J. G., J. Chen, et al. (2003). "The kinesin-associated protein UNC-76 is required for axonal transport in the Drosophila nervous system." Mol Biol Cell **14**(8): 3356-3365.

Gindhart, J. G., Jr., C. J. Desai, et al. (1998). "Kinesin light chains are essential for axonal transport in Drosophila." J Cell Biol **141**(2): 443-454.

Glater, E. E., L. J. Megeath, et al. (2006). "Axonal transport of mitochondria requires milton to recruit kinesin heavy chain and is light chain independent." J Cell Biol **173**(4): 545-557.

Goldsbury, C., M. M. Mocanu, et al. (2006). "Inhibition of APP trafficking by tau protein does not increase the generation of amyloid-beta peptides." Traffic **7**(7): 873-888.

Goldstein, A. Y., X. Wang, et al. (2008). "Axonal transport and the delivery of pre-synaptic components." Curr Opin Neurobiol **18**(5): 495-503.

Goldstein, L. S. (2003). "Do disorders of movement cause movement disorders and dementia?" Neuron **40**(2): 415-425.

Goldstein, L. S. and A. V. Philp (1999). "The road less traveled: emerging principles of kinesin motor utilization." Annu Rev Cell Dev Biol **15**: 141-183.

Goldstein, L. S. and Z. Yang (2000). "Microtubule-based transport systems in neurons: the roles of kinesins and dyneins." Annu Rev Neurosci **23**: 39-71.

Goulian, M. and S. M. Simon (2000). "Tracking single proteins within cells." Biophys J **79**(4): 2188-2198.

Grafstein, B. and D. S. Forman (1980). "Intracellular transport in neurons." Physiol. Rev. **60**(4): 1167-1283.

Gross, S. P. (2004). "Hither and yon: a review of bi-directional microtubule-based transport." Phys Biol **1**(1-2): R1-11.

Gross, S. P., M. C. Tuma, et al. (2002). "Interactions and regulation of molecular motors in Xenopus melanophores." J Cell Biol **156**(5): 855-865.

Gross, S. P., M. A. Welte, et al. (2002). "Coordination of opposite-polarity microtubule motors." J Cell Biol **156**(4): 715-724.

Gunawardena, S., L. S. Her, et al. (2003). "Disruption of axonal transport by loss of huntingtin or expression of pathogenic polyQ proteins in Drosophila." Neuron **40**(1): 25-40.

Haghnia, M., V. Cavalli, et al. (2007). "Dynactin is required for coordinated bidirectional motility, but not for dynein membrane attachment." Mol Biol Cell **18**(6): 2081-2089.

Hampel, H., K. Burger, et al. (2008). "Core candidate neurochemical and imaging biomarkers of Alzheimer's disease." Alzheimers Dement **4**(1): 38-48.

Harris, D. A. (2003). "Trafficking, turnover and membrane topology of PrP." Br Med Bull **66**: 71-85.

Hendricks, A. G., E. Perlson, et al. (2010). "Motor Coordination via a Tug-of-War Mechanism Drives Bidirectional Vesicle Transport." Curr Biol.

Hill, D. B., M. J. Plaza, et al. (2004). "Fast vesicle transport in PC12 neurites: velocities and forces." Eur Biophys J **33**(7): 623-632.

Hirokawa, N. (1982). "Cross-linker system between neurofilaments, microtubules and membranous organelles in frog axons revealed by the quick-freeze, deep-etching method." J. Cell Biol. **94**(1): 129-142.

Hirokawa, N. and R. Takemura (2005). "Molecular motors and mechanisms of directional transport in neurons." Nat. Rev. Neurosci. **6**: 201-214.

Howard, J. (2001). Mechanics of motor proteins and the cytoskeleton. SunderLand, MA, Sinauer Associates.

Howard, J., A. J. Hudspeth, et al. (1989). "Movement of microtubules by single kinesin molecules." Nature **342**(6246): 154-158.

Hurd, D. D. and W. M. Saxton (1996). "Kinesin mutations cause motor neuron disease phenotypes by disrupting fast axonal transport in Drosophila." Genetics **144**(3): 1075-1085.

Hurd, D. D., M. Stern, et al. (1996). "Mutation of the axonal transport motor kinesin enhances paralytic and suppresses Shaker in Drosophila." Genetics **142**(1): 195-204.

Jaqaman, K., D. Loerke, et al. (2008). "Robust single-particle tracking in live-cell time-lapse sequences." Nat. Methods **5**(8): 695-702.

Kaether, C., P. Skehel, et al. (2000). "Axonal Membrane Proteins Are Transported in Distinct Carriers: A Two-Color Video Microscopy Study in Cultured Hippocampal Neurons." Mol. Biol. Cell **11**(4): 1213-1224.

Kamal, A., G. B. Stokin, et al. (2000). "Axonal transport of amyloid precursor protein is mediated by direct binding to the kinesin light chain subunit of kinesin-I." Neuron **28**(2): 449-459.

Kang, J. S., J. H. Tian, et al. (2008). "Docking of axonal mitochondria by syntaphilin controls their mobility and affects short-term facilitation." Cell **132**(1): 137-148.

Kardon, J. R. and R. D. Vale (2009). "Regulators of the cytoplasmic dynein motor." Nat. Rev. Mol. Cell Biol. **10**(12): 854-865.

Karki, S. and E. L. Holzbaur (1999). "Cytoplasmic dynein and dynactin in cell division and intracellular transport." Curr Opin Cell Biol **11**(1): 45-53.

Karr, T. L. and B. M. Alberts (1986). "Organization of the cytoskeleton in early Drosophila embryos." J Cell Biol **102**(4): 1494-1509.

Kim, H., S. C. Ling, et al. (2007). "Microtubule binding by dynactin is required for microtubule organization but not cargo transport." J Cell Biol **176**(5): 641-651.

King, S. J., C. L. Brown, et al. (2003). "Analysis of the dynein-dynactin interaction in vitro and in vivo." Mol Biol Cell **14**(12): 5089-5097.

King, S. J. and T. A. Schroer (2000). "Dynactin increases the processivity of the cytoplasmic dynein motor." Nat Cell Biol **2**(1): 20-24.

King, S. M. (2000). "The dynein microtubule motor." Biochim. Biophys. Acta. **1496**: 60-75.

Koo, E. H., S. S. Sisodia, et al. (1990). "Precursor of amyloid protein in Alzheimer disease undergoes fast anterograde axonal transport." Proc Natl Acad Sci U S A **87**(4): 1561-1565.

Kubitscheck, U., O. Kuckmann, et al. (2000). "Imaging and tracking of single GFP molecules in solution." Biophys J **78**(4): 2170-2179.

Kural, C., H. Kim, et al. (2005). "Kinesin and dynein move a peroxisome in vivo: a tug-of-war or coordinated movement?" Science **308**(5727): 1469-1472.

Lawrence, C. J., R. K. Dawe, et al. (2004). "A standardized kinesin nomenclature." J Cell Biol **167**(1): 19-22.

Levi, V., A. S. Serpinskaya, et al. (2006). "Organelle transport along microtubules in Xenopus melanophores: evidence for cooperation between multiple motors." Biophys J **90**(1): 318-327.

Levy, J. R. and E. L. Holzbaur (2006). "Cytoplasmic dynein/dynactin function and dysfunction in motor neurons." Int J Dev Neurosci **24**(2-3): 103-111.

Ligon, L. A., M. Tokito, et al. (2004). "A direct interaction between cytoplasmic dynein and kinesin I may coordinate motor activity." J Biol Chem **279**(18): 19201-19208.

Lu, H., M. Y. Ali, et al. (2009). "Diffusive movement of processive kinesin-1 on microtubules." Traffic **10**(10): 1429-1438.

Lyman, M. G. and L. W. Enquist (2009). "Herpesvirus interactions with the host cytoskeleton." J Virol **83**(5): 2058-2066.

Malaga-Trillo, E., G. P. Solis, et al. (2009). "Regulation of embryonic cell adhesion by the prion protein." PLoS Biol **7**(3): e55.

Martin, M., S. J. Iyadurai, et al. (1999). "Cytoplasmic dynein, the dynactin complex, and kinesin are interdependent and essential for fast axonal transport." Mol Biol Cell **10**(11): 3717-3728.

Mazumdar, M., A. Mikami, et al. (1996). "In vitro motility from recombinant dynein heavy chain." Proc Natl Acad Sci U S A **93**(13): 6552-6556.

McGrail, M. and T. S. Hays (1997). "The microtubule motor cytoplasmic dynein is required for spindle orientation during germline cell divisions and oocyte differentiation in Drosophila." Development **124**(12): 2409-2419.

Moore, D. S. and G. P. McCabe (2005). Introduction to the Practice of Statistics, 5th edition., W. H. Freeman.

Mouillet-Richard, S., M. Ermonval, et al. (2000). "Signal transduction through prion protein." Science **289**(5486): 1925-1928.

Moya, K. L., R. Hassig, et al. (2004). "Enhanced detection and retrograde axonal transport of PrPc in peripheral nerve." J Neurochem **88**(1): 155-160.

Muller, M. J., S. Klumpp, et al. (2008). "Tug-of-war as a cooperative mechanism for bidirectional cargo transport by molecular motors." Proc Natl Acad Sci U S A **105**(12): 4609-4614.

Netten, H., I. T. Young, et al. (1997). "FISH and chips: automation of fluorescent dot counting in interphase cell nuclei." Cytometry **28**(1): 1-10.

Okada, Y., H. Yamazaki, et al. (1995). "The neuron-specific kinesin superfamily protein KIF1A is a unique monomeric motor for anterograde axonal transport of synaptic vesicle precursors." Cell **81**(5): 769-780.

Pfister, K. K., P. R. Shah, et al. (2006). "Genetic analysis of the cytoplasmic dynein subunit families." PLoS Genet **2**(1): e1.

Plitz, T. and K. Pfeffer (2001). "Intact lysosome transport and phagosome function despite kinectin deficiency." Mol Cell Biol **21**(17): 6044-6055.

Ponti, A., P. Vallotton, et al. (2003). "Computational Analysis of F-Actin Turnover in Cortical Actin Meshworks Using Fluorescent Speckle Microscopy." Biophys. J. **84**(5): 3336-3352.

Radtke, K., D. Kieneke, et al. (2010). "Plus- and minus-end directed microtubule motors bind simultaneously to herpes simplex virus capsids using different inner tegument structures." PLoS Pathog **6**(7): e1000991.

Rahman, A., D. S. Friedman, et al. (1998). "Two kinesin light chain genes in mice. Identification and characterization of the encoded proteins." J Biol Chem **273**(25): 15395-15403.

Rahman, A., A. Kamal, et al. (1999). "Defective kinesin heavy chain behavior in mouse kinesin light chain mutants." J Cell Biol **146**(6): 1277-1288.

Reck-Peterson, S. L., A. Yildiz, et al. (2006). "Single-molecule analysis of dynein processivity and stepping behaviro." Cell **126**: 335-348.

Rodolfo, K., R. Hassig, et al. (1999). "A novel cellular prion protein isoform present in rapid anterograde axonal transport." Neuroreport **10**(17): 3639-3644.

Sato-Yoshitake, R., H. Yorifuji, et al. (1992). "The phosphorylation of kinesin regulates its binding to synaptic vesicles." J Biol Chem **267**(33): 23930-23936.

Saxton, W. M., J. Hicks, et al. (1991). "Kinesin heavy chain is essential for viability and neuromuscular functions in Drosophila, but mutants show no defects in mitosis." Cell **64**(6): 1093-1102.

Schnitzer, M. J. and S. M. Block (1997). "Kinesin hydrolyses one ATP per 8-nm step." Nature **388**(6640): 386-390.

Schroer, T. A. (2004). "Dynactin." Annu. Rev. Cell Dev. Biol. **20**: 759-779.

Shubeita, G. T., S. L. Tran, et al. (2008). "Consequences of motor copy number on the intracellular transport of kinesin-1-driven lipid droplets." Cell **135**(6): 1098-1107.

Simons, M., E. Ikonen, et al. (1995). "Intracellular routing of human amyloid protein precursor: axonal delivery followed by transport to the dendrites." J Neurosci Res **41**(1): 121-128.

Slemmon, J. R., P. M. Salvaterra, et al. (1982). "Purification of choline acetyltransferase from Drosophila melanogaster." J Biol Chem **257**(7): 3847-3852.

Soppina, V., A. K. Rai, et al. (2009). "Tug-of-war between dissimilar teams of microtubule motors regulates transport and fission of endosomes." Proc Natl Acad Sci U S A.

Souchier, C., C. Brisson, et al. (2003). "Data reproducibility in fluorescence image analysis." Methods Cell Sci **25**(3-4): 195-200.

Spudich, J. (1990). "Optical trapping: molecular molecules in motion." Nature **348**: 284-285.

Stamer, K., R. Vogel, et al. (2002). "Tau blocks traffic of organelles, neurofilaments, and APP vesicles in neurons and enhances oxidative stress." J Cell Biol **156**(6): 1051-1063.

Stokin, G. B. and L. S. B. Goldstein (2006). "Axonal transport and Alzheimer's disease." Ann. Rev. Biochemistry **75**: 607-627.

Stone, M. C., F. Roegiers, et al. (2008). "Microtubules Have Opposite Orientation in Axons and Dendrites of Drosophila Neurons." Mol. Biol. Cell **19**(10): 4122-4129.

Sugiyama, Y., I. Kawabata, et al. (2005). "Determination of absolute protein numbers in single synapses by a GFP-based calibration technique." Nat. Methods **2**(9): 677-684.

Svoboda, K., C. F. Schmidt, et al. (1993). "Direct observation of kinesin stepping by optical trapping interferometry." Nature **365**(6448): 721-727.

Szodorai, A., Y. H. Kuan, et al. (2009). "APP anterograde transport requires Rab3A GTPase activity for assembly of the transport vesicle." J Neurosci **29**(46): 14534-14544.

Tanaka, Y., Y. Kanai, et al. (1998). "Targeted disruption of mouse conventional kinesin heavy chain, kif5B, results in abnormal perinuclear clustering of mitochondria." Cell **93**(7): 1147-1158.

Taylor, A. M., M. Blurton-Jones, et al. (2005). "A microfluidic culture platform for CNS axonal injury, regeneration and transport." Nat. Methods **2**(8): 599-605.

Theodoridis, S. and K. Koutroumbas (2008). Pattern Recognition, Academic Press.

Thomann, D., D. R. Rines, et al. (2002). "Automatic fluorescent tag detection in 3D with super-resolution: application to the analysis of chromosome movement." J Microsc **208**(Pt 1): 49-64.

Thorn, K. S., J. A. Ubersax, et al. (2000). "Engineering the processive run length of the kinesin motor." J Cell Biol **151**(5): 1093-1100.

Tienari, P. J., B. De Strooper, et al. (1996). "The beta-amyloid domain is essential for axonal sorting of amyloid precursor protein." EMBO J **15**(19): 5218-5229.

Vallee, R. B. V., J. C. W. Williams, et al. (2004). "Dynein: an ancient motor protein involved in multiple modes of transport." Journal of Neurobiology **58**(2): 189-200.

Vaughan, K. T. and R. B. Vallee (1995). "Cytoplasmic dynein binds dynactin through a direct interaction between the intermediate chains and p150Glued." J. Cell Biol. **131**(6): 1507-1516.

Verhey, K. J. and J. W. Hammond (2009). "Traffic control: regulation of kinesin motors." Nat. Rev. Mol. Cell Biol. **10**(11): 765-777.

Verhey, K. J., D. L. Lizotte, et al. (1998). "Light chain-dependent regulation of Kinesin's interaction with microtubules." J Cell Biol **143**(4): 1053-1066.

Wang, Z., S. Khan, et al. (1995). "Single cytoplasmic dynein molecule movements: characterization and comparison with kinesin." Biophys. J. **69**(5): 2011-2023.

Welte, M. A. (2004). "Bidirectional transport along microtubules." Curr Biol **14**(13): R525-537.

Wu, C. F., N. Suzuki, et al. (1983). "Dissociated neurons from normal and mutant Drosophila larval central nervous system in cell culture." J Neurosci **3**(9): 1888-1899.

Wu, J. Q. and T. D. Pollard (2005). "Counting cytokinesis proteins globally and locally in fission yeast." Science **310**(5746): 310-314.

Xia, C., A. Rahman, et al. (1998). "Chromosomal localization reveals three kinesin heavy chain genes in mouse." Genomics **52**(2): 209-213.

Xia, C. H., E. A. Roberts, et al. (2003). "Abnormal neurofilament transport caused by targeted disruption of neuronal kinesin heavy chain KIF5A." J Cell Biol **161**(1): 55-66.

Yang, G., A. Matov, et al. (2005). "Reliable tracking of large-scale dense particle motion for fluorescent live cell imaging." Proc. IEEE Int. Conf. Computer Vision and Pattern Recognition **3**: 138.